

**RESEARCH ON COMPRESSED SENSING AND ITS APPLICATIONS
IN WIRELESS COMMUNICATIONS**

by

Xianjun Yang



Dissertation submitted in fulfilment of the requirements

for the degree of

DOCTOR OF PHILOSOPHY

Department of Engineering
Faculty of Science
Macquarie University
Sydney, Australia

Jun 2014

ABSTRACT

Compressed Sensing (CS) suggests that it is possible to enable sub-Nyquist sampling, by merging sampling and compression into one single step. Hence, CS will lead to a revolution in the sampling area. Moreover, CS will have great impacts on information theory, coding and wireless communications.

In this thesis, we will study the basic sampling problem of analog sparse signals and investigate the applications of CS into Cognitive Radio Networks (CRNs) and Wireless Sensor Networks (WSNs). The main contributions of this thesis are summarized as follows.

(1) Application of discrete CS into WSNs. Based on discrete CS and network coding, we significantly improve the energy efficiency of WSN by simultaneously reducing the number of required transmissions and receptions.

(2) Research on analog CS. Based on the non-modulated Slepian basis, we simultaneously improve the recovery performance and reduce the recovery computation complexity of analog CS. Based on the structure of the random cyclic orthogonal matrix, we reduce the hardware complexity of analog CS by utilizing the cyclic shifts of the Zadoff-Chu sequence.

(3) Application of analog CS into CRNs. By introducing analog CS and multi-antenna technology, we improve the detection performance of wideband spectrum sensing (WSS) in CRNs at the sub-Nyquist sampling rate.

(4) Research on denoising CS recovery algorithm. To improve the CS recovery performance in noisy environments, we propose a regularized subspace pursuit (RSP) denoising CS recovery algorithm, which has the highest recovery performance in comparison with existing CS recovery algorithms.

So far, the application of CS in channel estimation for LTE-A systems has been discussed by 3GPP. It is believed that, in the future, more and more new problems faced by wireless communications will be resolved with the help of CS.

STATEMENT OF CANDIDATE

I certify that the work in this thesis has not previously been submitted for a degree nor has it been submitted as part of the requirements for a degree to any other university or institution other than Macquarie University.

I certify that the thesis is an original piece of research and has been written by me.

In addition, I certify that all information sources and literature used are indicated in the thesis.

Xianjun Yang

Xianjun Yang

ACKNOWLEDGMENTS

First and foremost, I would like to express my sincerest gratitude to my supervisor, Prof. Eryk Dutkiewicz (Macquarie University, Australia), who has constantly encouraged me to strive for excellence in my career. This work would not have been completed without his remarkable insight, great knowledge, invaluable guidance and generous financial support for international academic exchange.

I would also like to acknowledge my supervisors Prof. Xiaojing Huang (CSIRO Computational Informatics, Australia), Prof. Y. Jay Guo (CSIRO Computational Informatics, Australia), Dr. Gengfa Fang (Macquarie University, Australia), Prof. Xiaofeng Tao (Beijing University of Posts and Telecommunications, China), and Prof. Qimei Cui (Beijing University of Posts and Telecommunications, China) for their support, advice and encouragement throughout this work.

Furthermore, I would like to thank my colleagues, friends and staff from Macquarie University, CSIRO Computational Informatics, and Beijing University of Posts and Telecommunications who helped me during my PhD studies.

Finally, I am forever indebted to my parents and brother for their infinite support, encouragement and love.

Contents

Abstract	iii
Acknowledgments	ix
Table of Contents	xi
List of Figures	xvii
List of Tables	xxi
List of Publications	xxiii
1 Introduction	1
1.1 Background	1
1.2 Motivation	2
1.2.1 Energy consumption of the wireless communications in catastrophic scenarios	3
1.2.2 Sampling problem of multi-band signals	4
1.2.3 Contradiction of spectrum shortage and low spectrum utilization . .	4
1.2.4 Degradation of wireless system performance caused by noise	5
1.3 Contributions of the Thesis	5
1.3.1 CS Based Energy-efficient DDS in WSNs	5
1.3.2 Structured Matrix Based Analog CS	6

1.3.3	Multi-antenna Based Compressed WSS for CRs	6
1.3.4	Denoising CS Recovery Algorithm	7
1.4	Organization of the Thesis	7
2	Literature Review	11
2.1	Discrete Compressed Sensing	11
2.1.1	Sparse Representation	12
2.1.2	Property of Measurement Matrix	12
2.1.3	Signal Recovery Algorithms in Noise-free Scenario	14
2.1.4	Signal Recovery Algorithms in Noisy Environments	17
2.2	Analog Compressed Sensing	20
2.2.1	AIC Method	21
2.2.2	MWC Method	23
2.2.3	Other Analog CS Methods	28
2.3	Applications of Compressed Sensing	29
2.3.1	Compressive Imaging	29
2.3.2	Compressed Sensing for Wireless Communications	31
3	Compressed Network Coding for Distributed Data Storage in WSNs	33
3.1	Introduction	33
3.2	Signal Model and Network Deployment	36
3.2.1	Signal Model	36
3.2.2	Network Deployment	37
3.3	Proposed CNCDS Scheme	38
3.3.1	Overall Description of CNCDS Scheme	38
3.3.2	Procedures of CNCDS Scheme	39
3.3.3	Choice of Parameters N_s and P_0	41

3.3.4	Formulation of Measurement Matrix	41
3.3.5	Property of Measurement Matrix	44
3.3.6	Discussion of CNCDS Scheme under More Practical Conditions . .	47
3.4	Derivation of Expressions for Nt_{tot} and Nr_{tot}	48
3.4.1	Preliminary Knowledge	49
3.4.2	Lemma for Expressions for Nt_{tot} and Nr_{tot}	49
3.4.3	Derivation of N_r^{II}	50
3.4.4	Derivation of N_r^q	51
3.4.5	Formal Expressions for Nt_{tot} and Nr_{tot}	53
3.5	The Adaptive CNCDS Scheme	54
3.5.1	Motivation of Adaptive CNCDCS Scheme	54
3.5.2	Description of Adaptive CNCDCS Scheme	55
3.5.3	Extended Research on Energy Efficiency of Wireless Network	56
3.6	Performance Evaluation	57
3.6.1	Simulation Parameters and Performance Metrics	57
3.6.2	Schemes Used for Comparison	57
3.6.3	Simulation Results	58
3.7	Summary	64
4	Structured Measurement Matrix Based Analog Compressed Sensing	67
4.1	Introduction	67
4.2	Non-Modulated Slepian Basis Based Analog Compressed Sensing	70
4.2.1	Brief Introduction to Slepian Basis	70
4.2.2	Analytical Derivation of MWC under Slepian Basis	72
4.2.3	Recovery Algorithm	73
4.2.4	Performance Evaluation	76
4.3	Random Circulant Orthogonal Matrix Based Analog CS	79

4.3.1	Description of RCOM-ACS Scheme	79
4.3.2	Measurement Matrix of RCOM-ACS Scheme	81
4.3.3	Conditions for Successful Recovery	83
4.3.4	Extensions of RCOM-ACS Scheme	85
4.3.5	Fast Processing RCOM-ACS Scheme	85
4.3.6	Performance Evaluation	87
4.4	Summary	90
5	Compressed Wideband Spectrum Sensing for CRNs	93
5.1	Introduction	93
5.2	System Model	95
5.3	DA Algorithm for Wideband Spectrum Sensing	96
5.3.1	Description of DA algorithm	96
5.3.2	Theoretical Analysis of DA algorithm	97
5.3.3	Performance Evaluation of DA algorithm	100
5.3.4	Extended Research on Spectrum Sensing and Data Transmission . .	101
5.4	CS Recovery Algorithms for Multi-antenna Signals	103
5.4.1	CRL ₂ Algorithm	103
5.4.2	CBS Algorithm	105
5.4.3	Summary of CRL ₂ Algorithm and CBS Algorithm	106
5.5	Numerical Results	107
5.6	Summary	110
6	Denoising Regularized Subspace Pursuit CS Recovery Algorithm	113
6.1	Introduction	113
6.2	Proposed RSP Algorithm	115
6.2.1	Basic Idea	115

6.2.2	Pseudocode of Proposed RSP Algorithm	118
6.3	Performance Evaluation	119
6.3.1	Simulation Parameters and Performance Metrics	119
6.3.2	Illustration of Noise-folding Effect	120
6.3.3	Simulation Results under Signal Model $\mathbf{y}=\mathbf{A}(\mathbf{x} + \mathbf{z}) + \mathbf{w}$	121
6.3.4	Simulation Results under Signal Model $\mathbf{y}=\mathbf{A}\mathbf{x} + \mathbf{w}$	123
6.4	Summary	127
7	Conclusions and Future Work	129
7.1	Innovations in the Thesis	129
7.1.1	CNCDS Scheme	129
7.1.2	Research on Analog CS Based on Structured Matrix	130
7.1.3	MCWSS Scheme	131
7.1.4	CS Denoising Recovery Algorithm – Regularized Subspace Pursuit .	131
7.2	Future Work	132
7.2.1	New DDS Scheme Based on Spatial and Temporary Correlation . .	132
7.2.2	Novel Analog CS Method with Low Time Delay and Low Hardware Complexity	132
7.2.3	New WSS Scheme Based on CS Measurements	133
7.2.4	Theoretical Analysis of Denoising Recovery Algorithm	133
A	Derivations of Some Expressions in Chapter 3	135
A.1	Derivation of \bar{S}_2	135
A.2	Computation of \bar{S}_{Π}	136
A.3	Calculation of $N_{r,1}^q$, $N_{r,2}^q$, $N_{r,3}^q$ and $N_{r,4}^q$	137
A.3.1	Calculation of $N_{r,1}^q$	137
A.3.2	Calculation of $N_{r,2}^q$	137

A.3.3	Calculation of $N_{r,3}^q$	138
A.3.4	Calculation of $N_{r,4}^q$	139
A.4	Derivation of \bar{S}_3	139
A.5	Computation of \bar{S}_{2l}	140
Symbols		141
Abbreviations		143
Bibliography		149

List of Figures

Figure 1.1	Relations of the main chapters in this thesis.	8
Figure 2.1	Block diagram of AIC [1].	21
Figure 2.2	Illustration of the multi-band signal.	24
Figure 2.3	Block diagram of MWC [2].	25
Figure 2.4	Block diagram of random filters, (a) using convolution, (b) using FFT/IFFT. [3]	29
Figure 2.5	Aerial view of the single-pixel CS camera in the lab [4].	30
Figure 3.1	Illustration of the network deployment, where $N_s = 30$ nodes of the total $N = 100$ nodes are randomly selected as source nodes.	37
Figure 3.2	Packet format of the i^{th} node in CNCDS scheme.	39
Figure 3.3	(a) Source nodes broadcasting process in Stage II, (b) Intermediate nodes forwarding process in Stage III.	42
Figure 3.4	(a) Illustration of the area (represented by oblique lines) in which no nodes are located when calculating $P_{2,1}$, with $0 < d(i,j) \leq 2r_t$. (b) Illus- tration of the area S_{II} (represented by oblique lines) with $d(n_{s,1}, n_{s,2}) < r_t$, when calculating N_r^{II} in Section 3.4.3.	46
Figure 3.5	(a) Illustration of area S_{III} , (b) Illustration of area S_{c1} described in Case One.	52

Figure 3.6	Illustration of area S_{c2} in Case Two, and S_{c2} is further divided into two situations: (a) S_{c2a} with $0 < d(n_{t,1}^{q-1}, n_{t,2}^{q-1}) < r_t$, (b) S_{c2b} with $r_t < d(n_{t,1}^{q-1}, n_{t,2}^{q-1}) < 2r_t$.	53
Figure 3.7	The recovery MSE vs. the number of nodes queried by the mobile collector M .	59
Figure 3.8	The total number of receptions Nr_{tot} vs. the number of nodes queried by the mobile collector M .	61
Figure 3.9	The total number of transmissions Nt_{tot} vs. the number of nodes queried by the mobile collector M .	62
Figure 3.10	Comparison between the theoretical values and simulation results of the total number of transmissions Nt_{tot} vs. the number of nodes queried by the mobile collector M .	63
Figure 3.11	Comparison between the theoretical values and simulation results of the total number of receptions Nr_{tot} vs. the number of nodes queried by the mobile collector M .	64
Figure 4.1	Illustration of the recovered signal with the non-modulated Slepian basis and the DFT basis, compared with the original signal.	77
Figure 4.2	Comparison of the recovery SNR under the Slepian basis and the DFT basis versus the size of the Slepian basis in the noise-free environment.	78
Figure 4.3	Comparison of the recovery SNR under the Slepian basis and the DFT basis versus the size of the Slepian basis with SNR=10dB.	78
Figure 4.4	Block diagram of RCOM-ACS scheme.	80
Figure 4.5	Block diagram of SRCOM-ACS scheme.	86
Figure 4.6	Performance comparison among RCOM-ACS scheme, MWC and the collapsing method with M-BP recovery algorithm.	89

Figure 4.7 Performance comparison among RCOM-ACS scheme, MWC and the collapsing method with M-OMP recovery algorithm.	90
Figure 5.1 System model of MCWSS scheme.	95
Figure 5.2 Block diagram of DA algorithm.	96
Figure 5.3 Performance gain of DA algorithm compared with CFAR.	101
Figure 5.4 Detection probability of DA algorithm in multi-antenna scenario with different methods.	102
Figure 5.5 False alarm probability of DA algorithm in multi-antenna scenario with different methods.	103
Figure 5.6 Description of CRL ₂ algorithm.	104
Figure 5.7 Block diagram of CBS algorithm.	106
Figure 5.8 Performance of three joint processing methods: L ₁ norm combining, L ₂ norm combining, L _∞ norm combining.	108
Figure 5.9 Detection probability of CRL ₂ and CBS algorithm compared with single antenna scenario.	110
Figure 5.10 False alarm probability of CRL ₂ and CBS algorithm compared with single antenna scenario.	111
Figure 6.1 Illustration of the noise-folding effect, the successful recovery rate η vs. the number of measurements M	120
Figure 6.2 Illustration of the noise-folding effect, the normalized reconstruction error ε vs. the number of measurements M	121
Figure 6.3 Successful recovery rate η vs. the number of measurements M , when $\mathbf{y}=\mathbf{A}(\mathbf{x} + \mathbf{z}) + \mathbf{w}$, $\sigma^2=0.05$ and $\text{SNR} \approx 10 \lg^{1/(1+\frac{12.8}{M})}\text{dB}$	122
Figure 6.4 Normalized reconstruction error ε vs. the number of measurements M , when $\mathbf{y}=\mathbf{A}(\mathbf{x} + \mathbf{z}) + \mathbf{w}$, $\sigma^2=0.05$ and $\text{SNR} \approx 10 \lg^{1/(1+\frac{12.8}{M})}\text{dB}$	122

Figure 6.5	Successful recovery rate η vs. $\text{SNR} \approx 10 \lg^{1/(1+\frac{256}{90}\sigma^2)}$, when $\mathbf{y}=\mathbf{A}(\mathbf{x} + \mathbf{z}) + \mathbf{w}$ and $M=90$	124
Figure 6.6	Normalized reconstruction error ε vs. $\text{SNR} \approx 10 \lg^{1/(1+\frac{256}{90}\sigma^2)}$, when $\mathbf{y}=\mathbf{A}(\mathbf{x} + \mathbf{z}) + \mathbf{w}$ and $M=90$	124
Figure 6.7	Successful recovery rate η vs. the number of measurements M , when $\mathbf{y}=\mathbf{A}\mathbf{x} + \mathbf{w}$ and $\text{SNR}=10\text{dB}$	125
Figure 6.8	Normalized reconstruction error ε vs. the number of measurements M , when $\mathbf{y}=\mathbf{A}\mathbf{x} + \mathbf{w}$ and $\text{SNR}=10\text{dB}$	125
Figure 6.9	Successful recovery rate η vs. SNR , when $\mathbf{y}=\mathbf{A}\mathbf{x} + \mathbf{w}$ and $M=90$	126
Figure 6.10	Normalized reconstruction error ε vs. SNR , when $\mathbf{y}=\mathbf{A}\mathbf{x} + \mathbf{w}$ and $M=90$	126
Figure A.1	(a) The critical situation when case one happens, (b) Illustration of the area of S_3 when calculating N_{c1}	138

List of Tables

Table 2.1	Procedures of OMP Algorithm [5]	16
Table 3.1	Pseudocode of CNCDS Scheme	40
Table 4.1	Cost of Different Schemes	88
Table 5.1	Procedures of CRL_2 algorithm	105
Table 5.2	Procedures of CBS Algorithm	107
Table 6.1	Psudocode of Proposed RSP Algorithm	118

List of Publications

The publications of the author during her PhD study are listed as follows.

- **Journal Papers**

1. **Xianjun Yang**, Xiaofeng Tao, Eryk Dutkiewicz, Xiaojing Huang, Y. Jay Guo, Qimei Cui, “Energy-Efficient Distributed Data Storage for Wireless Sensor Networks Based on Compressed Sensing and Network Coding,” *IEEE Transactions on Wireless Communications*, Vol.12, 2013, pp.5087-5099. (corresponding to Chapter 3)
2. Qimei Cui, **Xianjun Yang**, Hamalainen Jyri, Xiaofeng Tao, Ping Zhang, “Optimal Energy-efficient Relay Deployment for the Bidirectional Relay Transmission Schemes,” *IEEE Transactions on Vehicular Technology*, 2013. (related to Chapter 3, Section 3.5.3)
3. **Xianjun Yang**, Xiaofeng Tao, Y. Jay Guo, Qimei Cui, Xiaojing Huang, “Subsampled circulant matrix based analog compressed sensing,” *IET Electronics Letters*, 2012, vol.48, pp. 767-768. (corresponding to Chapter 4)
4. **Xianjun Yang**, Xiaofeng Tao, Qimei Cui, Y. Jay Guo, “Interference-constrained adaptive simultaneous spectrum sensing and data transmission scheme for unslotted cognitive radio network,” *EURASIP Journal on Wireless Communications and Networking* 2012, 2012:102, pp. 1-12. (related to Chapter 5, Section 5.3.4)

- **Conference papers**

1. **Xianjun Yang**, Eryk Dutkiewicz, Qimei Cui, Xiaojing Huang, Xiaofeng Tao, Gengfa Fang, “Analog Compressed Sensing for Multiband Signals with Non-Modulated

Slepian Basis,” IEEE International Conference on Communications (ICC), 2013, pp. 3534-3538. (corresponding to Chapter 4)

2. **Xianjun Yang**, Y. Jay Guo, Qimei Cui, Xiaofeng Tao, Xiaojing Huang, “Random Circulant Orthogonal Matrix based Analog Compressed Sensing,” IEEE Global Communications Conference (GlobeCom), 2012, pp. 3629-3633. (corresponding to Chapter 4)

3. **Xianjun Yang**, Eryk Dutkiewicz, Qimei Cui, Xiaofeng Tao, Y. Jay Guo, Xiaojing Huang, “Compressed Network Coding for Distributed Storage in Wireless Sensor Networks,” International Symposium on Communications and Information Technologies (ISCIT), 2012, pp. 816-821. (Won the “Best Paper Award”, corresponding to Chapter 3)

4. **Xianjun Yang**, Qimei Cui, Rui Yang, Xiaofeng Tao, Xin Guo, “Multi-antenna Compressed Wideband Spectrum Sensing for Cognitive Radio,” IEEE Wireless Communications and Networking Conference (WCNC), 2011, pp. 1903-1908. (corresponding to Chapter 5)

5. **Xianjun Yang**, Qimei Cui, Eryk Dutkiewicz, Xiaojing Huang, Xiaofeng Tao, “Anti-Noise-Folding Regularized Subspace Pursuit Recovery Algorithm for Noisy Sparse Signals,” IEEE Wireless Communications and Networking Conference (WCNC), 2014, pp. 287-292.(corresponding to Chapter 6)

6. Xuefei Zhang, Qimei Cui, **Xianjun Yang**, Xiaofeng Tao, “A Multistep Detection Scheme Based on Iteration for Cooperative Spectrum Sensing in Cognitive Radio,” IEEE Vehicular Technology Conference (VTC) Fall 2011, pp.1-5.

7. Xiangling Li, Qimei Cui, Xiaofeng Tao, **Xianjun Yang**, Waheed Ur Rehman, “Performance Bounds of Compressed Sensing Recovery Algorithms for Sparse Noisy Signals,” IEEE Wireless Communications and Networking Conference (WCNC), 2013, pp.2884-2889.

- **Patents**

1. Xiaofeng Tao, Qimei Cui, **Xianjun Yang**, Xiaodong Xu, Ping Zhang, "Analog Compressed Sensing Sampling Method and System Based on Random Cyclic Matrices", Application No. 2012200795. (Australia Patent, corresponding to Chapter 4)
2. Qimei Cui, **Xianjun Yang**, Xiaofeng Tao, Rui Yang, Xuefei Zhang, "Apparatus and method of Spectrum Sensing for Cognitive Radio, and program" Application No. 201010179307.4, Publication No. CN102255675A. (China Patent, corresponding to Chapter 5)
3. Qimei Cui, Shiyuan Li, Xiaofeng Tao, Chao Wang, **Xianjun Yang**, "Method and device for user pairing for uplink multi-user MIMO under coordinated multiple point transmission scenario", EP 2288049(A2). (European Patent)

Chapter 1

Introduction

In this chapter, the historic development and vision of compressed sensing is shown in Section 1.1, the motivation of this thesis is addressed in Section 1.2, the contributions of this thesis are summarized in Section 1.3, and the organization of this thesis is described in Section 1.4.

1.1 Background

Compressed sensing (CS) was firstly proposed by David L. Donoho, Emmanuel J. Candes, and Terence Tao in 2004, the related work [6] [7] was published in 2006 and won the Information Theory Society Paper Award in 2008. The basic idea of CS theory is that sparse signals or images can be successfully reconstructed from far fewer samples or measurements than that required by the Shannon-Nyquist theorem. Therefore, until now, CS [8] [9] is a very hot research topic in the signal processing society and has been widely applied into many areas, such as compressive imaging [10] [11], medical imaging [12] [13], geophysical data analysis [14] [15], sub-Nyquist sampling [16] [2], wireless communications [17] [18] and so on.

In the early stage of CS theory, it was confined to discrete signals for simplicity, because

this basic formulation already requires very sophisticated mathematical tools and rich theories to analyze the recovery approaches and provide performance guarantees. The applications of discrete CS mainly focus on image compression [11], magnetic resonance imaging (MRI) [12], seismic data processing [15], distributed source coding in multi-signal settings such as WSNs [19], designing fast error correcting codes [20] and so on.

Later on, CS is extended to analog domain in literatures [16] [2], aiming to reduce the extremely high sampling rate required by the ultra-wideband signal sampling (up to several GHz). The above methods provide guidance on how to design physical sampling devices that can directly acquire discrete, low-rate incoherent measurements from the incident analog signals. Specifically, analog-to-information conversion (AIC) [16] and modulated wideband converter (MWC) [2] are two typical examples of such sampling devices. The applications of analog CS mainly focus on wireless communications, such as the wideband spectrum sensing for CR networks [21], the multi-band signal sampling for LTE systems [22] and so on.

In the future, the basic theory of CS will be further studied and enriched. Specifically, more practical methods of finding an optimal basis to express a sparse signal will be established, more structures will be places into the measurement matrix to facilitate the implementation, and the performance of CS recovery algorithms in noisy environment will be improved significantly. More importantly, CS will be applied into wider areas, including imaging, data analysis, signal sampling, wireless communications and etc., in a more practical way.

1.2 Motivation

In the thesis, we focus on the research of CS and its applications in wireless communications. Besides the research of CS itself, this thesis is also motivated by utilizing the

properties of CS to tackle the challenges faced by wireless communications.

Currently, the main challenges faced by wireless communications include high cost and energy consumption of wireless systems, the sampling problem of wideband signals with multiple discrete bands (multi-band signal), contradiction between spectrum shortage and low spectrum utilization, uneven information density and “tidal effect”, data collection and communication in catastrophic scenario, etc. To resolve these challenges, many new technologies have been proposed, such as, compressed sensing (CS) [6], green communications [23], cognitive radios (CRs) [24], wireless sensor networks (WSNs) [25], millimeter-wave communication [26], small cell technology [27], multi-user information theory [28], etc.

In this thesis, based on CS theory and combined with WSNs and CRs, we aim to investigate and tackle the following four challenges.

1.2.1 Energy consumption of the wireless communications in catastrophic scenarios

WSN is an efficient way to realize communications in catastrophic scenarios, since it can be easily deployed at low cost and can enable self-organizing networks. In such a harsh environment, a WSN is vulnerable or inaccessible and the sensor nodes are also unreliable. To guarantee reliable communication of WSNs in catastrophic environments, distributed data storage (DDS) is proposed in [29] and [30]. Specifically, the sensed data of DDS are stored with redundancy in the network, so that the mobile sink node is able to reconstruct all the sensed data in the whole WSN by visiting only a small number of the surviving nodes. Since the sensor node is battery-driven, energy efficiency is one of the most important performance metrics for WSNs [31]. Therefore, reliable and energy-efficient communications is indispensable for WSNs deployed in catastrophic environments.

1.2.2 Sampling problem of multi-band signals

With the rapid development of wireless communications, it is hard to find a continuous wide band (e.g., 100MHz) in low frequencies (e.g., 400MHz-3GHz) now. To provide high data rate communication, carrier aggregation (CA) [22] technology has been proposed in Long Term Evolution-Advanced (LTE-Advanced) to combine several discontinuous bands. To sample the CA signals, i.e., one kind of multi-band signals, we need several independent radio front-ends (RFs) and analog-to-digital converters (ADCs) [32]. However, since the cost of the RF part accounts for a very large part of the total wireless system cost, the independent RF solution has a very high cost and energy consumption, and furthermore, this solution also occupies a large space.

1.2.3 Contradiction of spectrum shortage and low spectrum utilization

On one side, most of the available spectrum have been assigned to different wireless communication systems. On the other side, many of the assigned spectrum bands are not fully utilized [33]. To solve the above problem, the concept of CR [24] [34] has been proposed to allow the unlicensed users accessing the temporarily unused licensed spectrum. The first step of CR is to detect the unoccupied spectrum, i.e., to carry out spectrum sensing [35]. Recently, wideband spectrum sensing (WSS) [36] has attracted a lot of attentions due to its ability to provide more opportunities of spectrum access than narrowband spectrum sensing (NSS). However, WSS faces more challenges than NSS. e.g., WSS requires an extremely high sampling rate (e.g., several GHz) and high computation complexity.

1.2.4 Degradation of wireless system performance caused by noise

In wireless communication systems, the transmitters, receivers and channels are inevitably contaminated by noise. Unfortunately, noise degrades the performance of wireless systems, especially when CS is applied in wireless systems, since the rectangular CS measurement matrix amplifies the power of noise [37]. Thus, effective denoising CS recovery algorithms are essential to make the applications of CS in wireless communication practical, especially when the sparse signal is contaminated by noise before CS measurements.

1.3 Contributions of the Thesis

The objectives of this thesis are to tackle the challenges stated in Section ?? based on CS. The contributions of this thesis are stated as follows.

1.3.1 CS Based Energy-efficient DDS in WSNs

As mentioned in Section 1.2.1, DDS is an efficient communication method for WSNs in catastrophic scenarios. Here, we aim to improve the energy efficiency of DDS. It is worthwhile to note that the energy costs for data transmission and data reception are nearly the same in WSNs with short-range communications. Thus, we propose to improve the energy efficiency of WSNs by simultaneously reducing the number of data transmissions and receptions based on CS and network coding. Theoretical analysis proves that the proposed scheme guarantees good CS recovery performance. Based on the random geometric graphs (RGG) theory, we derive the expressions for the number of transmissions and receptions. Furthermore, on the basis of the derived expressions, an adaptive scheme is proposed to further improve the energy efficiency. Simulation results show that, compared with existing schemes, our scheme has the highest energy efficiency at the lowest

reconstruction error.

1.3.2 Structured Matrix Based Analog CS

We improve the recovery performance of analog CS from the angle of signal representation. Specifically, to avoid the frequency leakage effect of the Discrete Fourier Transform (DFT) basis, we propose using the non-modulated Slepian basis to represent the modulated and bandlimited multi-band signals. Compared with the method using the modulated Slepian basis to represent the whole multi-band signal, our method reduces the dimension of the measurement matrix and thus reduces the computational complexity of recovery. Furthermore, based on the random circulant orthogonal matrix, we reduce the hardware complexity of analog CS by replacing the independent pseudo-random mixing functions with the cyclic shifts of Zadoff-Chu (ZC) Sequence. We prove that the measurement matrix of the proposed scheme satisfies the sufficient condition for successful CS recovery, i.e., the Restricted Isometry Property (RIP), with very high probability.

1.3.3 Multi-antenna Based Compressed WSS for CRs

To improve the detection performance of compressed WSS in low signal-to-noise ratio (SNR) scenarios, we propose a multi-antenna technology based compressed WSS scheme. In the proposed scheme, we introduce multi-antenna technology to combat the influence of noise and propose a joint recovery algorithm by utilizing the joint sparsity of multi-antenna signals. To reduce the influence of noise uncertainty on detection performance, we propose a low-complexity and high-performance detection algorithm, whose threshold dynamically varies with the actual noise variance. Simulation results show that, our proposed scheme has high detection performance at about 28% of the Nyquist sampling rate in low SNR scenarios.

1.3.4 Denoising CS Recovery Algorithm

We propose a novel denoising CS recovery algorithm for the scenario where both the sparse signal and the CS measurements are contaminated by noise. In the proposed algorithm, we reduce the noise-folding effect caused by the noise in sparse signals via adding a pre-processing operation. To make the identified columns corresponding to the non-zero elements approximately satisfy the restricted isometry property (RIP) condition, we regularize the chosen columns. To further reduce the effect of noise, we adopt the Minimum Mean Square Estimation (MMSE) method to estimate the non-zero elements. Simulation results show that, compared with existing CS recovery algorithms, our proposed algorithm has the highest successful recovery rate and the lowest reconstruction error.

1.4 Organization of the Thesis

The relations between the main chapters of this thesis are shown in Figure 1.1. Specifically, this organization of this thesis is stated as follows:

Chapter 1 is Introduction. Section 1.2 states the motivation of this thesis, i.e., the main challenges we aim to tackle. Section 1.3 describes the main contributions of this thesis. Section 1.4 introduces the organization of this thesis. Section ?? lists the papers and patents published by the author.

Chapter 2 is Literature Review. Section 2.1 introduces the theory of discrete CS. Section 2.2 presents the existing methods for analog CS. And Section 2.3 briefly introduces the applications of CS in imaging and wireless communications.

Chapter 3 discusses the application of discrete CS into WSNs. Specifically, Section 3.3 proposes a compressed network coding based distributed data storage (CNCDS) scheme, which improves the energy efficiency of WSNs by simultaneously reducing the number of data transmissions and receptions. Based on the random geometric graph theory,

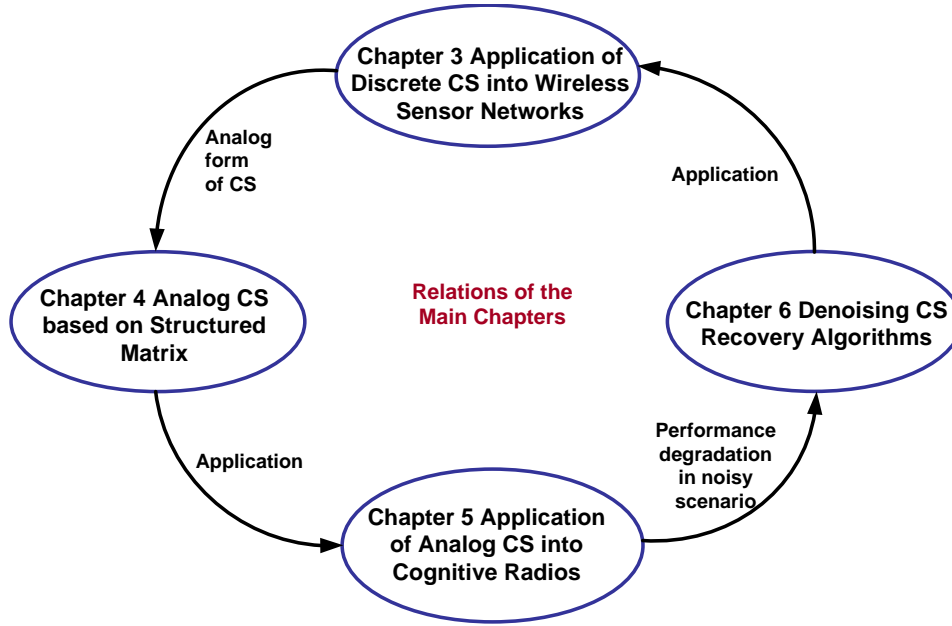


Figure 1.1: Relations of the main chapters in this thesis.

Section 3.4 derives the expressions for the number of data transmissions and receptions. Furthermore, based on the derived expressions, Section 3.5 proposes an adaptive CNCDS scheme to further improve the energy efficiency of WSNs.

Chapter 4 studies the analog CS based on the structured matrix. Section 4.1 introduces the related work on analog CS. Section 4.2 improves the recovery performance of analog CS based on the non-modulated Slepian basis. Section 4.3 reduces the hardware complexity of analog CS based on the random circulant orthogonal matrix.

Chapter 5 investigates the application of analog CS into WSS for cognitive radios. To improve the detection performance in low SNR scenarios at lower sampling rates, this chapter proposes a multi-antenna based compressed wideband spectrum sensing (MCWSS) scheme. Utilizing the joint sparsity of multi-antenna signals, Section 5.4.1 proposes a joint recovery algorithm. Base on the sparsity of wideband signals, Section 5.3 proposes a low-complexity WSS algorithm and alleviates the the effect of noise uncertainty.

Chapter 6 proposes a novel denoising CS recovery algorithm to resolve the problem met in Chapter 5, i.e., the problem that noise degrades the CS recovery performance. Specifically, Section 6.2 proposes the regularized subspace pursuit algorithm for the scenario where both the sparse signals and CS measurements are contaminated by noise.

Finally, Chapter 7 summarizes the research of this thesis and recommends related future work.

Chapter 2

Literature Review

Since the focus of this thesis is the research of CS and its application in wireless communications, in this chapter, we will give a comprehensive literature reviews on discrete CS, analog CS and the applications of CS are presented in Section 2.1, Section 2.2 and Section 2.3, respectively.

2.1 Discrete Compressed Sensing

The basic idea of discrete CS is that if an $N \times 1$ discrete signal \mathbf{x} is K -sparse in an orthogonal basis Ψ , i.e., $\mathbf{x} = \Psi\boldsymbol{\theta}$ and the coefficient vector $\boldsymbol{\theta}$ has only K nonzero elements, where the indices of the nonzero elements are called the signal support of signal $\boldsymbol{\theta}$, then \mathbf{x} can be successfully reconstructed from an $M \times 1$ measurement vector \mathbf{y} , where

$$\mathbf{y} = \Phi\mathbf{x} = \Phi\Psi\boldsymbol{\theta} = \mathbf{A}\boldsymbol{\theta}, \quad (2.1)$$

in which Φ is an $M \times N$ measurement matrix, which should satisfy the (RIP) [20] or the mutual incoherence property (MIP) [38], and $\mathbf{A} = \Phi\Psi$.

The CS theory is composed of three basic components, i.e., sparse representation of signals, stable measurement matrices and robust recovery algorithms. In this thesis, we assume that we know the signal is sparse in a certain basis as a prior information and

mainly focus on the property of the measurement matrix and the recovery algorithms. Next, the above three elements are introduced as follows.

2.1.1 Sparse Representation

As expressed in (2.1), the premise of the CS theory is that the signal is sparse/compressible in some basis/dictionary. Thus, sparse representation [39] [40] is the basis of the CS theory. In the literature, sparse representation is also known as sparse decomposition [38] [41] or sparse approximation [42]. Currently, existing lossy compression techniques rely on the empirical observations, for example, JPEG is based on the fact that the digital images are compressible in Discrete Cosine Transform (DCT) domain. The problem of finding the sparsest representation/approximation in terms of the given basis/dictionary turns out to be the general ℓ_0 -problem of finding the sparsest solution of an under-determined system. Unfortunately, the ℓ_0 -problem is NP-hard, then greedy methods and ℓ_1 -minimization were subsequently introduced as tractable alternatives. The details of ℓ_0 -problem, greedy methods and ℓ_1 -minimization will be elaborated in Section 2.1.3.

2.1.2 Property of Measurement Matrix

The two important and equivalent properties for the CS measurement matrix are stated as follows.

Restricted Isometry Property

The restricted isometry constant [20] δ_K of an $M \times N$ matrix \mathbf{A} is defined as the smallest positive number such that the following condition

$$(1 - \delta_K) \|\boldsymbol{\theta}\|_2^2 \leq \|\mathbf{A}\boldsymbol{\theta}\|_2^2 \leq (1 + \delta_K) \|\boldsymbol{\theta}\|_2^2 \quad (2.2)$$

holds for every K -sparse vector $\boldsymbol{\theta}$, where $\|\boldsymbol{\theta}\|_2 = \sqrt{\sum_{j=1}^N (\theta_j)^2}$ is the ℓ_2 norm of vector $\boldsymbol{\theta}$. If $K + K' < N$, the K, K' -restricted orthogonality constant $\gamma_{K, K'}$ is defined as the

smallest number that satisfies the following condition

$$|\langle \mathbf{A}\boldsymbol{\theta}, \mathbf{A}\boldsymbol{\theta}' \rangle| \leq \gamma_{K,K'} \|\boldsymbol{\theta}\|_2 \|\boldsymbol{\theta}'\|_2 \quad (2.3)$$

for all the K -sparse vector $\boldsymbol{\theta}$ and K' -sparse vector $\boldsymbol{\theta}'$, where $\boldsymbol{\theta}$ and $\boldsymbol{\theta}'$ have disjoint support.

The RIP [20] refers to the following statements, if

$$\delta_K + \gamma_{K,K} + \gamma_{K,2K} < 1, \quad (2.4)$$

then the K -sparse solution to the following ℓ_1 minimization problem is unique

$$\hat{\boldsymbol{\theta}} = \arg \min_{\boldsymbol{\theta} \in \mathbb{R}^N} \|\boldsymbol{\theta}\|_1, \text{ s.t. } \mathbf{y} = \mathbf{A}\boldsymbol{\theta}. \quad (2.5)$$

Besides, we have a similar condition in [43], which indicated that if

$$\delta_{3K} + 3\delta_{4K} < 2, \quad (2.6)$$

then the K -sparse signal can be successfully reconstructed from the problem in (2.5).

However, the calculation of the restricted isometry constant δ_K is a Non-deterministic Polynomial(NP)-hard problem, thus the MIP is proposed as follows.

Mutual Incoherence Property

The mutual incoherence [38] between the measurement matrix Φ and the basis Ψ is defined as

$$\mu(\Phi, \Psi) = \sup \{ |\langle \phi_i, \psi_j \rangle| \}, \quad (2.7)$$

where $\sup\{x\}$ denotes the supremum of x , ϕ_i and ψ_j are the i^{th} and j^{th} column of matrix Φ and Ψ , respectively. The MIP refers to the following property, if

$$K < \frac{1}{2} \left(1 + \frac{1}{\mu} \right), \quad (2.8)$$

then the K -sparse solution to the ℓ_1 minimization problem in (2.5) is unique.

The connections between RIP and MIP

From (2.2), (2.3) and (2.7), we can conclude that [44]

$$\mu = \delta_2 = \gamma_{1,1}. \quad (2.9)$$

Furthermore, [45] indicated that

$$\delta_K \leq (K-1)\mu \quad \text{and} \quad \gamma_{K,K'} \leq \sqrt{KK'}\mu. \quad (2.10)$$

With the above relations, the results in RIP can also be stated in terms of MIP. However, the current RIP conditions are not enough for achieving the sharp MIP condition (2.8) [45].

2.1.3 Signal Recovery Algorithms in Noise-free Scenario

The natural and optimal method to resolve problem (2.1) is the following ℓ_0 minimization problem

$$\hat{\boldsymbol{\theta}} = \arg \min_{\boldsymbol{\theta} \in \mathbb{R}^N} \|\boldsymbol{\theta}\|_0, \quad s.t. \quad \mathbf{y} = \mathbf{A}\boldsymbol{\theta}, \quad (2.11)$$

where the ℓ_0 norm $\|\boldsymbol{\theta}\|_0$ counts the number of the nonzero elements in vector $\boldsymbol{\theta}$. However, the ℓ_0 minimization problem is NP-hard, so many sub-optimal algorithms to solve problem (2.1) are proposed. Generally speaking, the CS recovery algorithms can be classified into the following two categories, i.e., the relaxed optimization algorithms and the greedy algorithms, which are stated as follows, respectively.

Convex Relaxation Algorithms

To overcome the above obstacle in solving the ℓ_0 minimization problem, the ℓ_0 minimization problem is relaxed to the ℓ_1 minimization problem (2.5) [46], which is convex and can be formulated as the following linear programming (LP) problem [6]

$$\hat{\mathbf{z}} = \arg \min_{\mathbf{z} \in \mathbb{R}^{2N}} \mathbf{1}^T \mathbf{z} \quad s.t. \quad \mathbf{B}\mathbf{z} = \mathbf{y}, \mathbf{z} \geq \mathbf{0}, \quad (2.12)$$

where $\mathbf{B} = [\mathbf{A}, -\mathbf{A}]$, and $\hat{\mathbf{z}}$ is partitioned as $\hat{\mathbf{z}}^T = [\mathbf{u}^T, \mathbf{v}^T]$, where $\mathbf{u}^T, \mathbf{v}^T \in \mathbb{R}^N$. Then, the solution to problem (2.5) is $\hat{\boldsymbol{\theta}} = \mathbf{u} - \mathbf{v}$, which is near-optimal. The problem (2.12) has been investigated under the name of basis pursuit (BP) [47] in the signal analysis area.

Nonconvex Local Optimization Algorithms

Based on the weighted norm minimization, the FOCal Underdetermined System Solver (FOCUSS) algorithm [48] is proposed to combine the desirable characteristics of both classical optimization and learning-based algorithms. The FOCUSS algorithm has two integral parts: a low-resolution initial estimate of the real signal and the iteration process that refines the initial estimate to the final localized solution. The iterations are based on minimization of the weighted norm of the dependent variables, where the weights are a function of the preceding iterative solutions.

A weighted minimum norm solution is defined as the solution minimizing a weighted norm $\|\mathbf{W}^+\boldsymbol{\theta}\|_2 = \sqrt{\sum_{j=1, w_{j,j} \neq 0}^{j=N} (\frac{\theta_j}{w_{j,j}})^2}$, where \mathbf{W} is a diagonal matrix with the entries $w_{j,j}$ in the diagonal, \mathbf{W}^+ is the Moore-Penrose pseudo-inverse of \mathbf{W} . The definition of a weighted minimum norm solution is

$$\begin{aligned} \text{find } \boldsymbol{\theta} &= \mathbf{W}\mathbf{q} \\ \text{where } \mathbf{q} &= \arg \min_{\mathbf{q}' \in \mathbb{R}^N} \|\mathbf{q}'\|_2, \text{ s.t. } \mathbf{y} = \mathbf{AW}\mathbf{q}'. \end{aligned} \tag{2.13}$$

That is to say, $\boldsymbol{\theta} = \mathbf{W}(\mathbf{AW})^+\mathbf{y}$. The choice of the weighted matrix \mathbf{W} is based on the generalized Affine Scaling Transformation (AST), which scales the entries of the current solution by the solutions of the previous iterations.

Thus, the basic form of the FOCUSS algorithm is

$$\begin{aligned} \text{Step 1: } \mathbf{W}^{[t]} &= (\text{diag}(\boldsymbol{\theta}^{[t-1]})) , \\ \text{Step 2: } \mathbf{q}^{[t]} &= (\mathbf{AW}^{[t]})^+\mathbf{y}, \\ \text{Step 3: } \boldsymbol{\theta}^{[t]} &= \mathbf{W}^{[t]}\mathbf{q}^{[t]}. \end{aligned} \tag{2.14}$$

Table 2.1: Procedures of OMP Algorithm [5]

Input: \mathbf{A} , \mathbf{y} and K .
Initialization: Initialize the residual $\mathbf{r}_0 = \mathbf{y}$, the signal support set $\Lambda_0 = \emptyset$, and the iteration counter $t = 1$.
Iterations:
FOR $t = 1$ to K
$\lambda_t = \arg \max_{j=1,\dots,N} \langle \mathbf{r}_{t-1}, \mathbf{a}_j \rangle $. % Finding the index λ_t
$\Lambda_t = \Lambda_{t-1} \cup \{\lambda_t\}$. % Augment the signal support set.
$\hat{\boldsymbol{\theta}}_t = \begin{cases} \mathbf{A}_{\Lambda_t}^+ \mathbf{y}, & \text{on the support set } \Lambda_t \\ \mathbf{0}, & \text{elsewhere} \end{cases}$. % Estimating the signal.
$\mathbf{r}_t = \mathbf{y} - \mathbf{A} \hat{\boldsymbol{\theta}}_t$. % Updating the residual.
$t = t + 1$.
END
Output: The estimated signal support Λ_K and the estimated signal $\hat{\boldsymbol{\theta}}_K$.

where $\boldsymbol{\theta}^{[t]}$ is the estimated signal in the t^{th} iteration, all the entries in the initial estimate should be nonzero, and the initial estimate does not have to satisfy a given linear system exactly.

Greedy Algorithms

Although the program (2.12) in the BP algorithm can be solved in polynomial time, the commercial optimization software packets tend not to work very well for sparse signal recovery, because the solution vector is sparse while the measurement matrix is dense. Thus, it seems valuable to explore alternative approaches which are not based on optimization. A representative alternative approach for BP is Orthogonal Matching Pursuit (OMP) [5], whose procedures are stated in Table 2.1.

According to (2.1), the measurement vector $\mathbf{y} = \mathbf{A}\boldsymbol{\theta}$ is a linear combination of K

columns from matrix \mathbf{A} , since $\boldsymbol{\theta}$ is K -sparse. Thus, the basic idea of OMP is to pick the K columns participating in the measurement vector \mathbf{y} in a greedy fashion. Specifically, the OMP algorithm begins by initializing the estimated signal support set Λ_0 as an empty set \emptyset and setting the residual \mathbf{r}_0 as \mathbf{y} . At the t^{th} iteration, OMP finds one single column of matrix \mathbf{A} that is most highly correlated with the residual in the $(t-1)^{th}$ iteration \mathbf{r}_{t-1} , i.e., the index of this column λ_t is obtained by

$$\lambda_t = \arg \max_{j=1, \dots, N} |\langle \mathbf{r}_{t-1}, \mathbf{a}_j \rangle|, \quad (2.15)$$

where \mathbf{a}_j is the j^{th} column of matrix \mathbf{A} . Then, the index λ_t is added to the support set via $\Lambda_t = \Lambda_{t-1} \cup \{\lambda_t\}$. With the least-square (LS) estimation method, the estimated signal $\hat{\boldsymbol{\theta}}_t$ at the t^{th} iteration is calculated by

$$\hat{\boldsymbol{\theta}}_t = \begin{cases} \arg \min_{\boldsymbol{\theta} \in \mathbb{R}^N} \|\mathbf{y} - \mathbf{A}_{\Lambda_t} \boldsymbol{\theta}\|_2 = \mathbf{A}_{\Lambda_t}^+ \mathbf{y}, & \text{on the support set } \Lambda_t \\ \mathbf{0}, & \text{elsewhere} \end{cases}, \quad (2.16)$$

where \mathbf{A}_{Λ_t} is a submatrix of matrix \mathbf{A} consisting of the columns indexed by Λ_t , $\mathbf{A}_{\Lambda_t}^+$ is the Moore-Penrose pseudo-inverse of \mathbf{A}_{Λ_t} . The residual at the t^{th} iteration is expressed as

$$\mathbf{r}_t = \mathbf{y} - \mathbf{A} \hat{\boldsymbol{\theta}}_t. \quad (2.17)$$

After K iterations, OMP stops and the reconstructed signal is $\hat{\boldsymbol{\theta}}_K$ and the reconstructed signal support is Λ_K .

Furthermore, the Stagewise OMP (StOMP) [49] algorithm is proposed to speed up the OMP algorithm by choosing the coordinates in the relevance vector $\mathbf{A}^H \mathbf{r}_{t-1}$ with amplitudes exceeding a specially chosen threshold at the t^{th} iteration, and after a fixed number of iterations, the StOMP algorithm will stop.

2.1.4 Signal Recovery Algorithms in Noisy Environments

In the basic CS problem (2.1), we assume that the measurements are accurate. However, in any real application, the measured data will invariably be corrupted by at least

a small amount of noise, since sensing devices do not have infinite precision. Thus, it is imperative to develop stable CS recovery algorithms, where small perturbations in the data should cause only small perturbations in the reconstruction.

The signal model with noisy measurements is

$$\mathbf{y} = \mathbf{A}\boldsymbol{\theta} + \mathbf{w}, \quad (2.18)$$

where \mathbf{w} is assumed to be a stochastic or deterministic unknown error term, e.g., the Gaussian noise [50] [51], the impulsive noise in image recovery [52] [53], and the Poisson noise in photon-limited imaging systems [54]. Since the focus of this thesis is the application of CS in wireless communication, we will mainly focus on the scenario with Gaussian noise. Next, we will introduce three recovery algorithms for Gaussian noise corrupted measurements.

Regularization Algorithms

A natural approach to finding the sparsest signal satisfying (2.18) is to solve the following ℓ_0 regularization problem

$$\hat{\boldsymbol{\theta}} = \arg \min_{\boldsymbol{\theta} \in \mathbb{R}^N} \left\{ \|\mathbf{y} - \mathbf{A}\boldsymbol{\theta}\|_2^2 + \lambda \|\boldsymbol{\theta}\|_0 \right\}, \quad (2.19)$$

where $\lambda > 0$ is a regularization parameter. However, the ℓ_0 regularization problem is NP-hard. To overcome this obstacle, problem (2.19) is relaxed to the following ℓ_p regularization problem

$$\hat{\boldsymbol{\theta}} = \arg \min_{\boldsymbol{\theta} \in \mathbb{R}^N} \left\{ \|\mathbf{y} - \mathbf{A}\boldsymbol{\theta}\|_2^2 + \lambda \|\boldsymbol{\theta}\|_p^p \right\}, \quad (2.20)$$

where $0 < p \leq 1$ and the ℓ_p norm is defined as $\|\boldsymbol{\theta}\|_p = \left(\sum_{i=1}^N |\theta_i|^p \right)^{1/p}$. When $p=1$, problem (2.20) is convex [55] and is called the ℓ_1 regularization or basis pursuit denoising (BPDN) algorithm [46], which has good recovery performance. Besides, when $p = 1$ problem

(2.20) can also be solved by the least absolute shrinkage and selection operator (LASSO) technique [56] [57]. When $0 < p < 1$, problem (2.20) is non-convex and difficult to solve, but it has better recovery performance than ℓ_1 regularization. Recently, efficient algorithms have been proposed to resolve the above non-convex problems. For example, [58] proposed a fast iterative half thresholding algorithm for the $\ell_{1/2}$ regularization problem.

Denoising Matching Pursuit Algorithms

The second kind of denoising recovery algorithms are designed based on OMP. For example, regularized OMP (ROMP) [59] is proposed to incorporate the property of convex relaxation by selecting only the comparable coordinates of the relevance vector $\mathbf{A}^H \mathbf{r}_{t-1}$. Then, Compressive Sampling Matching Pursuit (CoSaMP) [60] is proposed to reduce the effect of noise by retaining only the largest entries in the LS estimated signal. Subsequently, Subspace Pursuit (SP) [61] is proposed to achieve a similar reconstruction accuracy as convex relaxation by obtaining a K -dimensional hyperplane closer to \mathbf{y} after each iteration. Meanwhile, it has been proved that, if the minimum magnitude of the nonzero elements in \mathbf{x} satisfies a certain condition, OMP can exactly reconstruct the support of the sparse signal from noisy measurements with high probability [62] [63].

Iterative Thresholding Algorithms

Another kind of recovery algorithm is the iterative thresholding algorithms, e.g., the iterative hard thresholding (IHT) algorithm [64] and the iterative soft thresholding (IST) algorithm [65].

The IHT algorithm solves the minimization problem (2.16) in the OMP algorithm using the gradient method, i.e., at each iteration the estimated signal is updated by

$$\boldsymbol{\theta}^{[t+1]} = H_s \left(\boldsymbol{\theta}^{[t]} + \mathbf{A}^T (\mathbf{y} - \mathbf{A} \boldsymbol{\theta}^{[t]}) \right), \quad (2.21)$$

where $\boldsymbol{\theta}^{[t]}$ is the estimated signal in the t^{th} iteration with $\boldsymbol{\theta}^{[0]} = \mathbf{0}$, $H_s(\mathbf{x})$ is a non-linear

operator that sets all but the largest (in magnitude) s elements of \mathbf{x} to zero, and a possible stopping criteria is $\|\mathbf{y} - \mathbf{A}\boldsymbol{\theta}^{[t]}\|_2 \leq \epsilon$, where ϵ is decided by the required estimation error.

The IST algorithm iteratively solves the ℓ_1 regularization problem in (2.20) when $p = 1$, i.e., at each iteration the estimated signal is updated by

$$\boldsymbol{\theta}^{[t+1]} = S_\lambda (\boldsymbol{\theta}^{[t]} + \mathbf{A}^T(\mathbf{y} - \mathbf{A}\boldsymbol{\theta}^{[t]})) , \quad (2.22)$$

where $S_\lambda(\mathbf{x})_j = S_\lambda(x_j)$ is the soft thresholding function

$$S_\lambda(x) = \begin{cases} x - \frac{\lambda}{2}, & \text{if } x > \frac{\lambda}{2} \\ 0, & \text{if } |x| \leq \frac{\lambda}{2} \\ x + \frac{\lambda}{2}, & \text{if } x < -\frac{\lambda}{2} \end{cases} , \quad (2.23)$$

and λ is the regularization parameter in (2.20).

2.2 Analog Compressed Sensing

Recently, the development of wideband communication technology has pushed the Nyquist-rate ADC systems to their performance limits. However, in some application scenarios, the signals of interest contain only a small number of significant frequencies relative to the band limit. In other words, the analog signal is sparse in the frequency domain, thus CS can be used to reduce the sampling rate. However, CS was initially proposed for discrete signals, so it is necessary to extend the CS theory to the analog domain.

So far, several analog CS methods have been proposed, where AIC [1] and MWC [2] form the basis for the development of analog CS. The details about AIC, MWC and other analog CS methods are stated as follows.

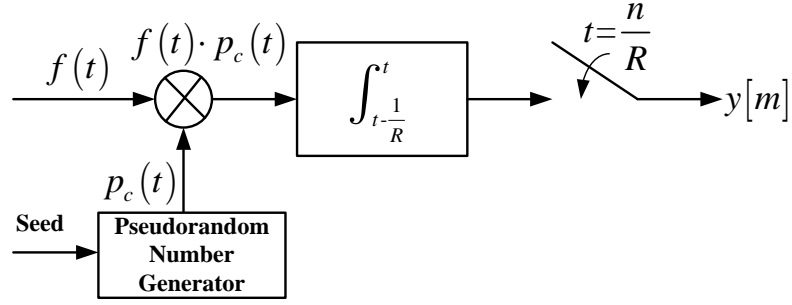


Figure 2.1: Block diagram of AIC [1].

2.2.1 AIC Method

Signal Model

AIC is proposed for the following multi-tone signal

$$f(t) = \sum_{\omega \in \Omega} a_{\omega} e^{-j2\pi\omega t}, \quad t \in [0, 1), \quad (2.24)$$

where Ω is a set of K integer-valued frequencies that satisfies

$$\Omega \subset \{0, \pm 1, \pm 2, \dots, \pm(W/2 - 1), W/2\}, \quad (2.25)$$

where $W/2$ is a positive integer which exceeds the highest frequency of signal $f(t)$, and a_{ω} denotes the amplitude of signal. Here, the number of active tones K is assumed to be much smaller than the bandwidth W . In other words, the signal $f(t)$ is K -sparse in the frequency domain.

System Description

Figure 2.1 shows the block diagram of AIC. Specifically, the input signal $f(t)$ is firstly modulated by multiplying with a high-rate pseudorandom sequence $p_c(t)$, which smears the tones across the entire spectrum. Then, the mixed signal $f(t) \cdot p_c(t)$ is passed through an integrator, which is a kind of low pass filter. Finally, the filtered signal is sampled with an ADC at rate $1/R$, where $R = O(K \log(W/K))$.

Mathematical Analysis

The expression for the pseudorandom sequence $p_c(t)$ is

$$p_c(t) = \varepsilon_n, \quad t \in \left[\frac{n}{W}, \frac{n+1}{W} \right), \quad n = 0, 1, \dots, W-1, \quad (2.26)$$

where ε_n is a random number that takes values ± 1 with equal probability. Then, the expression for the output signal sequence $y_m = y[m]$ is

$$y_m = \int_{m/R}^{(m+1)/R} f(t) p_c(t) dt, \quad m = 0, 1, \dots, R-1. \quad (2.27)$$

According to [1], the expression for y_m in the frequency domain is

$$\mathbf{y} = \mathbf{H}\mathbf{F}_s = \mathbf{A}\mathbf{s}, \quad (2.28)$$

where the $R \times W$ matrix \mathbf{H} corresponds to the integrator, and the r^{th} row of \mathbf{H} contains W/R consecutive entries starting from column $rW/R + 1$, where $r = 0, 1, \dots, R-1$. For example, when $R = 3$ and $W = 12$, we have

$$\mathbf{H} = \begin{bmatrix} 1 & 1 & 1 & 1 & & & & & & & & \\ & & & & 1 & 1 & 1 & 1 & & & & \\ & & & & & & & & 1 & 1 & 1 & 1 \end{bmatrix}. \quad (2.29)$$

When R does not divide W , matrix \mathbf{H} will have fractional elements in some of its columns.

An example with $R = 3$ and $W = 7$ is

$$\mathbf{H} = \begin{bmatrix} 1 & 1 & 1/3 & & & & \\ & 2/3 & 1 & 2/3 & & & \\ & & 1/3 & 1 & 1 & & \end{bmatrix}. \quad (2.30)$$

The $W \times W$ matrix \mathbf{D} corresponds to the pseudorandom sequence and is expressed as

$$\mathbf{D} = \begin{bmatrix} \varepsilon_0 & & & \\ & \varepsilon_1 & & \\ & & \ddots & \\ & & & \varepsilon_{W-1} \end{bmatrix}. \quad (2.31)$$

The $W \times W$ matrix \mathbf{F} is a permuted discrete Fourier transform (DFT) matrix, i.e.,

$$\mathbf{F} = \frac{1}{\sqrt{W}} [e^{-j2\pi n\omega/W}]_{n,\omega}, \quad (2.32)$$

where $n = 0, 1, \dots, W-1$ and $\omega = 0, \pm 1, \dots, \pm(W/2-1), W/2$. The $W \times 1$ vector \mathbf{s} is the coefficient vector of $f(t)$ in the DFT basis.

Recovery Algorithms for AIC

Finally, the signal $f(t)$ or the coefficient vector \mathbf{s} can be successfully recovered from (2.28) via the traditional BP or OMP algorithm. Although the authors in [1] have proposed a windowing technique to capture nonperiodic multi-tone signals, AIC is not effective to capture a wideband signal [66].

2.2.2 MWC Method

Since AIC is proposed for multi-tone signals, however, the model of multi-tone signal is too ideal and far from practical wideband signals. Thus, authors in [2] proposed MWC for the more practical multi-band signal.

Signal Model

As illustrated in Figure 2.2, the frequency support of a multi-band signal resides within several continuous intervals spreading over a very wide spectrum. A simple example for

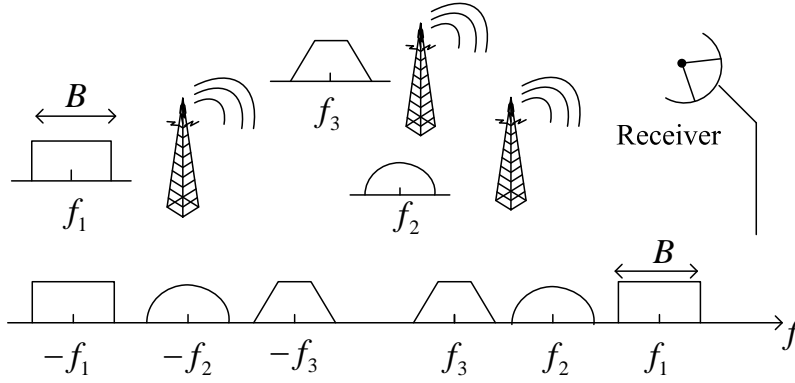


Figure 2.2: Illustration of the multi-band signal.

continuous-time multi-band signal is

$$x(t) = \sum_{i=1}^I \sqrt{E_i B} \text{sinc}(B(t - \tau_i)) \cos(2\pi f_i(t - \tau_i)), \quad (2.33)$$

where $\text{sinc}(x) = \sin(\pi x)/(\pi x)$, B is the bandwidth of each band in the multi-band signal, I is the number of the bands in the multi-band signals, E_i are the energy coefficients, and τ_i are the time offsets. Here, we assume that $x(t)$ is bandlimited to $\mathcal{F} = [-1/2T, 1/2T]$, and the Fourier transform of $x(t)$ is

$$X(f) = \int_{-\infty}^{\infty} x(t) e^{-j2\pi f t} dt. \quad (2.34)$$

System description

Figure 2.3 shows the system structure of MWC, where the input signal $x(t)$ enters m channels simultaneously. In the i^{th} channel, $x(t)$ is multiplied by a mixing function $p_i(t)$, which is T_p -periodic. Specifically, $p_i(t)$ is a piecewise constant function that alternates between the levels ± 1 for each of M equal time intervals. The expression for $p_i(t)$ is

$$p_i(t) = \alpha_{ik}, kT_p/M \leq t \leq (k+1)T_p/M, 0 \leq k \leq M-1, \quad (2.35)$$

where $\alpha_{ik} \in \{+1, -1\}$. After mixing, the signal spectrum is truncated by a low-pass filter (LPF) with cutoff $1/(2T_s)$ and the filtered signal is sampled at rate $1/T_s$.

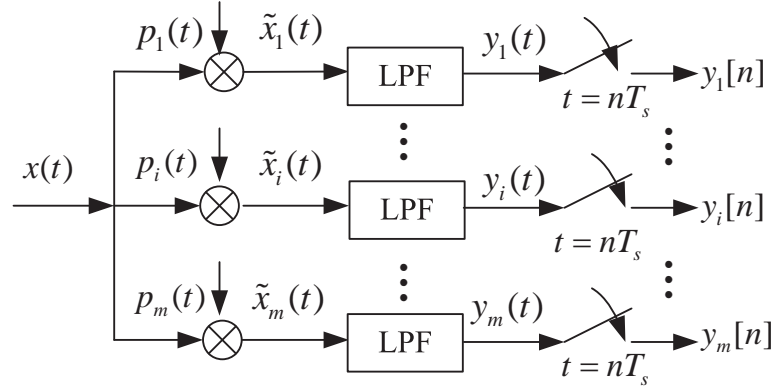


Figure 2.3: Block diagram of MWC [2].

Mathematical Analysis

Since $p_i(t)$ is T_p -periodic, it has a Fourier expansion

$$p_i(t) = \sum_{l=-\infty}^{\infty} a_{il} e^{j2\pi lt/T_p}, \quad (2.36)$$

where the coefficient a_{il} is expressed as

$$a_{il} = \frac{1}{T_p} \int_0^{T_p} p_i(t) e^{-j2\pi lt/T_p} dt. \quad (2.37)$$

Then, the Fourier transform of the mixed signal $\tilde{x}_i(t) = x(t)p_i(t)$ is

$$\begin{aligned} \tilde{X}_i(f) &= \int_{-\infty}^{\infty} x(t) \left(\sum_{l=-\infty}^{\infty} a_{il} e^{j2\pi lt/T_p} \right) e^{-j2\pi ft} dt \\ &= \sum_{l=-\infty}^{\infty} a_{il} \int_{-\infty}^{\infty} x(t) e^{-j2\pi(f-l/T_p)t} dt \\ &= \sum_{l=-\infty}^{\infty} a_{il} X(f - lf_p) \end{aligned} \quad (2.38)$$

where $f_p = 1/T_p$. Thus, $\tilde{X}_i(f)$ is a linear combination of f_p -shifted copies of $X(f)$.

The LPF is supposed to be ideal, thus the discrete-time Fourier transform (DTFT) of the sample sequence $y_i[n]$ is expressed as

$$Y_i(e^{j2\pi f T_s}) = \sum_{l=-L_0}^{L_0} a_{il} X(f - lf_p), \quad f \in \mathcal{F}_s, \quad (2.39)$$

where $\mathcal{F}_s = [-f_s/2, f_s/2]$ and $f_s = 1/T_s$, L_0 is chosen as the smallest integer such that the sum contains all the nonzero contributions of $X(f)$ over \mathcal{F}_s , i.e.,

$$-f_s/2 + (L_0 + 1)f_p \geq f_{nyq} \Rightarrow L_0 = \lceil \frac{f_{nyq} + f_s}{2f_p} - 1 \rceil, \quad (2.40)$$

where $f_{nyq} = 1/T$.

Since equation (2.39) is the key to the recovery of signal $x(t)$, expression (2.39) is rewritten into the following matrix form for convenience

$$\mathbf{y}(f) = \mathbf{A}\mathbf{z}(f), f \in \mathcal{F}_s, \quad (2.41)$$

where $\mathbf{y}(f)$ is a vector of length m with $y_i(f) = Y_i(e^{j2\pi f T_s})$. The unknown vector $\mathbf{z}(f) = [z_1(f), \dots, z_L(f)]^T$, where $L = 2L_0 + 1$ and

$$z_i(f) = X(f + (i - L_0 - 1)f_p), 1 \leq i \leq L, f \in \mathcal{F}_s. \quad (2.42)$$

The $m \times L$ matrix \mathbf{A} contains the coefficients a_{il} , i.e.,

$$A_{il} = a_{i,-l} = a_{il}^*. \quad (2.43)$$

The coefficient a_{il} is calculated as follows

$$\begin{aligned} a_{il} &= \frac{1}{T_p} \int_0^{T_p/M} \sum_{k=0}^{M-1} \alpha_{ik} e^{-j\frac{2\pi}{T_p} l(t+k\frac{T_p}{M})} dt \\ &= \frac{1}{T_p} \sum_{k=0}^{M-1} \alpha_{ik} e^{-j\frac{2\pi}{M} lk} \int_0^{T_p/M} e^{-j\frac{2\pi}{T_p} lt} dt \end{aligned} \quad (2.44)$$

Denote d_l as

$$d_l = \frac{1}{T_p} \int_0^{T_p/M} e^{-j\frac{2\pi}{T_p} lt} dt = \begin{cases} \frac{1}{M}, & l = 0 \\ \frac{1-\theta^l}{2j\pi l}, & l \neq 0 \end{cases} \quad (2.45)$$

where $\theta = e^{-j2\pi/M}$, thus we have

$$a_{il} = d_l \sum_{k=0}^{M-1} \alpha_{ik} \theta^{lk}. \quad (2.46)$$

Let \mathbf{F}_i be the i^{th} column of the DFT matrix, as stated in (2.32). Let $\mathbf{F}' = [\mathbf{F}_{L_0}, \dots, \mathbf{F}_{-L_0}]$, i.e., \mathbf{F}' is a reordered column subset of the DFT matrix. Then, (2.41) can be written as

$$\mathbf{y}(f) = \mathbf{S}\mathbf{F}'\mathbf{D}'\mathbf{z}(f), \quad f \in \mathcal{F}_s, \quad (2.47)$$

where \mathbf{S} is a $m \times M$ sign matrix, with $\mathbf{S}_{ik} = \alpha_{ik}$, and $\mathbf{D}' = \text{diag}(d_{L_0}, \dots, d_{-L_0})$.

Recovery Algorithm for MWC

Recovery of $x(t)$ from the sequences $y_i[n]$ boils down to recovery of the sparsest $\mathbf{z}(f)$ from (2.47) for every $f \in \mathcal{F}_s$. However, since $f \in \mathcal{F}_s$ has infinite cardinality, resolving $\mathbf{z}(f)$ from (2.47) is an infinite measurement vectors (IMV) problem, which requires an independent treatment for infinitely many systems. To avoid this difficulty of IMV, authors in [2] propose a continuous to finite (CTF) method to resolve (2.47). The CTF method begins with the construction of a finite frame for $\mathbf{y}(\mathcal{F}_s)$. Then, it finds the unique sparsest solution to the multiple measurement vectors (MMV) system $\mathbf{V} = \mathbf{A}\mathbf{U}$. The main result is that the support of $\mathbf{z}(\mathcal{F}_s)$, i.e., $S = \text{supp}(\mathbf{z}(\mathcal{F}_s))$ equals the support of \mathbf{U} , i.e., $\text{supp}(\mathbf{U})$. In other words, the support recovery is accomplished by solving only a finite-dimensional problem.

Specifically, the frame \mathbf{V} can be obtained via firstly computing matrix \mathbf{Q}

$$\mathbf{Q} = \int_{f \in \mathcal{F}_s} \mathbf{y}(f)\mathbf{y}^H(f)df = \sum_{n=-\infty}^{+\infty} \mathbf{y}[n]\mathbf{y}^T[n], \quad (2.48)$$

then any matrix \mathbf{V} satisfying $\mathbf{Q} = \mathbf{V}\mathbf{V}^H$ is a frame for $\mathbf{y}(\mathcal{F}_s)$. The signal support S of $\mathbf{z}(\mathcal{F}_s)$ can be recovered from the MMV problem $\mathbf{V} = \mathbf{A}\mathbf{U}$. Once the signal support is obtained, we have

$$\mathbf{z}_S[n] = \mathbf{A}_S^+ \mathbf{y}[n], \text{ and } z_i[n] = 0, i \notin S. \quad (2.49)$$

where $\mathbf{z}[n] = [z_1[n], \dots, z_L[n]]^T$ and $z_i[n]$ is the inverse-DTFT of $z_i(f)$. In other words, the sequences $z_i[n]$ are generated at the input rate f_s . Therefore, the sequences $z_i[n]$ are

first zero padded to the Nyquist rate, i.e.,

$$\tilde{z}_i[\tilde{n}] = \begin{cases} z_i[n], & \tilde{n} = nL, n \in \mathbb{Z} \\ 0, & \text{otherwise} \end{cases}. \quad (2.50)$$

Then, $\tilde{z}_i[\tilde{n}]$ is interpolated using an ideal digital filter with impulse $h_I[n]$, and then the interpolates sequences are modulated in time and summed, i.e.,

$$x[n] = x(nT) = \sum_{i \in S} (\tilde{z}_i[n] * h_I[n]) e^{j2\pi f_p nT}. \quad (2.51)$$

Comparison between AIC and MWC

From Figure 2.3 and Figure 2.1, we can find that MWC seems to be a parallel version of AIC, but their signal models and reconstruction algorithms strongly differ. Authors in [66] pointed out that, both AIC and MWC are based on the general concept of random filtering [3], but employ significantly different sampling functions. Specifically, the analog filter in AIC is an ideal integrator with impulse response $h(t) = \text{rect}(2Rt - 1)$, where

$$\text{rect}(x) = \begin{cases} 1, & \text{for } -1 \leq x \leq 1 \\ 0, & \text{otherwise} \end{cases}. \quad (2.52)$$

However, the analog filter in MWC is an ideal low pass filter with impulse response $h'(t) = \frac{1}{2T_s} \text{sinc}(t/2T_s)$.

2.2.3 Other Analog CS Methods

As mentioned in the comparison between AIC and MWC, both AIC and MWC are based on the concept of random filtering [3], whose block diagram is shown in Figure 2.4. Specifically, the signal s is captured by convolving it with a random-tap finite impulse response (FIR) filter h , then the filtered signal is downsampled to obtain a compressed representation y . However, AIC and MWC employ considerably different sampling functions [66]. In addition, different aspects of AIC and MWC have also been investigated.

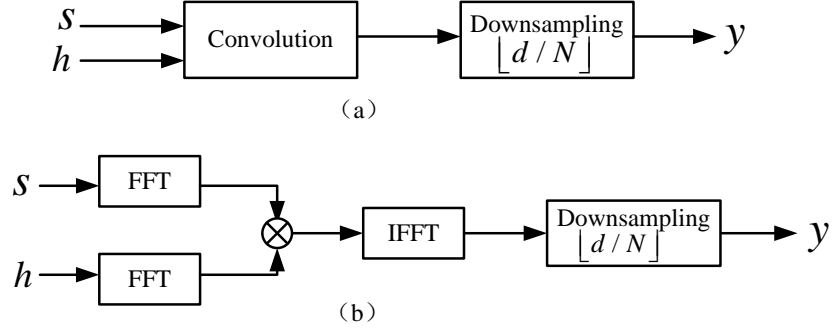


Figure 2.4: Block diagram of random filters, (a) using convolution, (b) using FFT/IFFT. [3]

For example, [67] proposes a segmented CS to reduce the hardware complexity of the parallel version of AIC, while [68] [69] utilizes structured matrix to reduce the hardware complexity of MWC, and [70] investigates the impact of using non-ideal element in MWC.

Based on Gabor frames, authors in [71] extend the MWC method to the multipulse signals, which are sparse in the time domain. Furthermore, for the signals that are not bandlimited but have a finite number of degrees of freedom per unit of time, e.g., streams of Diracs and nonuniform splines, authors in [72] stated that such signals can be successfully sampled at the rate of innovation with an appropriate kernel.

2.3 Applications of Compressed Sensing

In this section, we will firstly introduce the initial application of CS in imaging, and then we will mainly focus on the applications of CS in wireless communications.

2.3.1 Compressive Imaging

The basic idea behind image compression is that the image is firstly transformed into an appropriate basis and then only the important expansion coefficients are coded. However, this process has a drawback, i.e., most of the data we acquired are thrown away.

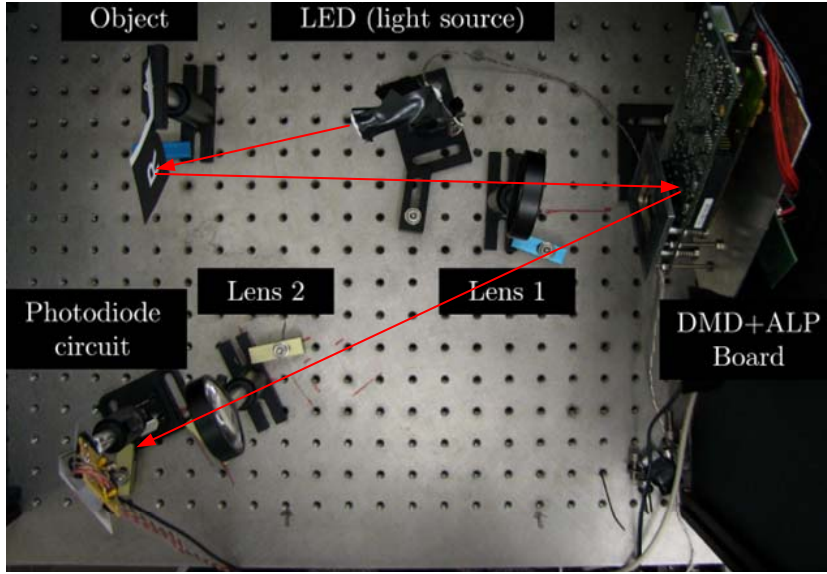


Figure 2.5: Aerial view of the single-pixel CS camera in the lab [4].

Fortunately, CS provides a way to directly measure the part that will not end up being thrown away.

Based on the CS theory, authors in [4] [10] achieved the sub-Nyquist image acquisition by developing a single-pixel camera as shown in Figure 2.5. Specifically, the object is front illuminated by an LED light, and then the light-field is focused by biconvex Lens 1 onto a digital micromirror device (DMD) consisting of an array of N tiny mirrors. Each mirror rotates about a hinge and can be positioned in one of two states, i.e., $+12^\circ$ (degrees) and -12° from horizontal. Thus, light falling on the DMD may be reflected in two directions depending on the orientation of the mirrors. After that, the reflected light is collected by biconvex Lens 2 and focused onto a single photon detector.

Mathematically, the output voltage of the photo detector $y[m]$ can be interpreted as the inner product of the N -pixel image \mathbf{x} corresponding to the N mirrors with a measurement basis vector ϕ_m . That is to say,

$$y[m] = \langle \mathbf{x}, \phi_m \rangle, \quad (2.53)$$

where $\phi_m = \mathbf{1}_{\{\rho_m = +12^\circ\}}$, in which ρ_m denotes the positions of the N mirrors for the m^{th} measurement pattern, and $\mathbf{1}$ is the $N \times 1$ indicator vector. Let M denote the number of measurements, then we have

$$\mathbf{y} = \Phi \mathbf{x}, \quad (2.54)$$

where $\mathbf{y} = [y[1], \dots, y[M]]^T$ and $\Phi = [\phi_1, \dots, \phi_M]^T$. Then, the image \mathbf{x} can be successfully recovered from (2.54) using the CS recovery algorithms.

2.3.2 Compressed Sensing for Wireless Communications

In this work, we mainly focus on the applications of CS in wireless communications, such as in wireless sensor networks and cognitive radio networks.

Distributed Compressed Sensing for Wireless Sensor Networks

In WSNs, the energy and communication bandwidth are limited and the data in neighboring sensors are often spatially and/or temporally correlated. Authors in [19] developed the distributed compressed sensing (DCS) and reduced the number of required measurements by exploiting the joint sparsity among different sensor data. Based on CS, authors in [73] greatly reduce the number of wake-up sensors for the sparse event detection problem in WSNs. Furthermore, exploiting the spatiotemporal correlation of sensor readings, authors in [74] and [75] improve the energy efficiency of WSNs by reducing the number of required transmissions based on the CS theory.

Compressed Sensing for Channel Estimation

To reduce the number of pilots and increase spectral efficiency, authors in [76] propose a new channel estimation technique based on the CS theory, by exploiting the delay-Doppler sparsity of the doubly selective wireless channels in multicarrier systems. Based on the

CS theory, the authors in [77] show that a reduced number of random projections of the received ultra-wideband (UWB) signal contains most of the relevant information, which are not only useful for signal reconstruction but also useful for UWB channel parameter estimation. Furthermore, extensive numerical results show that the proposed approach in [77] outperforms the traditional detector using just 30% of the ADC resources.

Compressed Sensing for Wideband Spectrum Sensing in Cognitive Radio

Capitalizing on the sparsity of wideband signals in frequency domain, the authors of [17] firstly introduce CS into cognitive radio networks to resolve the challenge of extremely high sampling rate faced by wideband spectrum sensing. However, the method in [17] is based on the discrete signals sampled at the Nyquist rate, which contradicts the initial objective. Then, the authors in [21] point out the above problem and propose a parallel structure to sample the analog signal at a sub-Nyquist rate.

In summary, this chapter briefly introduces the basic theory and applications of both discrete CS and analog CS, which provide the preliminary knowledge for the following chapters. Furthermore, to make the thesis more easy to follow, we will start with the applications of discrete CS in WSNs in the next chapter.

Chapter 3

Compressed Network Coding for Distributed Data Storage in WSNs

Since CS is originally proposed for discrete signals, we will firstly discuss the applications of discrete CS in wireless communications, especially in WSNs. In this Chapter, we aim to improve the energy efficiency of WSNs deployed in catastrophic scenarios.

3.1 Introduction

WSNs [78] [25] [31] are widely deployed to detect events, monitor environmental conditions, track multiple targets and achieve other application functionalities. One of the great challenges faced by WSNs is how to collect data with high energy efficiency, especially in hostile, harsh and catastrophic environments, where the network is vulnerable or inaccessible. In such scenarios, it is impossible to have static and powered sink nodes which are responsible for collecting data from the distributed sensors. In addition, the sensor nodes are also unreliable. To resolve this problem, DDS [29] [79] [80] (also termed as data persistence in [30] [81] [82]) is proposed for reliable data communication even if large numbers of sensor nodes fail to function. Specifically, the sensed data of the DDS are

stored with redundancy in the network, so that the mobile sink node is able to reconstruct all the sensed data of the whole WSN by visiting only a small number of the surviving nodes.

In essence, the problem of DDS is equivalent to the reliable communication problem in an erasure channel. Thus, erasure coding provides a potential way to resolve the DDS problem. Specifically, an erasure code transforms a source message of m symbols into a longer code with n symbols, and then the original symbols can be decoded from a small subset of the n encoded symbols. For example, Fountain Codes (FC) [83] [84], one class of the erasure codes, are adopted in a decentralized fashion in [29] [30] to encode the sensor readings. Then, the sensed data can be reconstructed from any $m(1 + \varepsilon)$ FC encoded symbols, where $\varepsilon > 0$ is a small constant. In addition, Luby Transform (LT) codes [82] [85], which is one class of the practical FC, are utilized in a distributed way to improve the decoding performance of DSS [81].

This chapter focuses on the energy efficiency problem of DDS in WSNs. In terms of the energy consumption for DDS, the data dissemination consisting of both data transmission and data reception accounts for the largest part. It is worth mentioning that, for short-range communication in WSNs, the energy costs for data transmission and data reception are nearly the same [25] [86]. Therefore, one effective method to improve the energy efficiency of DDS in WSNs is to reduce both the number of data transmissions and the number of data receptions during the data dissemination process.

To date, there have been two potential solutions to reduce the number of transmissions. First, compressive data persistence (CDP) [74] and CStorage [75] reduce the number of required transmissions by exploiting the spatiotemporal correlation of sensor readings [18] and utilizing the CS theory [6] [7] [9]. Second, Random Linear Network Coding (RLNC) [87] is proved to be able to decrease the number of transmissions [88] [89]. In addition, real network codes [90] and NetCompress [91] are specially proposed for WSNs. However,

all the above schemes only focus on reducing the number of data transmissions Nt_{tot} , without considering the number of data receptions Nr_{tot} , which have almost the same energy cost as data transmissions for short-range communications [25] [86].

To simultaneously reduce Nt_{tot} and Nr_{tot} , this chapter proposes a CNCDS scheme. We prove that the measurement matrix of the CNCDS scheme guarantees good CS recovery performance. Based on RGG theory, we derive the expressions for Nt_{tot} and Nr_{tot} to verify the efficiency of the CNCDS scheme. Furthermore, based on the theoretical expressions for Nt_{tot} and Nr_{tot} , we propose an adaptive CNCDS scheme, where the forwarding probability is adjusted according to the number of each node's neighbors. Simulation results demonstrate that, compared with the conventional ICStorage scheme, the CNCDS scheme decreases Nt_{tot} , Nr_{tot} , and the CS recovery mean squared error (MSE) by up to 55%, 74%, and 76% respectively. In addition, the adaptive CNCDS scheme further reduces Nt_{tot} and Nr_{tot} by up to 63% and 32% respectively in comparison with the CNCDS scheme.

The rest of this chapter is organized as follows. Section 3.2 briefly introduces signal model and network deployment. Section 3.3 presents the proposed CNCDS scheme, including its packet format, procedures, and the property of its measurement matrix, then the CNCDS scheme is discussed under more practical conditions. Section 3.4 derives the expressions for the number of transmissions Nt_{tot} and the number of receptions Nr_{tot} respectively based on the RGG theory. Section 3.5 describes the adaptive CNCDS scheme. Section 3.6 evaluates the performance of the CNCDS scheme and the adaptive CNCDS scheme. Finally, Section 3.7 concludes this chapter.

3.2 Signal Model and Network Deployment

This section describes the signal model for the sensed data and the network deployment for WSNs.

3.2.1 Signal Model

Consider a WSN composed of N nodes and the sensed data are $\mathbf{x} = [x_1, \dots, x_N]^T$, with x_i representing the reading of the i^{th} sensor node. Since the sensed data \mathbf{x} are often spatially and/or temporally correlated, data \mathbf{x} are compressible in an orthogonal basis Ψ , e.g., DCT basis. The formulation of the $M \times N$ measurement matrix Φ and the $M \times 1$ measurement vector \mathbf{y} will be stated in Section 3.3.4. Then, the signal model of the CNCDS scheme is $\mathbf{y} = \Phi\mathbf{x} = \Phi\Psi\boldsymbol{\theta}$, which coincides with that of CS.

To make the signal model more explicit, the definition of a compressible signal is stated as follows. Signal \mathbf{x} is referred to be compressible if its coefficient vector $\boldsymbol{\theta}$ decays according to a power law, i.e., the i^{th} largest transform coefficient satisfies

$$|\boldsymbol{\theta}|_{(i)} \leq R \times i^{-1/p}, \quad (3.1)$$

where $1 \leq i \leq N$, R is the radius of the weak ℓ_p ball which consists of vector $\boldsymbol{\theta}$ [7] [9], and $0 < p < 1$ represents the speed of decay: the smaller the p , the faster the decay. Let $\boldsymbol{\theta}_K$ denote the truncated version of the vector $\boldsymbol{\theta}$ by taking the K largest transform coefficients and setting the remaining coefficients to zero. The approximation error is

$$\|\boldsymbol{\theta} - \boldsymbol{\theta}_K\|_2 \leq \varsigma_p \times R \times (K + 1)^{1/2-1/p}, \quad (3.2)$$

where ς_p is a constant which only depends on p .

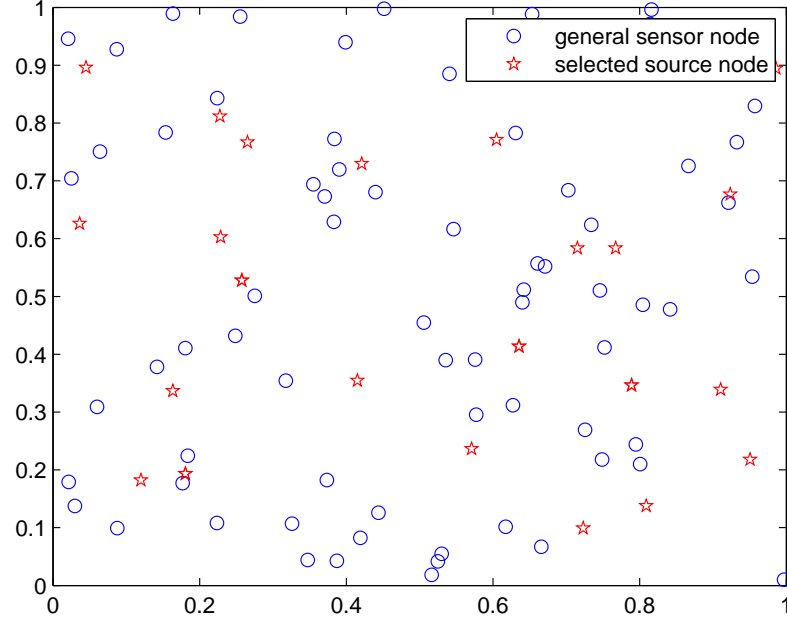


Figure 3.1: Illustration of the network deployment, where $N_s = 30$ nodes of the total $N = 100$ nodes are randomly selected as source nodes.

3.2.2 Network Deployment

Consider a WSN with N nodes which are randomly and uniformly deployed over a normalized field of size $S = 1 \times 1$. Assume that all the N nodes have an identical transmission range r_t , and two nodes can communicate with each other if their Euclidian distance d is smaller than r_t . To ensure network connectivity, r_t should satisfy $r_t^2 > S \cdot \ln(N)/(\pi N)$ [26]. Based on the compressibility of the sensed data and the CS theory, only N_s nodes are randomly selected as source nodes to reduce the number of data transmissions and receptions. Figure 3.1 shows an example of the network deployment with $N = 100$ nodes randomly distributed in an area of size $S = 1 \times 1$, where $N_s = 30$ nodes are randomly selected as source nodes (denoted by the red pentagrams, whereas, the blue circle denotes the unselected sensor node).

3.3 Proposed CNCDS Scheme

This section presents the proposed CNCDS scheme. Firstly, Section 3.3.1 generally describes the proposed CNCDS scheme, whose detailed procedures are presented in Section 3.3.2. Then, Section 3.3.3 discusses the choice of two parameters N_s and P_0 . Section 3.3.4 illustrates the forming process of the CNCDS scheme's measurement matrix. Section 3.3.5 proves that the formed measurement matrix guarantees good CS recovery performance. Finally, Section 3.3.6 discusses the CNCDS scheme under more practical situations.

3.3.1 Overall Description of CNCDS Scheme

In this chapter, we assume that the communication in the whole network is synchronized and slotted. Firstly, at the beginning of the CNCDS scheme, i.e., the initialization stage, each sensor node i multiplies its reading x_i by a random coefficient $\varphi_{i,i}$, which is chosen to be +1 or -1 randomly with equal probability. Then, node i forms its initial packet, denoted by a structure variable $\mathbf{r}(i)$, which is made up of the coefficient set $\mathbf{r}(i).\mathbf{a1}=[\varphi_{i,i}]$, the node ID set $\mathbf{r}(i).\mathbf{a2}=[i]$ and the data multiplied with the coefficient $\mathbf{r}(i).\mathbf{a3}=\varphi_{i,i} \times x_i$.

Then, the source node broadcasting stage is started, where each sensor node randomly selects itself as a source node with probability P_1 and then broadcasts their initial packets. The value of P_1 is discussed in Section 3.3.3. If the reception node i does not share any node ID with the corresponding transmission node j , i.e.,

$$(\mathbf{r}(i).\mathbf{a2}) \cap (\mathbf{r}(j).\mathbf{a2}) = \emptyset, \quad (3.3)$$

then $\mathbf{r}(j)$ is merged into $\mathbf{r}(i)$ with $\mathbf{r}(i).\mathbf{a1} = [\mathbf{r}(i).\mathbf{a1}] \cup [\mathbf{r}(j).\mathbf{a1}]$, $\mathbf{r}(i).\mathbf{a2} = [\mathbf{r}(i).\mathbf{a2}] \cup [\mathbf{r}(j).\mathbf{a2}]$ and $\mathbf{r}(i).\mathbf{a3} = \mathbf{r}(i).\mathbf{a3} + \mathbf{r}(j).\mathbf{a3}$. Thus, we can use the packet format in Figure 3.2 to represent the packet of each node, which includes the header and the data. Specifically, the header consists of a set of 1-bit coefficients $\varphi_{i,j}$ and a set of the $\lceil \log_2^N \rceil$ -bit node IDs.

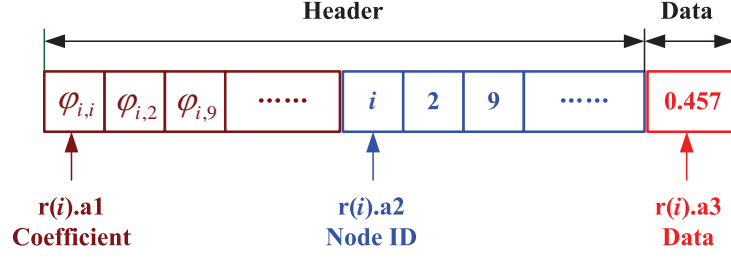


Figure 3.2: Packet format of the i^{th} node in CNCDS scheme.

The size of the data field is 32 bits or 64 bits depending on the precision requirement.

Thirdly, the reception nodes in the source broadcasting stage will forward the merged packet to its neighbors with probability P_0 . Again, the node i that hears the transmitted packet $\mathbf{r}(j)$ will examine the reception condition (3.3). If the condition (3.3) is satisfied, then $\mathbf{r}(j)$ will be merged into $\mathbf{r}(i)$ as aforementioned. Otherwise, node i will not receive $\mathbf{r}(j)$, i.e., $\mathbf{r}(j)$ will not be merged into $\mathbf{r}(i)$. Due to the small forwarding probability ($P_0 < 1$) and the reception condition (3.3), the transmission will cease after the intermediate reception nodes forward the received and merged packets for a few times.

After all the transmissions are finished, the mobile collector queries any M nodes to obtain the measurement matrix Φ and the measurement vector \mathbf{y} . Finally, the CS recovery algorithm, such as the BP algorithm [7] [46] or OMP algorithm [5], can be used to reconstruct all the sensor readings \mathbf{x} from $\mathbf{y} = \Phi\mathbf{x}$.

3.3.2 Procedures of CNCDS Scheme

To make the procedures more clear, Table 3.1 illustrates the pseudocode of the CNCDS scheme, which is made up of three stages: the initialization stage, the source node broadcasting stage and the intermediate node forwarding stage.

Table 3.1: Pseudocode of CNCDS Scheme**STAGE I. Initialization.**

for $i = 1$ **to** $i = N$
 Set $\varphi_{i,i}$ to be +1 or -1 randomly with equal probability;
 $\mathbf{r}(i).\mathbf{a1} = [\varphi_{i,i}]$; $\mathbf{r}(i).\mathbf{a2} = [i]$; $\mathbf{r}(i).\mathbf{a3} = \varphi_{i,i} \times x_i$;
end

STAGE II. Source Nodes Broadcasting.

N_s source nodes randomly choose themselves to broadcast their packets;
for $j = 1$ **to** $j = N_s$
for $i = 1$ **to** $i = N$
if (Node i hears $\mathbf{r}(j)$) && $((\mathbf{r}(i).\mathbf{a2}) \cap (\mathbf{r}(j).\mathbf{a2}) = \emptyset)$;
 $\mathbf{r}(i).\mathbf{a1} = [\mathbf{r}(i).\mathbf{a1}, \mathbf{r}(j).\mathbf{a1}]$; $\mathbf{r}(i).\mathbf{a2} = [\mathbf{r}(i).\mathbf{a2}, \mathbf{r}(j).\mathbf{a2}]$;
 $\mathbf{r}(i).\mathbf{a3} = \mathbf{r}(i).\mathbf{a3} + \mathbf{r}(j).\mathbf{a3}$;
else continue;
end
end
end

STAGE III. Intermediate Nodes Forwarding.

The reception nodes in Stage II broadcast their packets with probability P_0 ;
while There is a node j which forwards its packet $\mathbf{r}(j)$;
for $i = 1$ **to** $i = N$
if (Node i hears $\mathbf{r}(j)$) && $((\mathbf{r}(i).\mathbf{a2}) \cap (\mathbf{r}(j).\mathbf{a2}) = \emptyset)$;
 $\mathbf{r}(i).\mathbf{a1} = [\mathbf{r}(i).\mathbf{a1}, \mathbf{r}(j).\mathbf{a1}]$; $\mathbf{r}(i).\mathbf{a2} = [\mathbf{r}(i).\mathbf{a2}, \mathbf{r}(j).\mathbf{a2}]$;
 $\mathbf{r}(i).\mathbf{a3} = \mathbf{r}(i).\mathbf{a3} + \mathbf{r}(j).\mathbf{a3}$;
else continue;
end
end
 The reception nodes in the last forwarding choose themselves with
 probability P_0 to broadcast their received and merged packets;
end

The mobile collector queries any M nodes to obtain the measurement matrix Φ and the measurement vector \mathbf{y} .

Use the OMP algorithm to reconstruct all the sensor readings \mathbf{x} from $\mathbf{y} = \Phi\mathbf{x}$ from the structure variable \mathbf{r} .

3.3.3 Choice of Parameters N_s and P_0

Table 3.1 shows that the intermediate nodes in Stage III also have the opportunity to broadcast their own packets. Thus, to disseminate all the information throughout the network, less than N source nodes are needed, i.e., $N_s < N$. Meanwhile, $N_s \geq M$ is a necessary condition for ensuring that the rank of the measurement matrix is M [75], where M should satisfy $M \geq cK \log(N/K)$ based on the CS theory [6]- [9], with c being a small constant. Thus, we have $N_s \geq M \geq cK \log(N/K)$. In reality, to make $N_s \geq M$ is satisfied with high probability, the probability that each node chooses itself as a source node P_1 should satisfy $P_1 \geq P_1^*$, where P_1^* equals to the value which makes $Pr\{N_s \geq M\} = \sum_{n=M}^N C_N^n P_1^n (1 - P_1)^{N-n} \geq 0.99$.

The forwarding probability P_0 is required to be greater than P_0^* to ensure a high ratio $R(P_0)$ of nodes receiving a particular transmission [75], where P_0^* equals to the probability that a giant component appears in a random network. A giant component is a connected component containing a positive fraction of the entire graph's vertices [92]. Furthermore, it has been proved that a high $R(P_0)$, i.e., $P_0 > P_0^*$, is necessary to ensure that the rank of the measurement matrix is M with high probability [75]. Thus, we assume $P_0 > P_0^*$ is satisfied throughout this chapter.

3.3.4 Formulation of Measurement Matrix

To illustrate the forming process of the measurement matrix, we consider a small network with $N = 7$ nodes, as illustrated in Figure 3.3, where node 2 and node 7 are chosen to be the source nodes.

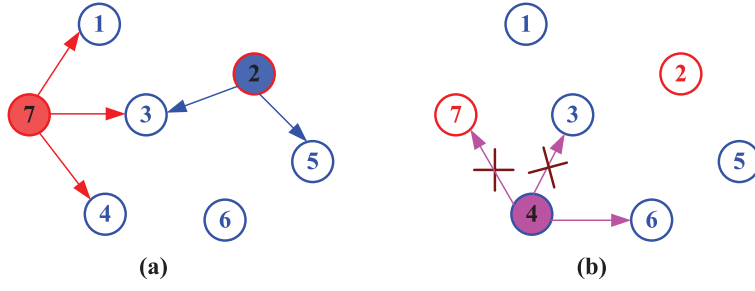


Figure 3.3: (a) Source nodes broadcasting process in Stage II, (b) Intermediate nodes forwarding process in Stage III.

After the initialization stage, the total measurement matrix Φ_t for all N nodes is

$$\Phi_t^I = \begin{bmatrix} \varphi_{1,1} & 0 & 0 & 0 & 0 & 0 & 0 \\ 0 & \varphi_{2,2} & 0 & 0 & 0 & 0 & 0 \\ 0 & 0 & \varphi_{3,3} & 0 & 0 & 0 & 0 \\ 0 & 0 & 0 & \varphi_{4,4} & 0 & 0 & 0 \\ 0 & 0 & 0 & 0 & \varphi_{5,5} & 0 & 0 \\ 0 & 0 & 0 & 0 & 0 & \varphi_{6,6} & 0 \\ 0 & 0 & 0 & 0 & 0 & 0 & \varphi_{7,7} \end{bmatrix}. \quad (3.4)$$

In stage II, as illustrated in Figure 3.3(a), node 7 broadcasts $\mathbf{r}(7)$ to node 1, node 3 and node 4. Similarly, node 2 broadcasts $\mathbf{r}(2)$ to node 3 and node 5. After Stage II is

finished, the matrix Φ_t becomes

$$\Phi_t^{\text{II}} = \begin{bmatrix} \varphi_{1,1} & 0 & 0 & 0 & 0 & 0 & \varphi_{1,7} \\ 0 & \varphi_{2,2} & 0 & 0 & 0 & 0 & 0 \\ 0 & \varphi_{3,2} & \varphi_{3,3} & 0 & 0 & 0 & \varphi_{3,7} \\ 0 & 0 & 0 & \varphi_{4,4} & 0 & 0 & \varphi_{4,7} \\ 0 & \varphi_{5,2} & 0 & 0 & \varphi_{5,5} & 0 & 0 \\ 0 & 0 & 0 & 0 & 0 & \varphi_{6,6} & 0 \\ 0 & 0 & 0 & 0 & 0 & 0 & \varphi_{7,7} \end{bmatrix}, \quad (3.5)$$

where $\varphi_{i,j}$ is the random coefficient of node i received from node j . Thus, we have $\varphi_{1,7} = \varphi_{3,7} = \varphi_{4,7} = \varphi_{7,7}$ and $\varphi_{3,2} = \varphi_{5,2} = \varphi_{2,2}$.

During stage III, as shown in Figure 3.3(b), node 4 is chosen (with probability P_0) to forward $\mathbf{r}(4)$ to its neighbors. Because node 4, node 3 and node 7 share the information of node 7, the packet of node 4 cannot be merged into node 3 or node 7. Then, the matrix Φ_t turns into

$$\Phi_t^{\text{III}} = \begin{bmatrix} \varphi_{1,1} & 0 & 0 & 0 & 0 & 0 & \varphi_{1,7} \\ 0 & \varphi_{2,2} & 0 & 0 & 0 & 0 & 0 \\ 0 & \varphi_{3,2} & \varphi_{3,3} & 0 & 0 & 0 & \varphi_{3,7} \\ 0 & 0 & 0 & \varphi_{4,4} & 0 & 0 & \varphi_{4,7} \\ 0 & \varphi_{5,2} & 0 & 0 & \varphi_{5,5} & 0 & 0 \\ 0 & 0 & 0 & \varphi_{6,4} & 0 & \varphi_{6,6} & \varphi_{6,7} \\ 0 & 0 & 0 & 0 & 0 & 0 & \varphi_{7,7} \end{bmatrix}, \quad (3.6)$$

where $\varphi_{6,4} = \varphi_{4,4}$, and $\varphi_{6,7} = \varphi_{4,7} = \varphi_{7,7}$. If node 6 is not chosen to forward its packet, then all the transmissions are finished.

If the mobile collector chooses node 2, node 5 and node 6 to collect data, then the

measurement matrix Φ is composed of the 2nd, 5th and 6th row of Φ_t in (3.6), i.e.,

$$\Phi = \begin{bmatrix} 0 & \varphi_{2,2} & 0 & 0 & 0 & 0 & 0 \\ 0 & \varphi_{5,2} & 0 & 0 & \varphi_{5,5} & 0 & 0 \\ 0 & 0 & 0 & \varphi_{6,4} & 0 & \varphi_{6,6} & \varphi_{6,7} \end{bmatrix}. \quad (3.7)$$

Then, the corresponding measurement vector is expressed as $\mathbf{y} = [\mathbf{r}(2).\mathbf{a3}, \mathbf{r}(5).\mathbf{a3}, \mathbf{r}(6).\mathbf{a3}]^T$.

3.3.5 Property of Measurement Matrix

Verifying the RIP condition in (2.2) for an arbitrary matrix is NP-hard, however, the recovery performance can be guaranteed as long as the rows of the sparse measurement matrix are linearly independent [15].

Theorem 3.1. *Assume that all the N sensor nodes of a randomly deployed WSN have an identical transmission range r_t , where $r_t^2 > S \cdot \ln(N)/(\pi N)$ with S being the size of the field in which the WSN is deployed. If the proposed CNCDS scheme is used to fulfill the DDS function, where the number of source nodes N_s is greater than or equal to the number of nodes visited by a mobile collector M , and the forwarding probability P_0 is greater than the probability P_0^* that a giant component appears in the WSN, then any M rows of the total measurement matrix Φ_t are linearly independent and the sensor readings can be successfully recovered from the measurements obtained by the mobile collector with high probability.*

Proof. As expressed in (3.4), after Stage I is finished, the rank of matrix Φ_t is $\text{rank}(\Phi_t) = N$. During Stage II and Stage III, the value of $\text{rank}(\Phi_t)$ will decrease by one if one of the following three situations happens.

The First Situation

Any row φ_k can be expressed as a linear combination of any other two or more rows.

Note that, according to the design of the CNCDS scheme, the entries of Φ_t satisfy

$$\varphi_{i,j} = \varphi_{j,j}, \quad (3.8)$$

for $i, j = 1, \dots, N$. Thus, φ_k can be linearly expressed by any other two or more rows $\varphi_{k_1}, \varphi_{k_l}, \dots, \varphi_{k_q}$ if and only if

$$\Lambda_k = \bigcup_{i=1}^q \Lambda_{k_i}, q = 2, \dots, N-1, \quad (3.9)$$

where $\Lambda_k = \{j \mid \varphi_{k,j} \neq 0\}$ and $\Lambda_{k_i} = \{j \mid \varphi_{k_i,j} \neq 0\}$. Based on the formulation of Φ_t , (3.9) may be satisfied if node k receives packets from nodes k_1, \dots, k_q . However, due to the reception condition (3.3) and the initialization stage, (3.9) can never be satisfied. As a matter of fact, the relation between Λ_k and Λ_{k_i} satisfies

$$\Lambda_k = k \cup \left(\bigcup_{i=1}^q \Lambda_{k_i} \right), \quad (3.10)$$

if node k hears nodes k_1, \dots, k_q . From (3.9) and (3.10), we can conclude that no row can be linearly expressed by other rows. In addition, the difference between (3.9) and (3.10) also illustrates the importance of the initialization stage, i.e., multiplying the sensed data x_i with a random coefficient $\varphi_{i,i}$ for all the sensor nodes.

The Second Situation

Any two rows φ_i and φ_j are linearly dependent.

As expressed in (3.8), φ_i and φ_j will be linearly dependent if and only if they are precisely the same, which happens when the following two events happen simultaneously. The first event is that node i and node j have exactly the same neighbors, which happens with probability $P_{2,1}$. As shown in Figure 3.4(a), the value of $P_{2,1}$ equals to the probability that all the neighbors of node i and node j are located at their intersection area S_2 with the Euclidian distance $d(i,j) \leq 2r_t$. Since the average area of S_2 is $\bar{S}_2 = \frac{\pi r_t^2}{4}$ (see Section A.1), $P_{2,1}$ is calculated by

$$P_{2,1} = \left(\frac{\pi r_t^2}{4} \right)^{N\pi r_t^2} \times \left(1 - \left(2\pi r_t^2 - \frac{\pi r_t^2}{4} \right) \right)^{N-N\pi r_t^2}. \quad (3.11)$$

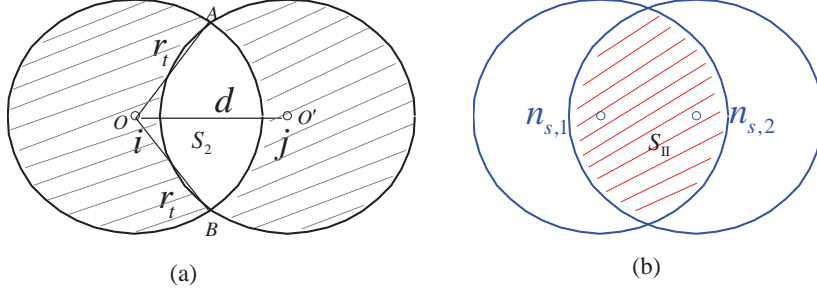


Figure 3.4: (a) Illustration of the area (represented by oblique lines) in which no nodes are located when calculating $P_{2,1}$, with $0 < d(i,j) \leq 2r_t$. (b) Illustration of the area S_{II} (represented by oblique lines) with $d(n_{s,1}, n_{s,2}) < r_t$, when calculating N_r^{II} in Section 3.4.3.

According to L' Hôpital's rule, as N approaches infinity, the limit of $P_{2,1}$ is

$$\lim_{N \rightarrow \infty} P_{2,1} = \lim_{N \rightarrow \infty} \left(\frac{\ln N}{4N} \right)^{\ln N} \times \left(1 - \frac{7 \ln N}{4N} \right)^{N - \ln N} = 0. \quad (3.12)$$

The second event is that exactly the same intermediate nodes are chosen to forward the received packet, which happens with probability $P_{2,2}$. Since $P_{2,2}$ is a function of P_0 and is much smaller than one, the limit of the probability that the second situation happens is

$$\lim_{N \rightarrow \infty} P_2 = \lim_{N \rightarrow \infty} P_{2,1} \times P_{2,2} = 0. \quad (3.13)$$

The Third Situation

Any three or more rows in Φ_t are linearly dependent. Similar to the second situation, the limit of the probability that the third situation happens is zero.

In conclusion, with a very high probability, the rows of the measurement matrix Φ are linearly independent and the sensor readings \mathbf{x} can be successfully recovered from $\mathbf{y} = \Phi \mathbf{x}$ with the proposed CNCDS scheme. \square

3.3.6 Discussion of CNCDS Scheme under More Practical Conditions

So far we have assumed that the sensor node can decode the received packets from several other transmit nodes in the same time slot. Now, let's consider a more practical situation where each sensor node can only decode one packet from another sensor node in one time slot. That is to say, packet collision will happen if one node receives several packets in the same time slot, and no packet can be decoded correctly in this situation. In addition, the situations of shadow fading and unreliable nodes are also considered for the CNCDS scheme.

The CNCDS Scheme Considering Packet Collisions

We propose to change the way of choosing source nodes in the CNCDS scheme to alleviate packet collisions. This is based on the observation that selecting proper nodes to broadcast messages can efficiently reduce packet collisions in WSNs [93]. Firstly, we geographically partition the entire network region into many disjoint and equally sized cellular zones. In each zone, the node that is the nearest to the center of the zone will be selected as a manager of the zone. Then, we randomly select the source nodes from the managers of the zones rather than from all of the sensor nodes.

When possible packet collisions happen during the intermediate node forwarding process, we assume that the corresponding nodes cannot decode the received packets and no retransmission will occur. This assumption is based on the fact that the failures in receptions for the colliding nodes do not reduce the rank of the measurement matrix, which decides the CS recovery performance. In addition, we will investigate the performance of the CNCDS scheme with packet collisions in Section 3.6 via simulations.

The CNCDS Scheme with Shadow Fading

In the disk radio model two nodes can communicate with each other if their distance is smaller than a constant r_t , because only path loss is considered. Now, we consider the effect of shadow fading on the performance of the CNCDS scheme. Assume that a node can decode the received packet if the received power exceeds a predefined threshold. Thus, when both path loss and log-normal shadowing are considered, the transmission range r_{sd} becomes a random variable

$$r_{sd} = r_t \times 10^{0.1 \times \vartheta_{dB} / \gamma}, \quad (3.14)$$

where ϑ_{dB} is a Gaussian-distributed random variable with zero mean and standard deviation σ_{dB} in dB, γ is the path loss exponent. In other words, the radio shape becomes irregular when considering shadow fading. The performance of the CNCDS scheme under shadow fading will be investigated in Section 3.6 via simulations.

The CNCDS Scheme with Unreliable Nodes

Since the CNCDS scheme is designed for hostile or catastrophic scenarios, we consider the impact of unreliable nodes on the CNCDS scheme in this section. Assume that the sensor nodes become not functional with a fixed probability p_{ur} . Then, the performance of the CNCDS scheme with unreliable nodes is evaluated in Section 3.6 via simulations.

3.4 Derivation of Expressions for Nt_{tot} and Nr_{tot}

To theoretically verify the efficiency of the proposed CNCDS scheme in reducing the total number of transmissions Nt_{tot} and receptions Nr_{tot} , we derive the expressions for Nt_{tot} and Nr_{tot} . In order to simplify the derivation, here we focus on the ideal CNCDS scheme, where we consider the disk radio model without packet collisions or unreliable nodes. Nt_{tot} and Nr_{tot} of the CNCDS scheme under more practical conditions will be

investigated via simulations in Section 3.6. In addition, the expressions for Nt_{tot} and Nr_{tot} also provide theoretical guidance on how to further improve the proposed CNCDS scheme.

3.4.1 Preliminary Knowledge

The network model in Section 3.2.2 indicates that the deployed WSN obeys the random geometric graph (RGG) [94] model $G(N, r_t)$, where N denotes the number of the nodes (vertices) which are randomly and uniformly distributed in a given area $S=1 \times 1$. If $d(i, j) \leq r_t$, then there exists an edge between node i and node j in $G(N, r_t)$. To avoid the edge effect, which means that the nodes close to the boundary of S will cover a smaller area than expected, the torus convention [95] is adopted in this chapter. Specifically, the torus convention turns the network area into a torus such that the region covered by any node is considered completely within the system. Thus, the link probability p_{link} , i.e., the probability of the occurrence of any link, is

$$p_{link} = \frac{\pi r_t^2}{S} = \pi r_t^2. \quad (3.15)$$

3.4.2 Lemma for Expressions for Nt_{tot} and Nr_{tot}

Lemma 3.1. *Consider a randomly and uniformly distributed WSN with N sensor nodes, which have identical transmission range r_t , where $r_t^2 > S \cdot \ln(N)/(\pi N)$ and $S=1 \times 1$ is the size of the field in which the WSN is deployed. The total number of transmissions Nt_{tot} and receptions Nr_{tot} during the data dissemination of the CNCDS scheme can be calculated respectively by*

$$Nt_{tot} = N_t^{II} + N_t^{III} = N_s + \sum_{q=1}^{N_f} N_t^q, \quad (3.16)$$

$$Nr_{tot} = N_r^{II} + N_r^{III} = N_r^{II} + \sum_{q=1}^{N_f} N_r^q, \quad (3.17)$$

where N_t^{II} and N_r^{III} (N_r^{II} and N_r^{III}) are the number of transmissions (receptions) in Stage II and Stage III respectively, N_t^q (N_r^q) is the number of transmissions (receptions) in the q^{th} forwarding of Stage III, N_f is the number of forwarding in Stage III. The relation between N_t^q and N_r^{q-1} is $N_t^q = P_0 \times N_r^{q-1}$, and specially we have $N_r^0 = N_r^{II}$.

Remark: In stage II, only the selected N_s source nodes transmit packets, thus we have $N_t^{II} = N_s$. In the CNCDS scheme, the reception nodes of the $(q-1)^{th}$ forwarding in Stage III will broadcast their received packets with probability P_0 in the q^{th} forwarding, therefore, we have $N_t^q = P_0 \times N_r^{q-1}$. The value of the total number of forwarding in Stage III is $N_f = q^* - 1$, where q^* is the value which makes $N_t^{q^*} = P_0 N_r^{q^*-1} < 1$. Consequently, we have $N_t^{III} = \sum_{q=1}^{N_f} N_t^q$ and $N_r^{III} = \sum_{q=1}^{N_f} N_r^q$.

3.4.3 Derivation of N_r^{II}

Proposition 3.1. *The number of receptions in Stage II of the CNCDS scheme is*

$$N_r^{II} = N_s \times N \pi r_t^2 - C_{N_s}^2 \pi r_t^2 \times N \left(\pi - \frac{3\sqrt{3}}{4} \right) r_t^2. \quad (3.18)$$

Proof. As shown in Table 3.1, the data dissemination process in Stage II indicates that N_r^{II} equals to the number of the neighbors of all the source nodes, $N_{s,nei}$, minus the number of the nodes which do not receive (combine) the heard packet because the condition (3.3) is not satisfied, $N_{nr,II}$, i.e.,

$$N_r^{II} = N_{s,nei} - N_{nr,II}. \quad (3.19)$$

The number of the neighbors of all the source nodes $N_{s,nei}$ is

$$N_{s,nei} = N_s \times N \times \pi r_t^2, \quad (3.20)$$

where $N \times \pi r_t^2$ denotes the average number of the neighbors of each node.

Based on the reception condition (3.3), the nodes in area S_{II} (as shown in Figure 3.4(b)) share the node ID of $n_{s,2}$ if node $n_{s,2}$ firstly broadcasts its packet to its neighbors.

So, $N_{nr,II}$ is the number of common neighbors of two separate source nodes $n_{s,1}$ and $n_{s,2}$ with $d(n_{s,1}, n_{s,2}) < r_t$, i.e.,

$$N_{nr,II} = N_{s,link} \times N \times \bar{S}_{II}, \quad (3.21)$$

where \bar{S}_{II} denotes the expected area jointly covered by two source nodes $n_{s,1}$ and $n_{s,2}$ with $d(n_{s,1}, n_{s,2}) < r_t$, $N_{s,link}$ is the number of source node pairs which satisfy $d(n_{s,1}, n_{s,2}) < r_t$, i.e., the number of links among the N_s source nodes,

$$N_{s,link} = C_{N_s}^2 \times p_{link} = C_{N_s}^2 \times \pi r_t^2. \quad (3.22)$$

As calculated in Section A.2, the value of \bar{S}_{II} is $\bar{S}_{II} = (\pi - \frac{3\sqrt{3}}{4})r_t^2$. Therefore, we have

$$N_{nr,II} = C_{N_s}^2 \times \pi r_t^2 \times N \times (\pi - \frac{3\sqrt{3}}{4})r_t^2. \quad (3.23)$$

Combining (3.19), (3.20) and (3.23), we obtain (3.18). \square

3.4.4 Derivation of N_r^q

Proposition 3.2. *In the CNCDS scheme, the number of receptions in the q^{th} forwarding of Stage III is expressed as*

$$\begin{aligned} N_r^q = & N_t^q \times N \frac{3\sqrt{3}}{4} r_t^2 - C_{N_t^q}^2 \frac{(14\pi - 15\sqrt{3})}{36} r_t^2 \times N \frac{\pi r_t^2}{6} \\ & - N_t^q \frac{(\pi - 3\sqrt{3}/4)r_t^2}{\pi r_t^2} \times N \frac{\pi r_t^2}{6} \\ & - N_t^q \frac{3\sqrt{3}r_t^2/16}{\pi r_t^2} \times N (\pi - \frac{15\sqrt{3}}{16}) r_t^2 \end{aligned} \quad (3.24)$$

Proof. The calculation of N_r^q is also based on the reception condition (3.3). As shown in Figure 3.5(a), the reception nodes in the q^{th} forwarding of Stage III are located in the area S_{III} , which is covered by the selected forward node n_t^q in the q^{th} forwarding but not covered by the node n_t^{q-1} which transmits packet to n_t^q . Let $N_{r,1}^q$ denote the number of the reception nodes in areas such as S_{III} .

Besides the above basic situation, there are two special cases which need to be considered:

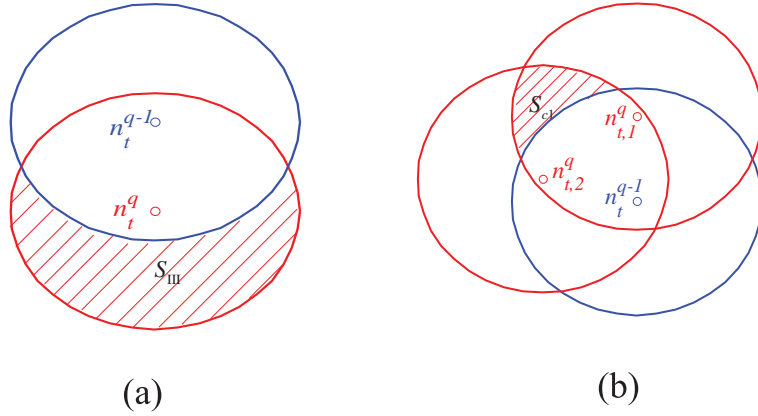


Figure 3.5: (a) Illustration of area S_{III} , (b) Illustration of area S_{c1} described in Case One.

Case One

As shown in Figure 3.5(b), two selected forward nodes $n_{t,1}^q$ and $n_{t,2}^q$ in the q^{th} forwarding are the receive nodes of the same forwarding node n_t^{q-1} in the $(q-1)^{th}$ forwarding. In such a case, the reception nodes in area S_{c1} (as shown in Figure 3.5(b)) will be counted twice. Suppose that the number of reception nodes in areas such as S_{c1} is $N_{r,2}^q$, which should be subtracted from $N_{r,1}^q$.

Case Two

Figure 3.6 illustrates the second case, where the selected forward node n_t^q in the q^{th} forwarding is located at the intersection of two forwarding nodes $n_{t,1}^{q-1}$ and $n_{t,2}^{q-1}$ in the $(q-1)^{th}$ forwarding. Due to the existence of $n_{t,2}^{q-1}$, the nodes in area S_{c2} (represented by the solid oblique lines in Figure 3.6) will not receive the heard packets in accordance with the reception condition (3.3). To facilitate the calculation of area S_{c2} , this case is further divided into two situations: (a) $0 < d(n_{t,1}^{q-1}, n_{t,2}^{q-1}) < r_t$ and (b) $r_t < d(n_{t,1}^{q-1}, n_{t,2}^{q-1}) < 2r_t$. Correspondingly, as shown in Figure 3.6(a) and Figure 3.6(b), the area of each situation is denoted by S_{c2a} and S_{c2b} respectively. Suppose that the numbers of the reception nodes in areas S_{c2a} and S_{c2b} are respectively denoted by $N_{r,3}^q$ and $N_{r,4}^q$. Again, $N_{r,3}^q$ and $N_{r,4}^q$

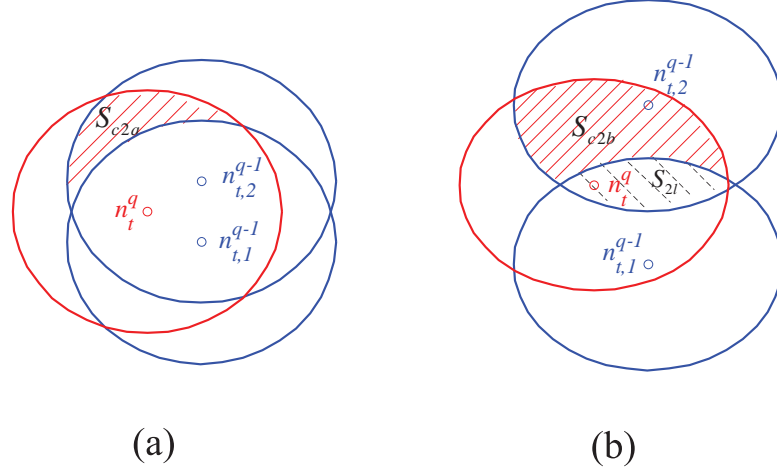


Figure 3.6: Illustration of area S_{c2} in Case Two, and S_{c2} is further divided into two situations: (a) S_{c2a} with $0 < d(n_{t,1}^{q-1}, n_{t,2}^{q-1}) < r_t$, (b) S_{c2b} with $r_t < d(n_{t,1}^{q-1}, n_{t,2}^{q-1}) < 2r_t$.

should also be subtracted from $N_{r,1}^q$.

In summary, the number of receptions in the q^{th} forwarding N_r^q can be expressed as

$$N_r^q = N_{r,1}^q - N_{r,2}^q - N_{r,3}^q - N_{r,4}^q. \quad (3.25)$$

The values of $N_{r,1}^q$, $N_{r,2}^q$, $N_{r,3}^q$ and $N_{r,4}^q$ are calculated in Appendix A.3. Combining (3.25), (A.12), (A.16), (A.19) and (A.23), we can obtain (3.24). \square

3.4.5 Formal Expressions for Nt_{tot} and Nr_{tot}

Theorem 3.2. Assume that all the N sensor nodes of a randomly and uniformly distributed WSN have identical transmission range r_t , where $r_t^2 > S \cdot \ln(N)/(\pi N)$ and $S = 1 \times 1$ is the size of the field in which the WSN is deployed. If the CNCDS scheme is used to fulfill the DDS function, then the total number of transmissions Nt_{tot} and receptions Nr_{tot} during the whole data dissemination are expressed respectively as

$$Nt_{tot} = N_s + \sum_{q=1}^{N_f} N_t^q, \quad (3.26)$$

$$\begin{aligned}
Nr_{tot} = & \left(N_s \times N\pi r_t^2 - C_{N_s}^2 \pi r_t^2 \times N\left(\pi - \frac{3\sqrt{3}}{4}\right)r_t^2 \right) \\
& + \sum_{q=1}^{N_f} \left(N_t^q N^{\frac{3\sqrt{3}}{4}} r_t^2 - C_{N_t^q}^2 \frac{(14\pi - 15\sqrt{3})}{36} r_t^2 N^{\frac{\pi r_t^2}{6}} \right) \\
& - \sum_{q=1}^{N_f} \left(N_t^q \frac{(\pi - 3\sqrt{3}/4)r_t^2}{\pi r_t^2} \times N^{\frac{\pi r_t^2}{6}} \right) \\
& - \sum_{q=1}^{N_f} \left(N_t^q \frac{3\sqrt{3}r_t^2/16}{\pi r_t^2} \times N\left(\pi - \frac{15\sqrt{3}}{16}\right)r_t^2 \right)
\end{aligned} \tag{3.27}$$

where $N_t^q = P_0 \times N_r^{q-1}$, $N_r^0 = N_r^H$, the expression for N_r^q is shown in (3.23), and $N_f = q^* - 1$ where q^* is the value which makes $N_t^{q^*} = P_0 N_r^{q^*-1} < 1$ as defined in the remark in Lemma 3.1.

Proof. Obviously, (3.26) can be directly obtained from (3.16). Based on (3.17) in Lemma 3.1, (3.18) in Proposition 3.1 and (3.24) in Proposition 3.2, we have the expression (3.27). \square

3.5 The Adaptive CNCDS Scheme

Based on the expressions for Nt_{tot} and Nr_{tot} , we propose an adaptive CNCDS scheme.

3.5.1 Motivation of Adaptive CNCDS Scheme

The forwarding probability P_0 is a very important parameter in the design of the CNCDS scheme. From the relation $N_t^q = P_0 \times N_r^{q-1}$ and the derived expressions for Nt_{tot} and Nr_{tot} in (3.26) and (3.27), we can conclude that Nt_{tot} and Nr_{tot} increase with the increasing P_0 . Therefore, one way to further reduce Nt_{tot} and Nr_{tot} is to reduce the forwarding probability. However, to ensure sufficient delivery of the information packets, the value of P_0 should be bigger than a well-chosen probability P_0^* [75], which equals to the probability that a giant component appears in the random network [96]. A giant component in a random graph is defined as a connected component which contains a positive fraction of the entire graph's vertices.

Nevertheless, the uniform forwarding probability P_0 is not optimal for a randomly distributed WSN. The reason is that the ability to disseminate a message varies from node to node in a random WSN since each node has a different number of neighbors. Thus, if we want to achieve an average efficiency in delivering a message, the nodes which have a larger number of neighbors can adopt a smaller forwarding probability. On the contrary, the nodes which have a smaller number of neighbors can adopt a bigger forwarding probability. Motivated by this observation, we propose the following adaptive CNCDS scheme based on the expressions for Nt_{tot} and Nr_{tot} .

3.5.2 Description of Adaptive CNCDS Scheme

Here, we assume that a node n_k can acquire the knowledge of the number of its neighbors $N_{nei,k}$. For example, $N_{nei,k}$ can be obtained by letting node n_k send a reference signal to its neighbors, and then the nodes receiving the reference signal respond with a feedback to n_k . Thus, we have $N_{nei,k}$ equal to the number of the feedbacks n_k received. In the adaptive CNCDS scheme, the adaptive forwarding probability $P_{adp,k}$ of node n_k is set to be inversely proportional to the number of its neighbors $N_{nei,k}$, i.e.,

$$P_{adp,k} = \frac{P_0^*}{N_{nei,k}}, \quad k=1, \dots, N. \quad (3.28)$$

The procedures of the adaptive CNCDS scheme are very similar to those of the CNCDS scheme which are described in Table 3.1. The only difference is that, in the adaptive CNCDS scheme the reception nodes in Stage II and Stage III broadcast their received packets with an adaptive forwarding probability $P_{adp,k} = P_0^*/N_{nei,k}$, while in the CNCDS scheme the reception nodes broadcast their received and merged packets with a uniform probability $P_0 = P_0^*$.

3.5.3 Extended Research on Energy Efficiency of Wireless Network

The above proposed schemes are designed to improve the energy efficiency of WSNs, however, the energy efficiency of cellular network has also attracted a lot of attentions. Thus, we also investigate the energy efficiency of cellular network based on relay technology. Specifically, we consider three basic bidirectional relay transmission schemes (i.e., the 4 time-slot (4TS), 3 time-slot (3TS) and 2 time-slot (2TS) scheme) from the angle of relay deployment. Since a realistic power consumption model is very important in analyzing energy efficiency, and power amplifier (PA) consumes up to 70% of the total power, we consider a realistic non-ideal PA model.

The derived closed-form expressions for the optimal relay deployment and the simulation results reveal the following two important conclusions. First, in bad channel conditions (heavy path loss), the RN should be deployed much farther from the BS than that under good channel conditions (small path loss). In other words, in bad channel conditions, it is possible to improve the energy efficiency while enlarging the cell coverage. However, it will be challenging to extend the cell coverage and enhance the energy efficiency simultaneously under good channel conditions. Second, the relay node should be deployed nearer to base station with the non-ideal PA than that with the ideal PA, and the optimal energy efficiency with non-ideal PA is much higher than that with ideal PA.

Further details can be found in one of my papers, which is published in *IEEE Transactions on Vehicular Technology*, 2013.

3.6 Performance Evaluation

3.6.1 Simulation Parameters and Performance Metrics

Monte Carlo simulations are performed with MATLAB to evaluate the performance of the proposed schemes against the existing schemes, and each simulation is repeated 3000 times. Firstly, $N = 1000$ nodes are randomly deployed in a normalized $S = 1 \times 1$ area, i.e., the coordinates (X_i, Y_i) of node i for $i = 1, \dots, N$ are two-dimensional standard uniformly distributed variables. Secondly, we assume that the sensor reading vector \mathbf{x} is compressible on the DCT basis and its coefficients satisfy (3.1) with $p = 7/8$. Then, the proposed CNCDS scheme is simulated according to the pseudocode in Table 3.1, where the forwarding probability is set to $P_0 = 0.24$ according to [15], the number of nodes queried by the mobile collector M ranges from 70 to 150 to observe the variance of the performance, and the probability that each node selects itself as a source node P_1 ranges from 0.09 to 0.18 corresponding to the values of M from 70 to 150.

The simulation parameters for more practical scenarios are stated as follows: the standard deviation σ_{dB} of the log-normal shadow fading is $\sigma_{dB} = 2\text{dB}$, the path loss exponent is $\gamma = 2.2$, and the probability that the sensor node becomes not functional is $p_{ur} = 0.15$. Finally, to evaluate the energy efficiency and the recovery performance of the proposed schemes, we choose the following three performance metrics: the total number of transmissions Nt_{tot} , the total number of receptions Nr_{tot} and the recovery Mean Squared Error (MSE) between the CS recovered sensor readings $\hat{\mathbf{x}}$ and the original sensor readings \mathbf{x} .

3.6.2 Schemes Used for Comparison

To verify the efficiency of the proposed CNCDS and adaptive CNCDS schemes, we compare them with the Improved CStorage (ICStorage) scheme and NoInitCNCDS scheme.

The ICStorage scheme is an improved version of the CStorage scheme [75], which is a very efficient DDS scheme employing CS theory. However, the CStorage scheme still has an extremely high number of transmissions, e.g., 1.545×10^6 for 10^4 sensor nodes [75]. Hence, to make the comparisons more comparable, we compare our proposed schemes with the ICStorage scheme, where we improve the CStorage scheme by letting the intermediate nodes forward their own sensor readings rather than just the received source sensor readings as in [75]. The NoInitCNCDS scheme is the CNCDS scheme without the initialization stage, which means that the sensor readings are not multiplied with the random coefficient $\varphi_{i,i}$ before they are broadcasted. Here, the NoInitCNCDS scheme is used to illustrate the importance of the initialization stage of the CNCDS scheme.

3.6.3 Simulation Results

The Recovery MSE

Figure 3.7 shows the recovery MSE of the proposed CNCDS scheme and the adaptive CNCDS scheme in comparison with the ICStorage scheme and NoInitCNCDS scheme. Firstly, the CNCDS and adaptive CNCDS schemes outperform the ICStorage scheme and the NoInitCNCDS scheme. Specifically, the CNCDS and the adaptive CNCDS scheme reduce the CS recovery MSE by up to 76% compared with the ICStorage scheme. On the other hand, the NoInitCNCDS scheme increases the recovery MSE by up to 5.6 times compared with ICStorage scheme.

These different recovery performances are caused by the differences in the rank or incoherence of their measurement matrices. Compared with the ICStorage scheme, the CNCDS scheme decreases the recovery MSE by using a more strict reception condition (3.3), which can increase the incoherence of the measurement matrix. However, the NoInitCNCDS scheme increases the recovery MSE due to the linear dependency in the rows of its measurement matrix, which can be inferred from (3.9) and (3.10) in the proof

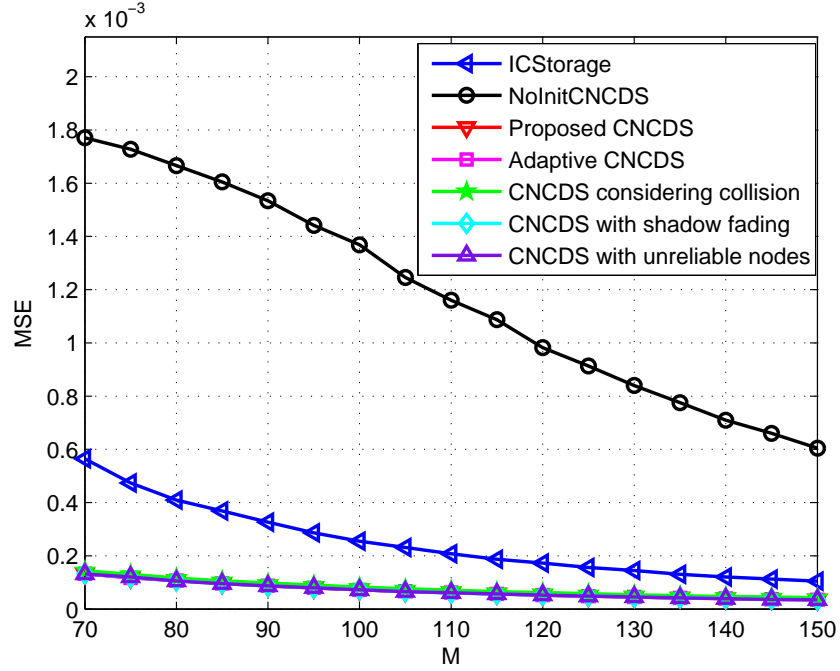


Figure 3.7: The recovery MSE vs. the number of nodes queried by the mobile collector M .

of Theorem 3.1. The adaptive CNCDS scheme has the same recovery MSE as the CNCDS scheme since the adaptive forwarding probability does not change the rank of the measurement matrix.

It is worthwhile to note that the CNCDS scheme considering packet collisions, shadow fading and unreliable nodes has almost the same recovery performance as the ideal CNCDS scheme. The reason is that the smaller transmission range due to shadow shading, the failures in receptions resulting from packet collisions, and unreliable nodes do not decrease the rank of the measurement matrix Φ . Specifically, based on the formulation process of the measurement matrix and the proof of Theorem 3.1, no additional elements are added to the measurement matrix Φ to make the rows of Φ linearly dependent.

Total Number of Receptions Nr_{tot}

Comparing Figure 3.8 with Figure 3.9, we find that the total number of receptions Nr_{tot} is much larger than the total number of transmissions Nt_{tot} . Since the data reception has almost the same energy cost as data transmission in WSNs, it is very important to reduce the number of receptions to improve the energy efficiency. The simulation results in Figure 3.8 show that, the NoInitCNCDS scheme, the CNCDS scheme and the adaptive CNCDS scheme reduce Nr_{tot} by up to 72%, 74% and 82% respectively in comparison with the ICStorage scheme. The decrease of Nr_{tot} for the NoInitCNCDS scheme and the CNCDS scheme results from the reception condition (3.3). Compared with CNCDS scheme, the adaptive CNCDS scheme reduced Nr_{tot} by up to 32% due to the adaptive forwarding probability.

The CNCDS scheme considering packet collisions has smaller Nr_{tot} than the ideal CNCDS scheme. This is because we only count the successful receptions in the CNCDS scheme with packet collisions, whereas the actual number of receptions including the failed ones is the same as the ideal CNCDS scheme. The CNCDS scheme with shadowing fading and unreliable nodes also has smaller Nr_{tot} than the ideal CNCDS scheme due to the smaller transmission range and the failures in receptions of the unreliable nodes respectively.

Total Number of Transmissions Nt_{tot}

Figure 3.8 shows that the adaptive CNCDS scheme requires the smallest number of transmissions, whereas the ICStorage scheme requires the largest number of transmissions. Specifically, the NoInitCNCDS scheme, the CNCDS scheme and the adaptive CNCDS scheme decrease Nt_{tot} by up to 53%, 55% and 84% respectively in comparison with the ICStorage scheme. These sharp decreases in Nt_{tot} of the CNCDS scheme and the NoInitCNCDS scheme are due to the application of network coding and the reception condition

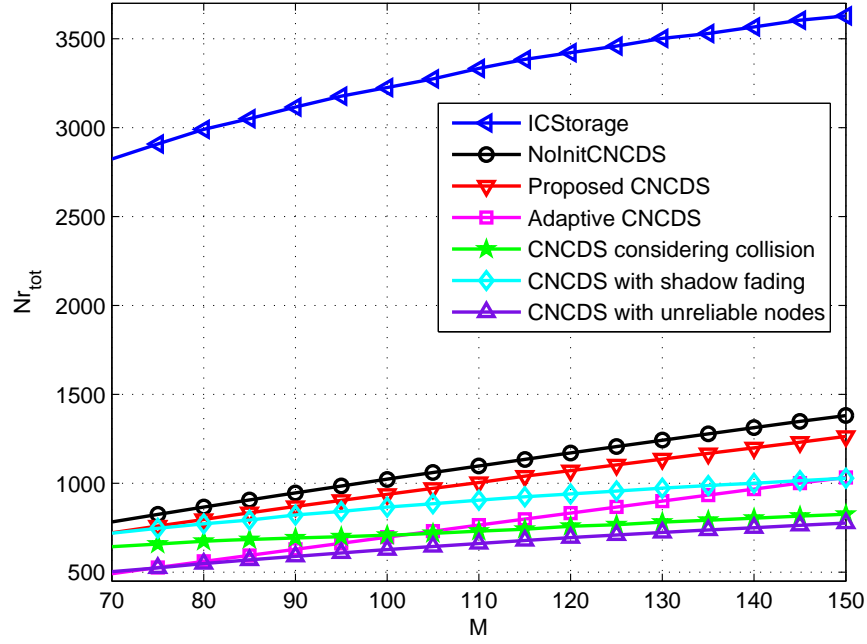


Figure 3.8: The total number of receptions Nr_{tot} vs. the number of nodes queried by the mobile collector M .

(3.3). Due to the initialization stage of the CNCDS scheme, the CNCDS scheme needs fewer transmissions than the NoInitCNCDS scheme. Compared with the CNCDS scheme, the adaptive CNCDS scheme further reduces Nt_{tot} by up to 63% because of the adaptive forwarding probability. The CNCDS scheme considering packet collisions, fading channel and unreliable nodes has smaller Nt_{tot} than the ideal CNCDS scheme because of the smaller Nr_{tot} and the probabilistic broadcasting mechanism.

Cost of the Proposed CNCDS Scheme

In this section, we analyze the cost of the CNCDS scheme in terms of its overhead. As stated in Section 3.6.1 with $N = 1000$, the packet of each node i contains a set of 1-bit coefficients $\mathbf{r}(i).\mathbf{a1}$, a set of 10-bit node IDs $\mathbf{r}(i).\mathbf{a2}$ and the RLNC coded 64-bit data $\mathbf{r}(i).\mathbf{a3}$. Simulation results show that the mean cardinality of $\mathbf{r}(i).\mathbf{a1}$ or $\mathbf{r}(i).\mathbf{a2}$ for

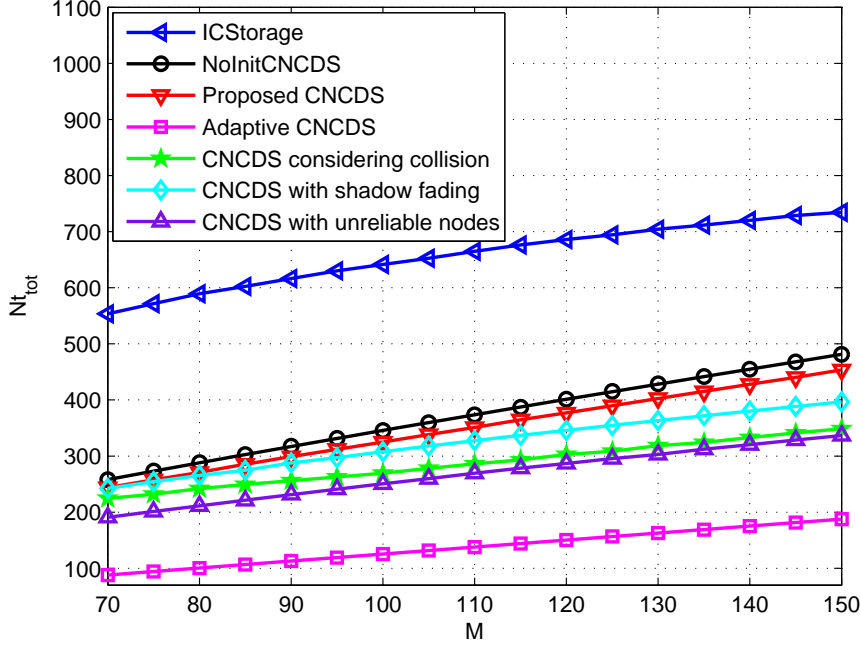


Figure 3.9: The total number of transmissions Nt_{tot} vs. the number of nodes queried by the mobile collector M .

$i = 1, \dots, N$ is 2.5 with variance 2.3, where the cardinality is defined as the number of elements in a set. In other words, most of the nodes' packets contain one 1-bit coefficient set $\mathbf{r}(i).\mathbf{a1}$ and one 10-bit node ID set $\mathbf{r}(i).\mathbf{a2}$ with cardinality ranging from 1 to 6. The average overhead is $2.5 \times 1 + 2.5 \times 10 = 27.5$ bits for each RLNC coded 64-bit data, which carries $64 \times 2.5 = 160$ bits of data on average. Thus, considering the equivalent transmission ability, the overhead of the proposed CNCDS scheme is low.

In summary, with the same CS recovery performance as that of the CNCDS scheme, the adaptive CNCDS scheme is capable of further reducing Nt_{tot} and Nr_{tot} by up to 63% and 32% respectively. Compared with ICStorage, both CNCDS and the adaptive CNCDS can simultaneously reduce Nt_{tot} , Nr_{tot} and the CS recovery MSE. In addition, when considering packet collisions, fading channel and unreliable nodes, the CNCDS scheme is robust and can guarantee the CS recovery performance due to the sparse property

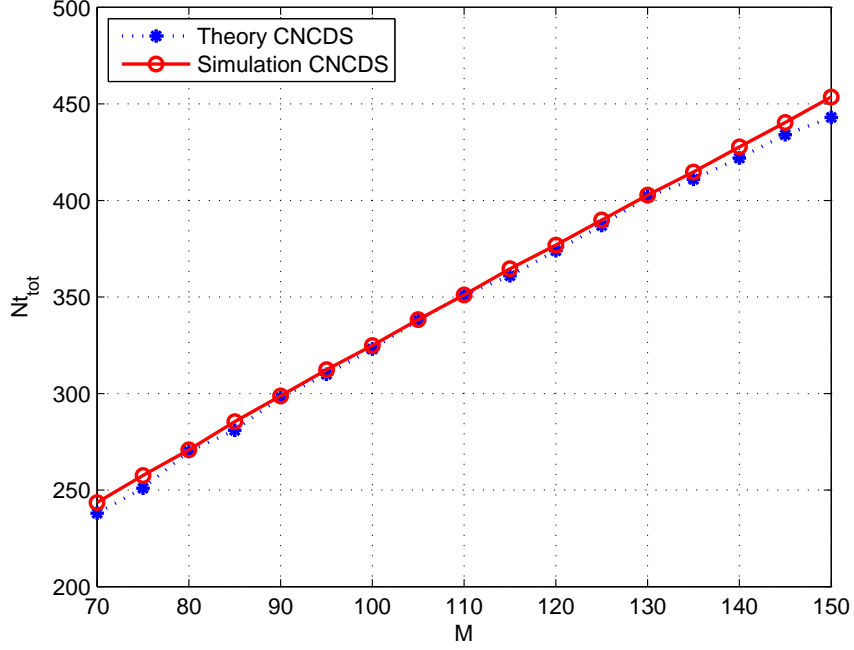


Figure 3.10: Comparison between the theoretical values and simulation results of the total number of transmissions Nt_{tot} vs. the number of nodes queried by the mobile collector M .

of the measurement matrix. Furthermore, the overhead of CNCDS is low in consideration of its equivalent transmission ability.

Comparisons between Theoretical Analysis and Simulation Results

Figure 3.10 and Figure 3.11 compare the theoretical values of Nt_{tot} and Nr_{tot} of the proposed CNCDS scheme with its simulation results. Firstly, it can be concluded that the theoretical analysis results coincide with the simulation results, which validates the efficiency of the CNCDS scheme and the correctness of the expressions for Nt_{tot} and Nr_{tot} in (3.26) and (3.27). The small difference between the theoretical values and the simulation results is caused by the approximations of \bar{S}_{c1} and \bar{S}_{c2a} in the theoretical analysis. Specifically, since the closed-form expressions for \bar{S}_{c1} and \bar{S}_{c2a} are too complicated to obtain, the average values are approximated by the corresponding maximum values.

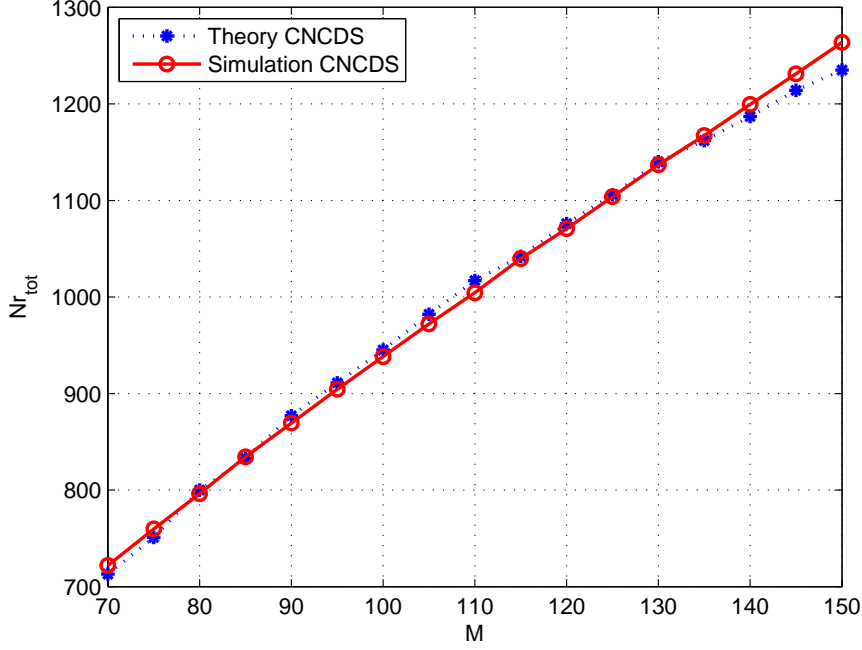


Figure 3.11: Comparison between the theoretical values and simulation results of the total number of receptions Nr_{tot} vs. the number of nodes queried by the mobile collector M .

3.7 Summary

Exploiting the correlation of the sensor readings in WSNs, this chapter proposes the CNCDS scheme based on the compressed sensing theory and network coding technology. The proposed CNCDS scheme achieves high energy efficiency by reducing the total number of transmissions Nt_{tot} and receptions Nr_{tot} respectively. Theoretical analysis proves that the CNCDS scheme guarantees good recovery performance. Based on the random graph theory, we derive the expression for Nt_{tot} and Nr_{tot} to verify the correctness and efficiency of the CNCDS scheme. Furthermore, based on the expressions for Nt_{tot} and Nr_{tot} , an adaptive CNCDS scheme is proposed. Simulation results show that, the proposed CNCDS scheme reduces Nt_{tot} , Nr_{tot} and the CS recovery MSE by up to 55%, 74% and 76% respectively in comparison with the conventional ICStorage scheme. In addition, the

adaptive CNCDS scheme can further reduce Nt_{tot} and Nr_{tot} by up to 63% and 32% respectively compared with the CNCDS scheme.

After the study on applications of discrete CS in WSNs in this chapter, we will investigate the extension of discrete CS into the analog domain in the next chapter.

Chapter 4

Structured Measurement Matrix Based Analog Compressed Sensing

As described in Chapter 3, discrete CS is able to resolve some challenges faced by wireless communications. Meanwhile, as one motivation behind CS is to realize the sub-Nyquist sampling of analog signals, CS has been extended to the analog domain, i.e., analog CS. The objective of this chapter is to improve the recovery performance and decrease the hardware complexity of analog CS based on a structured matrix.

4.1 Introduction

At the early stage of CS, most of the related work restricted their attentions to discrete signals due to the simplicity in theoretical analysis and providing performance guarantees [9]. Motivated by the desire to acquire extremely wideband analog signals at the sub-Nyquist sampling rate, CS has been pushed forward to the analog domain. The first challenge faced by analog CS is to find a suitable basis for the analog sparse signal. Another challenge is that the random measurement matrix is not easy to implement with hardware. However, if we can use a structured matrix to replace the random one, then

we can simplify the hardware implementation of analog CS. Thus, in this chapter, we will investigate analog CS from the angles of sparse signal representation and hardware implementation of the measurement matrix.

Most of existing research on analog CS is based on the DFT basis. Most recently, M.A. Davenport et al investigated analog CS in [97] using Discrete Prolate Spheroidal Sequences (DPSSs) [98], which is also termed as the Slepian basis. One of the important conclusions in [97] is that AIC can also be used to capture the multiband signal under the Slepian basis, while [66] states that AIC can only be used to sample the multi-tone signals under the DFT basis. In addition, the Slepian basis can substantially improve the recovery performance of analog CS compared with the DFT basis. However, modulating and merging the Slepian basis [97] produces a large-scale dictionary and a corresponding large-scale measurement matrix, which results in a very high computational load in the recovery stage. Thus, one objective of this chapter is to reduce the recovery computational complexity while improving the recovery performance.

As stated in Section 2.2.2, the low computation load and simple hardware structure make MWC a very attractive analog CS technique. However, when the multi-band signal is not very sparse, MWC still requires a large number of parallel channels, with each channel consisting of a mixing function $p_i(t)$, a LPF and an ADC. Two methods have been proposed to reduce the number of parallel channels. One is the collapsing method [2] proposed for MWC, the other is the segmented technique [67] proposed for the parallel structure of AIC [9]. Unfortunately, both of these two methods reduce the hardware complexity at the cost of a much higher sampling rate at each channel and increased digital processing. Therefore, the second objective of this chapter is to reduce the hardware complexity of MWC without increasing the sampling rate at each channel.

The main contributions of this chapter are stated as follows:

- (1) To reduce the computational complexity, rather than using the modulated Slepian-

an basis to represent the whole original multiband signal, this chapter proposes to use the non-modulated Slepian basis to represent the modulated and band-limited multiband signal. Based on the analytical derivation under the non-modulated Slepian basis, we conclude that the direct recovery (DR) algorithm based on Moore-Penrose pseudo-inverse cannot benefit from the Slepian basis. Thus, an interpolation recovery (IR) algorithm is further proposed to take full advantage of the Slepian basis by interpolating the CS recovered low-rate sequence into the Nyquist rate with the Slepian function. Simulation results demonstrate that, the non-modulated Slepian basis combined with the IR algorithm improves the recovery SNR by up to 35dB with a low recovery computational load.

(2) To reduce the hardware complexity without increasing the sampling rate of each channel, this chapter proposes the Random Circulant Orthogonal Matrix based Analog Compressed Sensing (RCOM-ACS) scheme, which reduces the number of physical parallel channels from m to 1. By replacing the independent mixing functions with random cyclic shifts of the Zadoff-Chu sequence, the RCOM-ACS scheme reuses the LPF and ADC, which have the same parameters at different channels of MWC. Theoretical analysis proves that the measurement matrix of the RCOM-ACS scheme satisfies the RIP condition, which is a standard tool for studying the effectiveness of the measurement matrix in CS. Simulation results show that the RCOM-ACS scheme has the best recovery performance compared with MWC and the collapsing method.

This chapter is organized as follows. Section 4.2 presents the analog CS method based on the non-modulated Slepian basis. Section 4.3 describes the proposed RCOM-ACS scheme. Finally, Section 4.4 concludes this chapter.

4.2 Non-Modulated Slepian Basis Based Analog Compressed Sensing

This section is organized as follows. Section 4.2.1 briefly introduces the CS theory and the Slepian basis. Section 4.2.2 presents the analytical derivation with the non-modulated Slepian basis. Section 4.2.3 investigates the recovery algorithm. Section 4.2.4 evaluates the recovery performance.

4.2.1 Brief Introduction to Slepian Basis

This section briefly introduces the Slepian basis, which includes both the Prolate Spheroidal Wave Functions (PSWFs) and DPSSs.

PSWFs

PSWF [99] answers the question of how nearly time-limited a band-limited signal can be. Given any time interval $T > 0$ and any bandwidth $B > 0$, the PSWFs are the real functions $\psi_0(t), \psi_1(t), \psi_2(t), \dots$ with the following properties:

- i. For all values of t , $\psi_i(t)$ is the real solution to

$$\lambda_i \psi_i(t) = \int_0^T \frac{\sin 2\pi B(t-s)}{\pi(t-s)} \psi_i(s) ds, \quad i = 0, 1, 2, \dots, \quad (4.1)$$

with λ_i being the ordered real positive eigenvalues of (4.1), i.e., $\lambda_0 > \lambda_1 > \dots$. The first $2TB$ eigenvalues are extremely close to one, while the others fall off to zero rapidly. The parameter $2TB$ is termed as the time bandwidth product.

- ii. In the real line, $\psi_i(t)$ is band-limited in $\mathcal{F}_B = [-B, B]$ and orthonormal, i.e.,

$$\int_{-\infty}^{\infty} \psi_i(t) \psi_j(t) dt = \begin{cases} 0, & i \neq j \\ 1, & i = j \end{cases} \quad i, j = 0, 1, 2, \dots. \quad (4.2)$$

iii. In the time interval $0 \leq t \leq T$, the $\psi_i(t)$ are orthogonal, i.e.,

$$\int_0^T \psi_i(t) \psi_j(t) dt = \begin{cases} 0, & i \neq j \\ \lambda_i, & i = j \end{cases} \quad i, j = 0, 1, 2, \dots \quad (4.3)$$

From the above property ii and property iii, we can conclude that the PSWFs are doubly orthogonal and form the Slepian basis. Thus, a band-limited signal $f(t)$ can be approximated by

$$f(t) = \sum_{j=0}^{J-1} \beta_j \psi_j(t), \quad (4.4)$$

with $\beta_j = \frac{1}{\lambda_j} \int_0^T f(t) \psi_j(t) dt$ and $J \geq 2TB$.

DPSSs

DPSS [98] is the discrete case of PSWF. For each $k=0,1,\dots,N-1$, DPSSs are the real solutions of

$$\sum_{n'=0}^{N-1} \frac{\sin 2\pi W(n-n')}{\pi(n-n')} v_k[n'] = \lambda_k v_k[n], \quad (4.5)$$

for $n = 0, \pm 1, \pm 2, \dots$, where $0 < W < 1/2$ is the normalized bandwidth. The DPSSs are normalized so that

$$\sum_{j=0}^{N-1} v_k^2[j] = 1. \quad (4.6)$$

Similar to PSWFs, the DPSSs are doubly orthogonal:

$$\sum_{n=0}^{N-1} v_i[n] v_j[n] = \lambda_i \sum_{n=-\infty}^{\infty} v_i[n] v_j[n] = \delta_{ij}, \quad (4.7)$$

for $i, j = 0, 1, \dots, N-1$.

Then, using the Slepian basis in the discrete form, a band-limited sequence h_n for $n = 0, 1, 2, \dots$ can be approximated as

$$h_n = \sum_{j=0}^{J-1} \gamma_j v_j[n], \quad (4.8)$$

with $\gamma_j = \sum_{n=0}^{N-1} h_n v_j[n]$ and $J \geq 2NW$.

4.2.2 Analytical Derivation of MWC under Slepian Basis

This section analyzes the MWC with the non-modulated Slepian basis and derives its system expression in matrix form.

Signal Model and System Description

Let $x(t)$ be a continuous-time signal which is band-limited to $\mathcal{F} = [-f_{nyq}/2, f_{nyq}/2]$, where f_{nyq} is the Nyquist sampling rate of $x(t)$. In the observation time $[0, T]$, $x(t)$ is multiband if its Fourier transform $X(f)$ contains a union of K disjoint bands in \mathcal{F} , where the bandwidth of each band does not exceed $2B$.

As described in Section 2.2.2, the expression for the mixing function can be described as

$$p_i(t) = \sum_{l=-L_0}^{L_0} a_{il} e^{j2\pi \frac{l}{T_p} t}, \quad (4.9)$$

with a_{il} is calculated by (2.37) and $L_0 = \lceil (f_{nyq} + f_s)/2f_p \rceil - 1$ and $L=2L_0+1$. The necessary condition for successful recovery is $f_s \geq f_p$, $M \geq L$ and $m \geq 2K$, and the simplest choice is $M=L$ and $f_s=f_p \simeq 2B$ [2], which are also the settings in this chapter.

Derivation with Non-modulated Slepian Basis

From Figure 2.3, it can be concluded that $y_i(t)$ is actually a time-limited and band-limited version of $\tilde{x}_i(t)$. Define the time-limit operator as

$$\mathcal{D}\{x(t)\} = \begin{cases} x(t), & 0 \leq t \leq T \\ 0, & \text{others} \end{cases}, \quad (4.10)$$

and the band-limit operator is

$$\mathcal{B}\{x(t)\} = \int_{-f_s/2}^{f_s/2} X(f) e^{j2\pi f t} df. \quad (4.11)$$

Thus, $y_i(t)$ can be expressed as

$$y_i(t) = \mathcal{BD}\{\tilde{x}_i(t)\} = \mathcal{BD}\{x(t)p_i(t)\}. \quad (4.12)$$

Based on the Fourier expansion and approximation of $p_i(t)$ in (4.9), we rewrite (4.12) as

$$\begin{aligned} y_i(t) &= \sum_{l=-L_0}^{L_0} a_{il} \cdot \mathcal{BD}\{x(t)e^{j2\pi l f_p t}\} \\ &= \sum_{l=-L_0}^{L_0} a_{il} \int_0^T x(s) e^{j2\pi l f_p s} \int_{-f_s/2}^{f_s/2} e^{j2\pi f(t-s)} df ds \quad (4.13) \\ &= \sum_{l=-L_0}^{L_0} a_{il} \int_0^T \frac{\sin \pi f_s(t-s)}{\pi(t-s)} x(s) e^{j2\pi l f_p s} ds \end{aligned}$$

Then, based on (4.1), the band-limited $y_i(t)$ can be expressed by as

$$y_i(t) = \sum_{l=-L_0}^{L_0} a_{il} \sum_{j=0}^{J-1} c_{lj} \psi_j(t), \quad (4.14)$$

with $J \geq 2TB = 2N_s T_s f_s / 2 = N_s$, and the coefficient c_{lj} is

$$c_{lj} = \frac{1}{\lambda_j} \int_0^T x(t) e^{j2\pi l f_p t} \psi_j(t) dt. \quad (4.15)$$

Therefore, the expression of the sampled sequence $y_i[n]$ is

$$y_i[n] = y_i[nT_s] = \sum_{l=-L_0}^{L_0} \sum_{j=0}^{J-1} a_{il} c_{lj} \psi_j[nT_s]. \quad (4.16)$$

The matrix expression of the output $y_i[n]$ for $n=1, \dots, N_s$ and $i=1, \dots, m$ is

$$\mathbf{Y} = \mathbf{A} \mathbf{C} \mathbf{\Psi}, \quad (4.17)$$

where \mathbf{Y} is a $m \times N_s$ matrix with $y_{in} = y_i[nT_s]$, \mathbf{A} is a $m \times L$ with elements a_{il} , \mathbf{C} is a $L \times J$ matrix with elements c_{lj} , and $\mathbf{\Psi}$ is a $J \times N_s$ non-modulated Slepian basis, whose element in the j^{th} row and n^{th} column is $\psi_{jn} = \psi_j[nT_s]$.

4.2.3 Recovery Algorithm

This section investigates how to reconstruct $x(t)$ from the measurements $y_i[n]$ with $n=1, \dots, N$ and $i=1, \dots, m$.

Problem Formulation

Since $f_s=f_p$, $x(t)$ in the observation time interval $[0, T]$ can be expressed as

$$\begin{aligned} x(t) &= \sum_{l=-L_0}^{L_0} e^{-j2\pi l f_p t} \cdot \mathcal{BD}\{x(t)e^{j2\pi l f_p t}\} \\ &= \sum_{l=-L_0}^{L_0} e^{-j2\pi l f_p t} \cdot \sum_{j=0}^{J-1} c_{lj} \psi_j(t) \end{aligned} \quad (4.18)$$

The digital sequence $x[nT_{nyq}]$ at the Nyquist rate is

$$x[nT_{nyq}] = \sum_{l=-L_0}^{L_0} e^{-j2\pi l f_p n T_{nyq}} \cdot \sum_{j=0}^{J-1} c_{lj} \psi_j[nT_{nyq}], n = 0, 1, \dots, N_{nyq}. \quad (4.19)$$

Then, the matrix form of the above equation (4.19) is

$$\mathbf{x} = \text{diag}(\mathbf{E}\mathbf{C}\mathbf{V}), \quad (4.20)$$

where function $\text{diag}(\cdot)$ returns the main diagonal of the input matrix, \mathbf{x} is the $N_{nyq} \times 1$ vector with $x_n = x[nT_{nyq}]$, matrix \mathbf{E} is a $N_{nyq} \times L$ with elements $e^{-j2\pi l n f_p / f_{nyq}}$, matrix \mathbf{C} is a $L \times J$ matrix which is the same as that defined in (4.17), and matrix \mathbf{V} is a $J \times N_{nyq}$ matrix with $v_{jn} = \psi_j[nT_{nyq}]$.

DR Algorithm

1) *Algorithm Description:* Since $x(t)$ is a multiband signal and is K -block-sparse in \mathcal{F} , it can be concluded from (4.14) that only $O(K)$ rows of the $L \times N_s$ matrix $\mathbf{C}\Psi$ are non-zero or have large amplitudes. Thus, problem (4.17) satisfies the MMV [100] model and the M-OMP algorithm [100] can be used to recover the positions of the non-zeros rows (support S) of $\mathbf{C}\Psi$.

Once we get the support S , the estimation of the signal at the non-zero rows is $\hat{\mathbf{X}}_s = \mathbf{A}_s^+ \mathbf{Y}$, where \mathbf{A}_s contains the columns of \mathbf{A} indexed by S , and \mathbf{A}_s^+ is the Moore-Penrose pseudo-inverse of \mathbf{A}_s . Then, the estimate of the coefficient matrix \mathbf{C} at the non-zero rows is $\hat{\mathbf{C}}_s = \mathbf{A}_s^+ \mathbf{Y} \Psi^+$. According to (4.20), the estimation of the digital sequence \mathbf{x}

with DR algorithm is

$$\hat{\mathbf{x}} = \text{diag}(\mathbf{E}_s \hat{\mathbf{C}}_s \mathbf{V}) = \text{diag}(\mathbf{E}_s \mathbf{A}_s^+ \mathbf{Y} \Psi^+ \mathbf{V}), \quad (4.21)$$

where \mathbf{E}_s contains the rows of \mathbf{E} indexed by support S .

2) *Performance Analysis:* According to the analysis in [97], to acquire the extremely good recovery performance, the number J of the DPSS vectors in the $J \times N_s$ Slepian basis Ψ should be larger than $2TB$. That is to say, to gain any benefit from the Slepian basis, $J > 2TB = N_s$ should be chosen. However, since the estimation of \mathbf{x} in the DR algorithm is based on the calculation of Ψ^+ , for which, if $J > N_s$, Ψ is not a full row rank matrix anymore and $\Psi \Psi^+ \neq \mathbf{I}$. Then, the estimation

$$\hat{\mathbf{C}}_s = \mathbf{A}_s^+ \mathbf{Y} \Psi^+ = \mathbf{A}_s^+ \mathbf{A} \mathbf{C} \Psi \Psi^+ = \mathbf{C}_s \Psi \Psi^+ \neq \mathbf{C}_s \quad (4.22)$$

will lead to a large deviation. Furthermore, according to (3.26) and the matrix theory, the estimation error of $\hat{\mathbf{x}} = \text{diag}(\mathbf{E}_s \hat{\mathbf{C}}_s \mathbf{V})$ will get larger as J increases.

Proposed Algorithm

To solve the problem confronted in the DR algorithm, we propose the following IR algorithm to improve the recovery performance. Note that, both the basis matrix \mathbf{V} and Ψ are the sampled data of the PSWFs with the same time bandwidth products, which are calculated by

$$2N_{nyq}W = 2 \times \frac{T}{T_{nyq}} \times \frac{B}{f_{nyq}} = 2TB. \quad (4.23)$$

Since matrix \mathbf{A} satisfies the RIP condition [20], \mathbf{A}_s is a full row rank matrix and the estimation of \mathbf{X}_s is

$$\hat{\mathbf{X}}_s = \mathbf{A}_s^+ \mathbf{Y} = \mathbf{A}_s^+ \mathbf{A}_s \mathbf{C}_s \Psi = \mathbf{C}_s \Psi, \quad (4.24)$$

we can interpolate $\hat{\mathbf{X}}_s = \mathbf{C}_s \Psi$ with the Slepian basis to obtain the estimation $\hat{\Theta}_s$ of $\mathbf{C}_s \mathbf{V}$. Then, the estimation of \mathbf{x} is

$$\hat{\mathbf{x}} = \text{diag}(\mathbf{E}_s \hat{\Theta}_s). \quad (4.25)$$

4.2.4 Performance Evaluation

This section evaluates the recovery performance of MWC under the non-modulated Slepian basis with the DR recovery algorithm and the IR recovery algorithm respectively.

Simulation Parameters

Consider the following multiband signal $x(t)$

$$x(t) = \sum_{i=1}^{K/2} \text{sinc}(2B(t - \tau_i)) \cos(2\pi f_i(t - \tau_i)), \quad (4.26)$$

where $K = 4$, $B = 25\text{MHz}$ and $f_{nyq} = 10\text{GHz}$, τ_i is the time offset and f_i is the carrier frequency. The system parameters are set as follows: the the number of the parallel channels is $m=30$, $f_s=f_p=50\text{MHz}$, and $M = L = 195$. The number of samples at each channel is set to be $N_s = 91$, and then we have $N_{nyq} = N_s \times M = 17745$. The performance metric is the recovery SNR which is defined as

$$\text{SNR}_{rec} = 20 \log_{10} \left(\frac{\|\mathbf{x}\|_2}{\|\mathbf{x} - \hat{\mathbf{x}}\|_2} \right) \text{ dB}. \quad (4.27)$$

Simulation Results

Firstly, Figure 4.1 illustrates the difference between the original signal and the best recovered signal with different basis and recovery algorithms in the noise-free environment. As shown in Figure 4.1, for the non-modulated Slepian basis, the IR algorithm can almost exactly reconstruct the original signal, while the DR algorithm has small recovery errors in both the main peaks and the side-lobes. For the DFT basis, although it does successfully

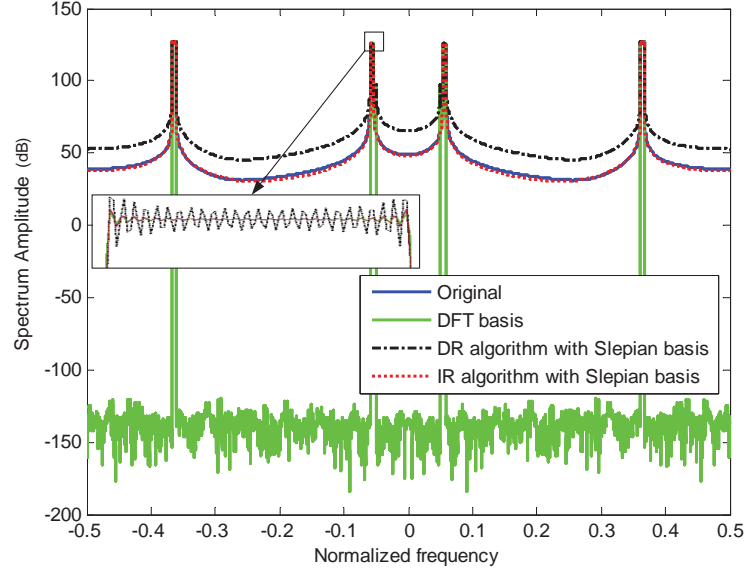


Figure 4.1: Illustration of the recovered signal with the non-modulated Slepian basis and the DFT basis, compared with the original signal.

capture the main peaks of each band, it misses all of the side-lobes of each band and has a number of spurious artifacts in regions where there is no significant frequency content in the original signal.

Figure 4.2 shows the recovery SNR of different recovery algorithms with different sizes of the Slepian basis in the noise free environment. The time bandwidth product of the non-modulated Slepian basis is $2N_{nyq}W = 91$. Firstly, it can be seen from Figure 4.2 that, the recovery SNR of the IR algorithm increases when the size of the Slepian basis J slightly exceeds the time-bandwidth product $2N_{nyq}W$, and then the recovery SNR decreases a little with the increase of J . Secondly, the recovery SNR with the DR algorithm decreases as J increases, which coincides with the analysis in Section 4.2.3. Obviously, the recovery SNR of the estimation with DFT basis remains constant as J increases.

Figure 4.3 shows the recovery SNR with different basis and recovery algorithms when SNR=10dB. By comparing Figure 4.3 with Figure 4.2, we can see that the recovery SNR of different basis and different algorithms deteriorates when noise is present. In the noisy

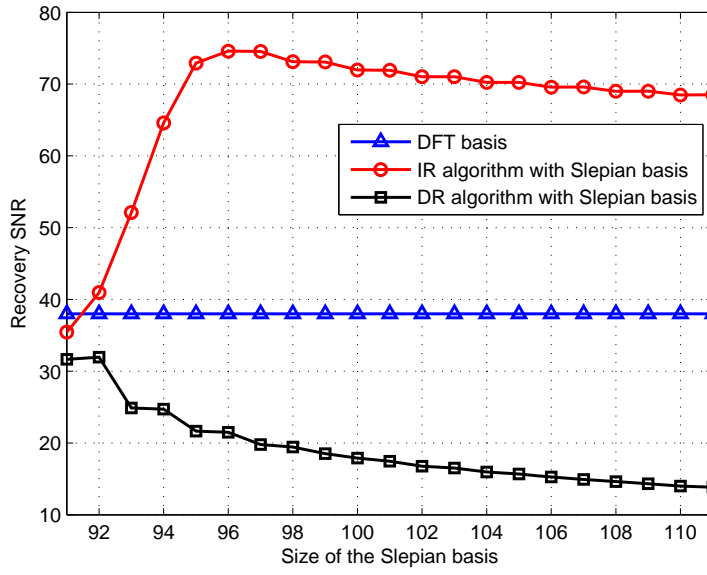


Figure 4.2: Comparison of the recovery SNR under the Slepian basis and the DFT basis versus the size of the Slepian basis in the noise-free environment.

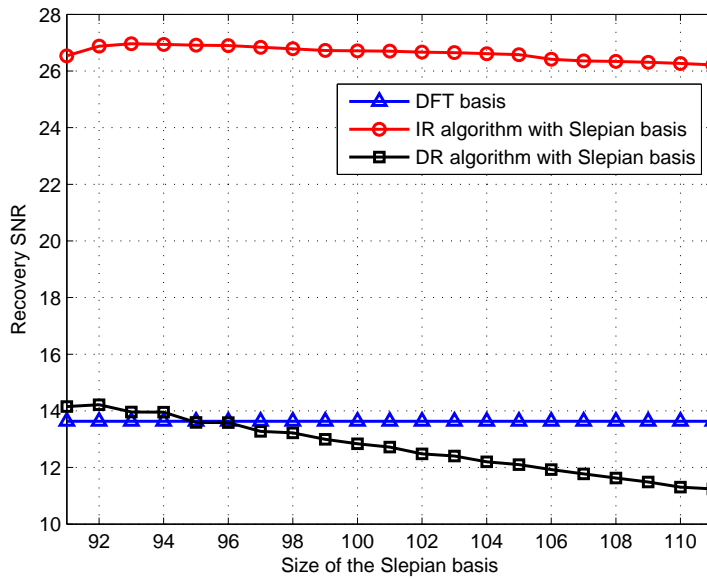


Figure 4.3: Comparison of the recovery SNR under the Slepian basis and the DFT basis versus the size of the Slepian basis with SNR=10dB.

environment, compared with the DFT basis, the non-modulated Slepian basis improves the recovery SNR by 13 dB, while it improves the recovery SNR by up to 35dB in the

noise-free environment.

Finally, we compare the size and complexity of the non-modulated Slepian basis in this chapter with the MM-Slepian dictionary in [97]. The size of the non-modulated Slepian basis Φ in this chapter is $J \times N_s = 96 \times 91$, and the size of the measurement matrix \mathbf{A} is $m \times M = 30 \times 195$. However, under the same simulation parameters, the size of the MM-Slepian dictionary and the corresponding measurement matrix in [97] should be respectively $N_{nyq} \times N_{nyq} = 17745 \times 17745$ and $\frac{N_{nyq}}{s} \times N_{nyq} = \frac{17745}{s} \times 17745$, where s is the sub-sampling factor. According to the analysis of BP and OMP recovery algorithm in [6] and [5], this significant dimension reduction will lead to a very remarkable decrease of the computational load in the recovery stage.

4.3 Random Circulant Orthogonal Matrix Based Analog CS

This section is organized as follows. Section 4.3.1 describes the RCOM-ACS scheme. Section 4.3.2 formulates the measurement matrix of RCOM-ACS scheme. Section 4.3.3 proves that the measurement matrix of the RCOM-ACS scheme satisfies the RIP condition. Section 4.3.5 presents the short processing time RCOM-ACS (SRCOM-ACS) scheme. Then, the performances of the proposed schemes are evaluated in Section 4.3.6.

4.3.1 Description of RCOM-ACS Scheme

This section presents the system model of the RCOM-ACS scheme and its mathematical formulation.

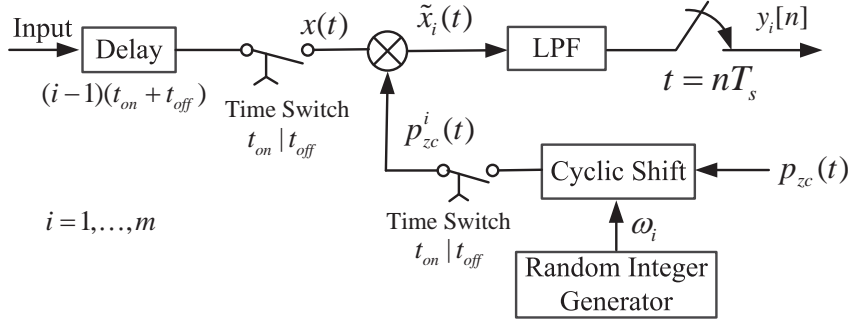


Figure 4.4: Block diagram of RCOM-ACS scheme.

System Model

Consider a multiband signal $x(t)$, whose frequency supports reside in a union of r disjoint bands which are spread over a very wide spectrum $\mathcal{F} = [-f_{nyq}/2, f_{nyq}/2]$, with the bandwidth of each band not exceeding W .

Figure 4.4 illustrates the work process of the RCOM-ACS scheme. Firstly, at the i^{th} time slice, the delayed input signal $x(t)$ is multiplied by mixing function $p_{zc}^i(t)$ with the aid of a time switch, which is turned on for t_{on} time and turned off for t_{off} time alternately, where t_{on} is equal to the time taken by the multiplication of $x(t)$ and $p_{zc}^i(t)$, t_{off} equals the processing time of the LPF and ADC. Secondly, the mixed signal $\tilde{x}_i(t)$ is filtered by the LPF with cutoff frequency $1/2T_s$. Finally, the filtered signal is sampled at rate $f_s = 1/T_s$ and the sampled data are $y_i[n]$ with $i = 1, \dots, m$.

To be specific, the input signal is delayed for $(i-1)(t_{on} + t_{off})$ time to make sure that the mixing function $p_{zc}^i(t)$ is multiplied with the same signal $x(t)$, where $i = 1, \dots, m$. The mixing function $p_{zc}^i(t)$ is the i^{th} cyclic shift of the T_p -periodic Zadoff-Chu sequence $p_{zc}(t)$, where the number of shifts ω_i is generated by the random integer generator.

Mathematic Formulation of the RCOM-ACS Scheme

The expression of the Zadoff-Chu sequence $p_{zc}(t)$ is

$$p_{zc}(t) = \beta_k = e^{-j\frac{\pi}{M}uk(k+1)}, k\frac{T_p}{M} \leq t \leq (k+1)\frac{T_p}{M}, \quad (4.28)$$

where $0 \leq k \leq M-1$, u is an integer and denotes the root of $p_{zc}(t)$, M is a prime number and represents the length of $p_{zc}(t)$, the expression of $p_{zc}^i(t)$ is

$$p_{zc}^i(t) = \alpha_{ik}, k\frac{T_p}{M} \leq t \leq (k+1)\frac{T_p}{M}, \quad (4.29)$$

where $1 \leq i \leq m$, $\boldsymbol{\alpha}_i = [\alpha_{i0}, \dots, \alpha_{i(M-1)}]^T$ is the ω_i -cyclic shift of $\boldsymbol{\beta} = [\beta_0, \dots, \beta_{M-1}]^T$, and ω_i obeys the discrete uniform distribution on $\{0, \dots, M-1\}$.

Since $p_{zc}^i(t)$ is T_p -periodic, it has a Fourier expansion $p_{zc}^i(t) = \sum_{l=-\infty}^{\infty} c_{il}e^{j2\pi lt/T_p}$. Then, the Fourier transform of $\tilde{x}_i(t) = x(t)p_{zc}^i(t)$ is

$$\tilde{X}_i(f) = \sum_{l=-\infty}^{\infty} c_{il}X(f - lf_p), \quad (4.30)$$

where $f_p = 1/T_p$, $X(f)$ is the Fourier transform of $x(t)$. Thus, the output of LPF in frequency domain is

$$Y_i(e^{j2\pi fT_s}) = \sum_{l=-L_0}^{L_0} c_{il}X(f - lf_p), \quad f \in \mathcal{F}_s, \quad (4.31)$$

where $\mathcal{F}_s = [-f_s/2, f_s/2]$, $Y_i(e^{j2\pi fT_s})$ is the discrete-time Fourier transform (DTFT) of $y_i[n]$, L_0 is chosen as an integer satisfying $L_0 \geq \lceil (f_{nyq} + f_s)/2f_p \rceil - 1$ so that (4.31) contains all nonzero contributions of $X(f)$ over \mathcal{F}_s .

4.3.2 Measurement Matrix of RCOM-ACS Scheme

To derive the expression of the measurement matrix of the RCOM-ACS scheme, we rewrite (4.31) as

$$\mathbf{y}(f) = \mathbf{A}\mathbf{z}(f), \quad f \in \mathcal{F}_s, \quad (4.32)$$

where \mathbf{A} is the $m \times L$ measurement matrix with $\mathbf{A}_{il} = c_{i,-l} = c_{il}^*$ and $L = 2L_0 + 1$, $\mathbf{y}(f) = [y_1(f), \dots, y_m(f)]^T$ with $y_i(f) = Y_i(e^{j2\pi f T_s})$, $f \in \mathcal{F}_s$, $\mathbf{z}(f) = [z_1(f), \dots, z_L(f)]^T$ with $z_l(f) = X(f + (l - L_0 - 1)f_p)$, $f \in \mathcal{F}_s$.

To investigate whether the measurement matrix \mathbf{A} satisfies the RIP condition, matrix \mathbf{A} is further decomposed into a combination of structured matrices as follows.

Proposition 4.1. *The measurement matrix \mathbf{A} of RCOM-ACS scheme can be decomposed into*

$$\mathbf{A} = \mathbf{R}_\Omega \mathbf{B} \mathbf{G} \mathbf{D}, \quad (4.33)$$

where \mathbf{R}_Ω is an $m \times M$ random selector, \mathbf{B} is a $M \times M$ circulant orthogonal matrix, \mathbf{G} is a $M \times L$ reordered column subset of a $M \times M$ Discrete Fourier Transform (DFT) matrix, \mathbf{D} is a $L \times L$ diagonal matrix with non-zero element in diagonal.

Proof. The $(i, l)^{th}$ entry of the $m \times L$ matrix \mathbf{A} is $\mathbf{A}_{il} = c_{i,-l} = c_{il}^*$, where $i = 1, \dots, m$, $l = 1, \dots, L$ and c_{il} is the Fourier coefficient of the T_p -periodic function $p_{zc}^i(t)$:

$$c_{il} = \frac{1}{T_p} \sum_{k=0}^{M-1} \alpha_{ik} e^{-j \frac{2\pi}{M} lk} \int_0^{\frac{T_p}{M}} e^{-j \frac{2\pi}{T_p} lt} dt. \quad (4.34)$$

The integral can be calculated as follows:

$$d_l = \frac{1}{T_p} \int_0^{\frac{T_p}{M}} e^{-j \frac{2\pi}{T_p} lt} dt = \begin{cases} 1/M & l = 0 \\ (1 - \theta^l)/(2j\pi l) & l \neq 0 \end{cases}, \quad (4.35)$$

where $\theta = e^{-j2\pi/M}$, then we have

$$c_{il} = d_l \sum_{k=0}^{M-1} \alpha_{ik} \theta^{lk}. \quad (4.36)$$

For $i = 1, \dots, m$ and $k = 0, \dots, M-1$, α_{ik} forms a $m \times M$ matrix \mathbf{S} with $\mathbf{S}_{ik} = \alpha_{ik}$. Since $\boldsymbol{\alpha}_i = [\alpha_{i0}, \dots, \alpha_{i(M-1)}]^T$ is the ω_i -cyclic shift of $\boldsymbol{\beta} = [\beta_0, \dots, \beta_{M-1}]^T$, matrix \mathbf{S} is actually a row sub-matrix of the circulant matrix \mathbf{B} indexed by the set $\Omega = \{\omega_1, \dots, \omega_m\}$, where \mathbf{B}

is

$$\mathbf{B} = \begin{bmatrix} \beta_0 & \beta_1 & \cdots & \beta_{M-1} \\ \beta_{M-1} & \beta_0 & \cdots & \beta_{M-2} \\ \vdots & \vdots & \ddots & \vdots \\ \beta_1 & \beta_2 & \cdots & \beta_0 \end{bmatrix}. \quad (4.37)$$

Define $\mathbf{R}_\Omega \in \mathbb{R}^{m \times M}$ as an operator restricting a vector to the entries listed in Ω , we have $\mathbf{S} = \mathbf{R}_\Omega \mathbf{B}$. Let $\mathbf{g}_i = [\theta^{0 \cdot i}, \dots, \theta^{(M-1) \cdot i}]^T$ and $\mathbf{G} = [\mathbf{g}_{L_0}, \dots, \mathbf{g}_{-L_0}]$, it is required that $M \geq L$ to make sure that \mathbf{G} contains no identical columns. For simplicity, we assume $M = L$ in this chapter since \mathbf{G} is unitary when $M = L$. Then, according to (4.36), we have $\mathbf{A} = \mathbf{R}_\Omega \mathbf{B} \mathbf{G} \mathbf{D}$, where $\mathbf{D} = \text{diag}(d_{L_0}, \dots, d_{-L_0})$. \square

4.3.3 Conditions for Successful Recovery

As stated in Section 2.1.2, the RIP condition is the necessary condition for the successful recovery of the sparse signal. In analog CS, besides the RIP condition, the parameters of the devices, i.e., the cutoff frequency of LPFs and the sampling rate of the low-rate ADCs, should also meet some conditions. Thus, we firstly specify the conditions for successful recovery of the RCOM-ACS scheme, and then we extend the RCOM-ACS scheme to a more general form while guaranteeing its recovery performance.

Conditions for Successful Recovery of RCOM-ACS Scheme

The conditions for successful recovery in the RCOM-ACS scheme are stated as follows.

Theorem 4.1. *For any $\varepsilon > 1$ and $r > 2$, when M is prime and equal to L , if $f_s \geq f_p > W$ and the number of rows in matrix \mathbf{A} satisfies*

$$m \geq (C\varepsilon r \log M) \log(C\varepsilon r \log M) \log^2 r, \quad (4.38)$$

then the measurement matrix $\mathbf{A} = \mathbf{R}_\Omega \mathbf{B} \mathbf{G} \mathbf{D}$ satisfies the RIP condition (2.6) with probability at least $1 - 5e^{-c\varepsilon}$, and $\mathbf{z}(f)$ is the unique r -sparse solution to (4.32), where C and c are some absolute constants.

Proof. The proof of Theorem 4.1 is divided into the following two parts:

1) *Conditions for Device Parameters:*

The choice of $f_p > W$ ensures that every band contributes only a single non-zero value to $\mathbf{z}(f)$. In other words, the choice of $f_p > W$ guarantees that $\mathbf{z}(f)$ is r -sparse in $f \in \mathcal{F}_s$. If $f_s < f_p$, then the sum in (4.31) lacks contribution from $X(f)$ for some $f \in \mathcal{F}$. Thus, $f_s \geq f_p$ is necessary.

2) *RIP condition for RCOM-ACS scheme:*

Since the diagonal matrix \mathbf{D} has nonzero diagonals, the support of $\mathbf{D}\mathbf{u}$ is equal to that of \mathbf{u} for any vector \mathbf{u} . Therefore, we just need to verify that $\mathbf{R}_\Omega \mathbf{B} \mathbf{G}$ satisfies the RIP condition.

The restricted isometry inequality (2.2) indicates that the singular values of \mathbf{A}_T lie between $\sqrt{1 - \delta_r}$ and $\sqrt{1 + \delta_r}$. Notice that, for any $m \times M$ matrix \mathbf{P} , its singular values remain unchanged when multiplying \mathbf{P} by a unitary matrix \mathbf{U} . Therefore, $\mathbf{P}\mathbf{U}$ will satisfy the RIP condition if \mathbf{P} does. Since $M = L$, matrix \mathbf{G} is unitary. Because M is prime, the circularly shifted versions of Zadoff-Chu sequence are orthogonal to each other, i.e., matrix \mathbf{B} is unitary.

Then, $\mathbf{A} = \mathbf{R}_\Omega \mathbf{B} \mathbf{G} \mathbf{D}$ will satisfy the RIP condition if \mathbf{R}_Ω does. According to [43] (Theorem 3.3), for any $\varepsilon > 1$ and $r > 2$, if the cardinality of a random subset Ω , i.e., the number of rows in random selector matrix \mathbf{R}_Ω , satisfies $m \geq (C\varepsilon r \log M) \log(C\varepsilon r \log M) \log^2 r$, then \mathbf{R}_Ω will satisfy the RIP condition (2.6) with probability at least $1 - 5e^{-c\varepsilon}$, where C and c are some absolute constants.

Therefore, if M is prime and $M = L$, $f_s \geq f_p > W$, m satisfies (4.38), then the measurement matrix \mathbf{A} satisfies the RIP condition and $\mathbf{z}(f)$ is the unique r -sparse solution of (4.32). \square

Remark:

- (1) The polynomial probability of success $1 - M^{-O(1)}$ can be obtained by letting $\varepsilon = O(\log M)$, the required number of measurements is $m = O(r \log^2 M \log^3 r)$.
- (2) The RCOM-ACS scheme accelerates the recovery algorithms compared with MWC,

because the measurement matrix $\mathbf{A} = \mathbf{R}_\Omega \mathbf{B} \mathbf{G} \mathbf{D}$ admits the fast matrix-vector multiplication due to the existence of circulant matrix \mathbf{B} .

4.3.4 Extensions of RCOM-ACS Scheme

Besides the Zadoff-Chu sequence, this chapter extends the RCOM-ACS scheme by allowing the mixing function to be any other sequence whose Fourier transform has the unit magnitude. The mathematic formulation and the proof of this conclusion are stated as follows.

Lemma 4.1. *Suppose \mathbf{h} is an $M \times 1$ sequence vector, $h(t)$ is the corresponding piecewise constant function. Let $\mathbf{\Lambda} = \text{diag}(\mathbf{F}_M \mathbf{h})$, where \mathbf{F}_M is the DFT matrix with $\mathbf{F}_M(i, k) = 1/\sqrt{M} \times e^{-j2\pi(i-1)(k-1)/M}$. If $\mathbf{\Lambda}^* \mathbf{\Lambda} = \mathbf{I}$, then $h(t)$ can be used as the mixing function of RCOM-ACS scheme, and the measurement matrix generated by \mathbf{h} satisfies the RIP condition.*

Proof. The circulant matrix \mathbf{H} generated by circularly shifting \mathbf{h} can be diagonalized by the DFT matrix \mathbf{F}_M , i.e., $\mathbf{H} = \mathbf{F}_M^* \mathbf{\Lambda} \mathbf{F}_M$. If $\mathbf{\Lambda}^* \mathbf{\Lambda} = \mathbf{I}$, then

$$\mathbf{H}^* \mathbf{H} = \mathbf{F}_M \mathbf{\Lambda}^* \mathbf{F}_M^* \mathbf{F}_M \mathbf{\Lambda} \mathbf{F}_M^* = \mathbf{I}. \quad (4.39)$$

That is to say, the circulant matrix \mathbf{H} is unitary. According to Theorem 4.1, if m satisfies (4.38), then the measurement matrix $\mathbf{A} = \mathbf{R}_\Omega \mathbf{H} \mathbf{G} \mathbf{D}$ satisfies the RIP condition and $\mathbf{z}(f)$ is the unique solution to $\mathbf{y}(f) = \mathbf{R}_\Omega \mathbf{H} \mathbf{G} \mathbf{D} \mathbf{z}(f)$, with $h(t)$ being the mixing function of RCOM-ACS scheme. \square

4.3.5 Fast Processing RCOM-ACS Scheme

Although the RCOM-ACS scheme reduces the number of physical parallel channels from m to 1, it does increase the processing time. To make a good tradeoff between hardware complexity and processing time, a SRCOM-ACS scheme is proposed.

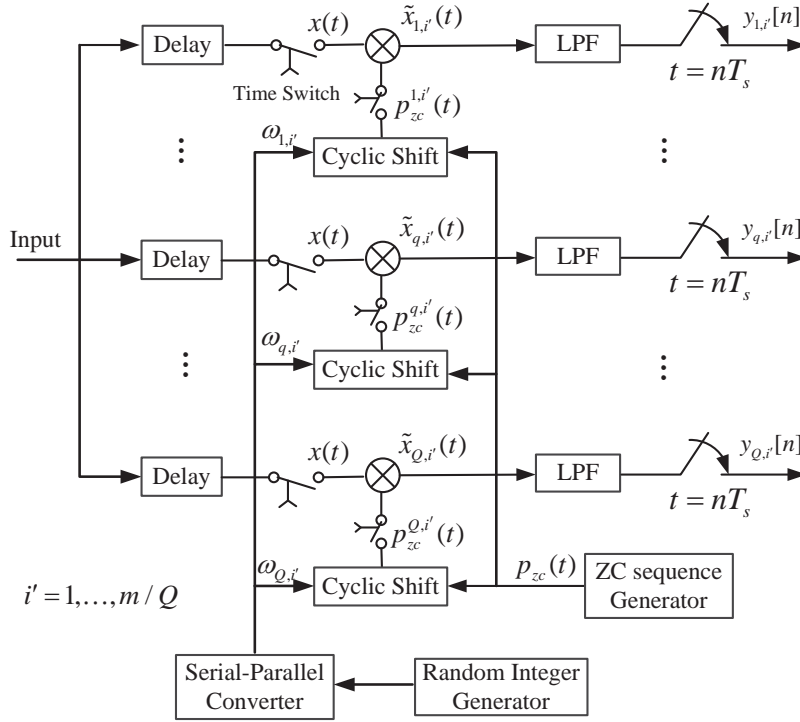


Figure 4.5: Block diagram of SRCOM-ACS scheme.

Description of SRCOM-ACS scheme

Figure 4.5 illustrates the SRCOM-ACS scheme, which uses Q physical parallel channels, with each physical channel equivalent to m/Q channels of MWC, assuming m/Q is an integer. For $q = 1, \dots, Q$ and $i' = 1, \dots, m/Q$, the mixing functions $p_{zc}^{q,i'}(t)$ are the $\omega_{q,i'}$ -cyclic shifts of the same Zadoff-Chu sequence $p_{zc}(t)$, the numbers $\omega_{q,i'}$ are generated by the same random integer generator and input into each channel by a serial-parallel converter.

The operational process of the SRCOM-ACS scheme is similar to that of RCOM-ACS scheme. Firstly, at the i'^{th} cyclic shift of the q^{th} channel, the input signal is delayed for $(i' - 1)(t_{on} + t_{off})$ time. Secondly, the delayed input signal $x(t)$ is multiplied by mixing function $p_{zc}^{q,i'}(t)$ with the aid of a time switch. Thirdly, the mixed signal $\tilde{x}_{q,i'}(t)$ is filtered by the LPF with cutoff frequency $1/2T_s$. Finally, the filtered signal is sampled at rate

$f_s = 1/T_s$ and the sampled data are $y_{q,i'}[n]$.

Discussion of SRCOM-ACS Scheme

This subsection discusses the choice of the mixing function and the RIP condition for the SRCOM-ACS scheme.

1) *Choice of the Mixing Function.* The cross correlation between two prime-length (M) Zadoff-Chu sequences, i.e., different u , is constant $1/\sqrt{M}$. Therefore, the circulant matrix generated by two or more prime length Zadoff-Chu sequences is not orthogonal and will not meet the RIP condition according to Theorem 4.1. Therefore, as shown in Figure 4.5, the same Zadoff-Chu sequence is adopted in the SRCOM-ACS scheme to produce the mixing functions for the Q parallel channels.

2) *RIP condition for SRCOM-ACS Scheme.* Since the SRCOM-ACS scheme generates the mixing functions by randomly and circularly shifting the same Zadoff-Chu sequence, it has the same mathematical formulation and measurement matrix as those of the RCOM-ACS scheme. Consequently, the measurement matrix of the SRCOM-ACS scheme satisfies the RIP condition and the performance of the SRCOM-ACS is the same as that of the RCOM-ACS scheme.

4.3.6 Performance Evaluation

The performances of the proposed schemes are evaluated against MWC and the collapsing method. The performance metric is the empirical recovery rate, which is defined as the percentage of correct support recovery.

Table 4.1: Cost of Different Schemes

Scheme	Number m'	Processing time	Sampling rate
MWC	m	t_0	51.3MHz
Collapsing	$m/5$	$t_0 + t_s + t_o$	256.4MHz
RCOM-ACS	1	mt_0	51.3MHz
SRCOM-ACS	Q	$(m/Q)t_0$	51.3MHz

Simulation Parameters and Recovery Algorithms

The schemes are tested on the noisy signal $x(t) + w(t)$, where $w(t)$ is zero-mean white Gaussian noise and the expression of $x(t)$ is

$$x(t) = \sum_{i=1}^{r/2} \text{sinc}(W(t - \tau_i)) \cos(2\pi f_i(t - \tau_i)), \quad (4.40)$$

in which $r = 6$, τ_i is the time offset, $W = 50\text{MHz}$, f_i is chosen uniformly and randomly in $\mathcal{F} = [-5\text{GHz}, 5\text{GHz}]$, the signal-to-noise ratio (SNR) is 10dB.

The problem (4.32) to be solved in the RCOM-ACS scheme is actually an IMV problem [101], because f is continuous and \mathcal{F}_s has infinite cardinality. To reconstruct $\mathbf{z}(f)$ from (4.32), we use the method in [2] and [101] to firstly convert the IMV problem (4.32) into a MMV [100] problem. Then, MMV-Basis Pursuit (M-BP) [102] recovery algorithm and MMV-Orthogonal Matching Pursuit (M-OMP) [102] recovery algorithm are used to reconstruct $x(t)$ respectively.

Simulation Results

The costs of different schemes are shown in Table 4.1, where t_0 denotes the processing time of MWC, t_s and t_o represent the additional signal processing time and observation time for the collapsing method respectively. The number of actual physical parallel channels m' of MWC, the collapsing method, the RCOM-ACS and SRCOM-ACS scheme are

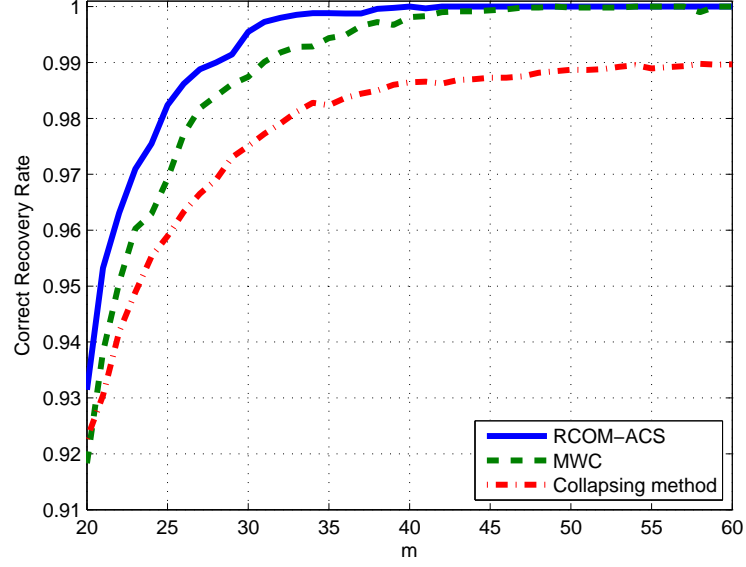


Figure 4.6: Performance comparison among RCOM-ACS scheme, MWC and the collapsing method with M-BP recovery algorithm.

m , $m/5$, 1 and Q respectively, where m is the number of equivalent parallel channels for the different schemes. Therefore, MWC has the highest hardware complexity and RCOM-ACS has the lowest hardware complexity. Conversely, MWC has the shortest processing time, while the RCOM-ACS scheme and the collapsing method have a much longer processing time. What's more, the collapsing method has the highest sampling rate at each parallel channel, while RCOM-ACS and SRCOM-ACS scheme have the same sampling rate as that of MWC.

Figure 4.6 and Figure 4.7 report the percentage of correct recovery for various numbers m with the M-BP recovery algorithm and the M-OMP recovery algorithm, respectively. It is evident that, with both of the two recovery algorithms, the RCOM-ACS scheme has the best recovery performance compared with MWC and the collapsing method, while the collapsing method degrades the recovery performance compared with MWC. Specifically, the RCOM-ACS scheme outperforms the collapsing method for each m and has better recovery performance than MWC especially when m is small. For the RCOM-ACS and

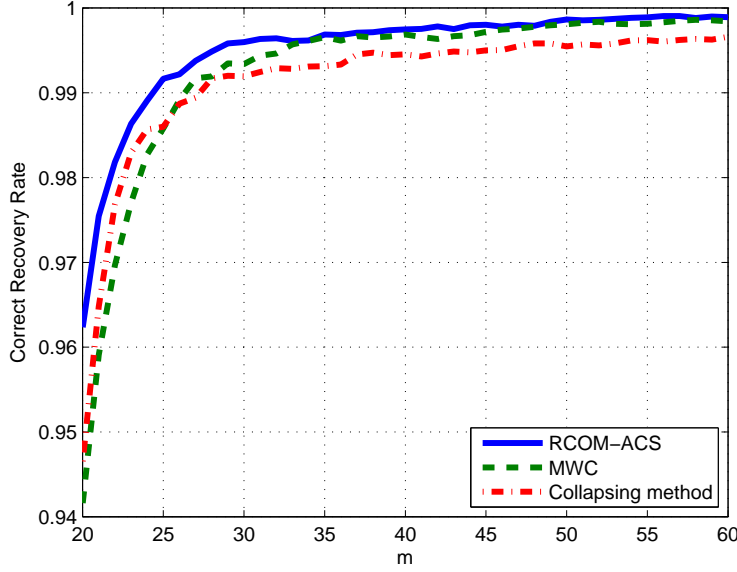


Figure 4.7: Performance comparison among RCOM-ACS scheme, MWC and the collapsing method with M-OMP recovery algorithm.

MWC schemes, the M-OMP recovery algorithm outperforms the M-BP recovery algorithm when m is small, whilst M-BP recovery algorithm has better performance than M-OMP when m is large. For the collapsing method, the M-OMP recovery algorithm outperforms the M-BP recovery algorithm for each m . As stated in section 4.3.5, the SRCOM-ACS scheme has the same recovery performance as that of the RCOM-ACS scheme and strikes a good balance between processing time and hardware complexity.

4.4 Summary

Based on the structured matrix, this chapter improves the recovery performance and reduces the hardware complexity of analog CS.

Firstly, to improve the recovery performance while keeping low computational complexity, this chapter proposes to use the non-modulated Slepian basis to represent the modulated and bandlimited version of the multiband signal based on MWC rather than

using the MM-Slepian dictionary to represent the whole original multiband signal. Furthermore, based on the derivation of MWC under the non-modulated Slepian basis, we propose an IR recovery algorithm to take full advantage of the Slepian basis. Simulation results verify that, compared with the DFT basis, the non-modulated Slepian basis combined with the IR algorithm improves the recovery SNR by up to 35 dB with a low recovery computational load in the noise-free environment.

Secondly, to reduce the hardware complexity of analog CS, this chapter proposed the RCOM-ACS scheme, which reduces the number of parallel channels in MWC from m to 1 at the expense of a longer processing time. It is proved that if $m = O(r \log^2 M \log^3 r)$, then the $m \times M$ measurement matrix $\mathbf{A} = \mathbf{R}_\Omega \mathbf{B} \mathbf{G} \mathbf{D}$ of the RCOM-ACS scheme satisfies the RIP condition with probability $1 - M^{-O(1)}$. Simulation results show that the RCOM-ACS scheme has the best recovery performance compared with the MWC scheme and the collapsing method. Furthermore, to balance the processing time with hardware complexity, a SRCOM-ACS scheme is proposed, which has the same recovery performance as that of the RCOM-ACS scheme.

After the study of analog CS in this chapter, we will discuss the application of analog CS in wireless networks of analog CS in the next chapter.

Chapter 5

Compressed Wideband Spectrum Sensing for CRNs

After the research on analog CS in Chapter 4, in this chapter we will investigate the application of analog CS in CRs, especially in WSS.

5.1 Introduction

In the early stage of wireless communications, the wireless spectrum were uniformly assigned and managed by governments. With the rapid development of wireless communications, the limited spectrum can not meet the wide bandwidth and high data rate requirements. However, according to the report from the Federal Communications Commission (FCC) [33] in 2002, only some frequency bands are heavily used, while the other frequency bands are largely unoccupied most of the time or only partially occupied. In other words, spectrum access is a more significant problem than physical scarcity of spectrum. Therefore, CR [34] [24] is proposed to allow the unlicensed (secondary) users to opportunistically access the temporarily unused spectrum. So, the first step for CR is to detect spectrum holes, i.e., spectrum sensing.

Generally speaking, spectrum sensing techniques can be classified as the following three kinds: energy detection [103], coherent detection [104] and characteristic detection [105]. The above three kinds of methods are designed for narrow-band signals. Recently, WSS has attracted great attention for its advantages and challenges. Owing to the spectrum awareness over a wide frequency band, WSS provides more efficient spectrum access in CR networks than narrow band detection [24].

Unfortunately, WSS is currently prevented from being put in practice mainly due to the following challenges. Firstly, WSS requires an extremely high sampling rate ADC (analog-to-digital converter), which is very expensive or even infeasible [106]. Secondly, for spectrum detection, there is an SNR wall below which detection becomes impossible [107]. Thirdly, WSS also suffers from noise uncertainty when estimating the noise's variance [107]. Besides, the existing WSS algorithms are too complex to satisfy the timing requirement of rapid detection. For example, WSS is implemented by a complex optimization algorithm in [108] and by a wavelet transform in [109].

Compressed WSS given in [17] has resolved the challenge of extremely high sampling rate by taking advantage of the CS theory and the sparsity of the wideband signal in the frequency domain. However, the method in [17] is actually based on discrete CS, which can not reduce the sampling rate of analog wideband signals. Then, [21] proposed a parallel structure to enable the sub-Nyquist sampling. Nevertheless, compressed WSS so far has not solved the other three challenges confronted by WSS.

To solve the above challenges, we propose a novel WSS scheme, namely MCWSS scheme. The main contributions of this chapter are stated as follows: Firstly, we propose a novel CRL_2 (combining relevance via L_2 norm) algorithm to jointly recover multi-antenna signals making use of their common sparsity. Then, a CBS (combining before sampling) algorithm is designed to increase the signal's SNR and to improve the recovery performance. For the detection step, we propose a novel and low-complexity divided-averaged

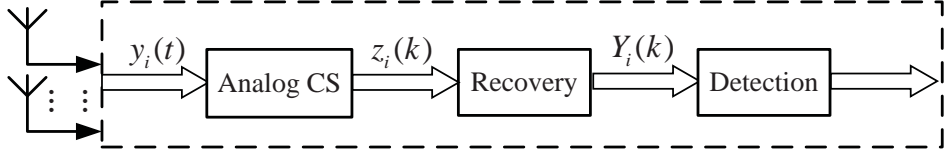


Figure 5.1: System model of MCWSS scheme.

(DA) algorithm, which has good performance and does not need to estimate the noise variance. Hence, the DA algorithm also overcomes the noise uncertainty problem. Simulation results show that, our proposed scheme can improve the detection performance at about 28% of Nyquist sampling rate.

The rest of this chapter is organized as follows. Section 5.2 describes the system model of the MCWSS scheme. Section 5.3 presents the DA algorithm, and gives the theory derivations in both the single antenna scenario and the multi-antenna scenario. Section 5.4 details the proposed CS recovery algorithms for multi-antenna signals, i.e., the CRL₂ algorithm and CBS algorithm. Section 5.5 and Section 5.6 demonstrate the simulation results and give conclusions, respectively.

5.2 System Model

The system model of MCWSS is illustrated in Figure 5.1. The received wideband multi-antenna signals $y_i(t), i = 1, \dots, N_r$ (where N_r is the number of CR user receive antennas) are firstly sampled by analog CS, the output of analog CS is the sub-Nyquist sampled data $z_i(k)$; then $z_i(k)$ is recovered into Nyquist rate data $Y_i(k)$ with a CS recovery algorithm; ultimately, wideband detection is carried out to detect the presence of the primary user's signal.

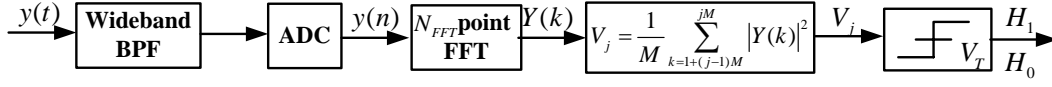


Figure 5.2: Block diagram of DA algorithm.

5.3 DA Algorithm for Wideband Spectrum Sensing

To make the WSS algorithm easy to implement, we devise a novel DA algorithm, which has good performance with low complexity.

5.3.1 Description of DA algorithm

The procedures of the DA algorithm are illustrated in Figure 5.2. Firstly, the received signal $y(t)$ is filtered, sampled, and then transformed into $Y(k), k = 1, \dots, N_{FFT}$ with a N_{FFT} -point fast Fourier transform (FFT). Secondly, $Y(k), k = 1, \dots, N_{FFT}$ is divided into J non-overlapping sub-bands. Thirdly, the j^{th} sub-band's energy V_j is calculated and compared with a threshold V_T to decide whether the j^{th} sub-band is occupied or not for $j = 1, \dots, J$.

Obviously, the key problem of the DA algorithm is how to set the threshold. According to the FCC's report [33], only a few sub-bands of the wideband signal are occupied. The average power of the wideband signal is small and can be approximated to the noise variance. Therefore, we set the average power of the wideband signal as the threshold, which can dynamically change with the actual noise variance. In other words, the DA algorithm bypasses the need for estimation of noise variance and overcomes the noise uncertainty.

5.3.2 Theoretical Analysis of DA algorithm

Single antenna scenario

The detection problem can be formulated into a binary hypothesis problem

$$Y(k) = \begin{cases} w(k) & H_0 \\ s(k) + w(k) & H_1 \end{cases}, \quad (5.1)$$

where $s(k)$, $w(k)$ and $Y(k)$ represent the k^{th} element of the sampled and FFT transformed primary user's signal, additive Gaussian noise (AWGN), and the received signal respectively. The noise $w(k)$ obeys a complex Gaussian distribution with zero mean and variance σ_w^2 , while $s(k)$ is assumed to be deterministic.

The test statistic (the energy of the j^{th} sub-band) is

$$V_j = \frac{1}{M} \sum_{k=1+(j-1)M}^{jM} |Y(k)|^2 \sim \begin{cases} \chi_{2M}^2 & H_0 \\ \chi_{2M,\lambda}^2 & H_1 \end{cases}, \quad (5.2)$$

where M is the number of points in the j^{th} sub-band. Under hypothesis H_0 , V_j follows a chi-square (χ^2) distribution with $2M$ degrees of freedom; under hypothesis H_1 , V_j obeys a non-central chi-square distribution with $2M$ degrees of freedom and a non-central parameter $\lambda = 2M\gamma/\mu$, where γ denotes the SNR of the wideband signal, μ denotes the sparsity of the wideband signal and is usually much less than one. Under hypothesis H_1 , the SNR of each sub-band is γ/μ , which is much higher than γ . The SNR improvement can be seen as the processing gain of the DA algorithm. The expression of threshold V_T is

$$V_T = \frac{1}{N_{FFT}} \sum_{k=1}^{N_{FFT}} |Y(k)|^2 \approx \bar{P}_s + \sigma_w^2, \quad (5.3)$$

where \bar{P}_s denotes the average power of the wideband signal. The detection probability $P_d = p(H_1|H_1)$ and false alarm probability $P_{fa} = p(H_1|H_0)$ are respectively

$$P_d = 1 - F_{2M,\lambda}(2M(1 + \gamma)), \quad (5.4)$$

$$P_{fa} = 1 - F_{2M}(2M(1 + \gamma)), \quad (5.5)$$

where $F_{2M,\lambda}(\cdot)$ denotes the cumulative distributed function (CDF) of non-central chi-square distribution $\chi_{2M,\lambda}^2$, $F_{2M}(\cdot)$ denotes the CDF of chi-square distribution χ_{2M}^2 .

Multi-antenna scenario

Since multi-antenna spectrum detection is one of our study objects, the performance of the DA algorithm in multi-antenna scenario is investigated. The signal model of multi-antenna spectrum detection is

$$Y_i(k) = \begin{cases} w_i(k) & H_0 \\ s(k) + w_i(k) & H_1 \end{cases} \text{ for } i = 1, \dots, N_r, \quad (5.6)$$

where $Y_i(k)$ is the k^{th} element of the received signal on the i^{th} antenna, $w_i(k), i = 1 \dots N_r$ is the k^{th} element of the independent and identically distributed (i.i.d.) Gaussian noise.

For multi-antenna spectrum detection, we consider two kinds of methods: one is combining the multi-antenna signals before detection, which is named as the pre-combining method; the other is combining the detection results, termed the post-combining method. Two pre-combining methods and one post-combining method are investigated sequentially in what follows.

a) Equal gain combining (EGC): The EGC combined signal is $Y'(k) = \sum_{i=1}^{N_r} Y_i(k)/N_r$. The detection probability $P_{d,EGC}$ and false alarm probability $P_{fa,EGC}$ with EGC method are

$$P_{d,EGC} = 1 - F_{2M,\lambda'}(2M(1 + N_r\gamma)), \quad (5.7)$$

$$P_{fa,EGC} = 1 - F_{2M}(2M(1 + N_r\gamma)), \quad (5.8)$$

where $\lambda' = 2MN_r\gamma/\mu$, and γ is the SNR of each antenna's signal. Compared with the single antenna scenario, EGC increases the signals' SNR from γ to $N_r\gamma$.

b) Square law combining (SLC): The SLC combined signal is $Y''(k) = \sum_{i=1}^{N_r} |Y_i(k)|^2/N_r$. The detection probability $P_{d,SLC}$ and false alarm probability $P_{fa,SLC}$ with the SLC method are

$$P_{d,SLC} = 1 - F_{2MN_r, \lambda''}(2MN_r(1 + \gamma)), \quad (5.9)$$

$$P_{fa,SLC} = 1 - F_{2MN_r}(2MN_r(1 + \gamma)), \quad (5.10)$$

where $\lambda'' = 2MN_r\gamma/\mu$. Compared with the single antenna scenario, the SLC method increases the degrees of freedom from $2M$ to $N_r \times 2M$. Since $2M \times J = N_{FFT}$, SLC is equivalent to increasing the number of FFT points.

c) "K out of N": "K out of N" principle means that if K antennas out of N_r antennas detect the primary user, then we decide the primary user is present. The detection probability $P_{d,K/N}$ and the false alarm probability $P_{fa,K/N}$ with the "K out of N" method are

$$P_{d,K/N} = \sum_{k=K}^{N_r} C_{N_r}^k (P_d)^k (1 - P_d)^{N_r-k}, \quad (5.11)$$

$$P_{fa,K/N} = \sum_{k=K}^{N_r} C_{N_r}^k (P_{fa})^k (1 - P_{fa})^{N_r-k}, \quad (5.12)$$

where P_d and P_{fa} are the detection probability and false alarm probability of a single antenna respectively. Since (5.11) and (5.12) have the same expression, $P_{d,K/N}$ follows the same trend as $P_{fa,K/N}$.

5.3.3 Performance Evaluation of DA algorithm

This subsection firstly demonstrates the performance gain of the DA algorithm compared with narrow band detection, e.g., the constant false alarm rate (CFAR) method presented in [103]. Then the performance of the DA algorithm in the multi-antenna scenario is evaluated.

The detection probability $P_{d,CFAR}$ of the CFAR method is

$$P_{d,CFAR} = Q((Q^{-1}(P_{fa,c}) - \gamma' \sqrt{M'/2})/(1 + \gamma')), \quad (5.13)$$

where $P_{fa,c}$ is the prescribed constant false alarm probability, γ' is the SNR of the narrow band signal, M' is the number of the sampling points. The theoretical values of the DA algorithm and the CFAR method are shown in Figure 5.3, from which we can conclude that the CFAR method can not achieve high detection probability and low false alarm probability simultaneously. The red lines and blue lines in Figure 5.3 illustrate the performance gain of the DA algorithm.

Theoretical values of the EGC, SLC and “K out of N” method for the DA algorithm in the multi-antenna scenario are shown by the solid lines in Figure 5.4 and Figure 5.5. From Figure 5.4 and 5.5, we can conclude that the pre-combining methods (EGC and SLC) increase p_d while decreasing p_{fa} , while the post-combining method (“K out of N”) either increases (e.g. “2 out of 4”) both p_d and p_{fa} at the same time, or decreases (e.g. “3 out of 4”) both p_d and p_{fa} simultaneously. Therefore, in Figure 5.4 and 5.5, there are intersections between the lines of the “K out of N” method and the lines of the other methods. In conclusion, the EGC method is the best method to process multi-antenna signals, the pre-combining method is better than the post-combining method in the multi-antenna scenario.

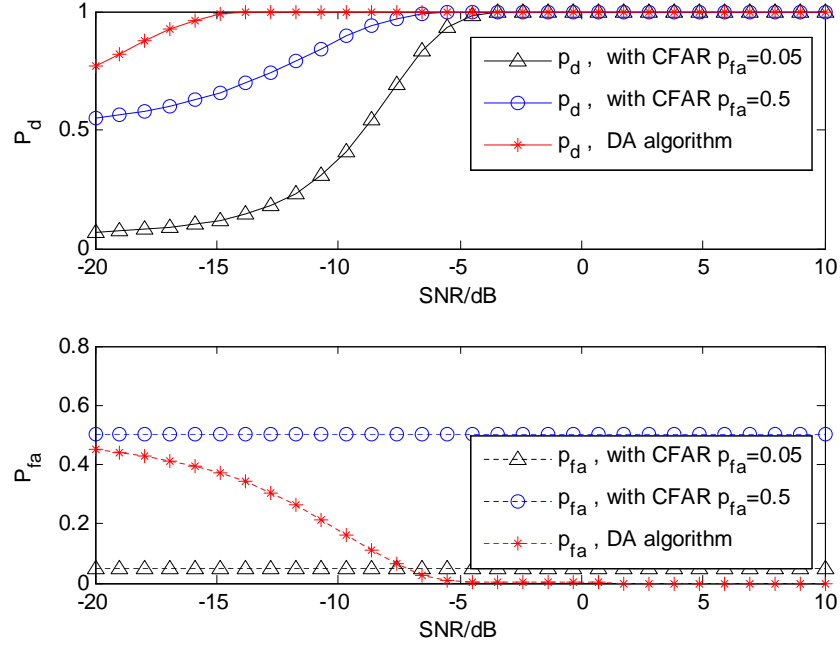


Figure 5.3: Performance gain of DA algorithm compared with CFAR.

5.3.4 Extended Research on Spectrum Sensing and Data Transmission

From the theoretical analysis in Section 5.3.2 and the numerical simulation in Section 5.3.3, we can conclude that the larger the number of sampling points, i.e., the longer spectrum sensing time, the better the detection performance. However, the longer the spectrum sensing time, the smaller throughput of CR system. In other words, this is a contradiction in CRs, i.e., to simultaneously minimize the interference caused to the primary (licensed) system, and maximize the throughput of the secondary (unlicensed) system.

To resolve the above challenge, we propose an interference-constrained adaptive simultaneous spectrum sensing and data transmission (ICASST) scheme. In the ICASST scheme, taking advantage of the statistic information of PUs activities, the operation

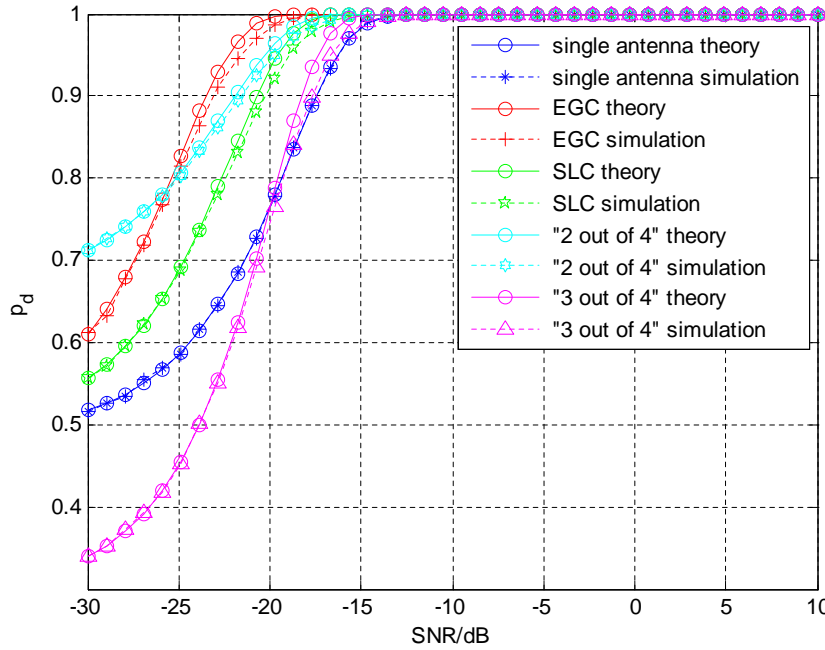


Figure 5.4: Detection probability of DA algorithm in multi-antenna scenario with different methods.

of spectrum sensing is moved to SU receiver from SU transmitter to increase the data transmission time and hence improve the throughput of SU; the data transmission time is adaptively adjusted to avoid the interference peculiar to unslotted CR network. Simulation results validate the efficiency of ICASST scheme, which significantly increases the throughput of secondary system and decreases the interference to PU simultaneously.

More details about the proposed scheme can be found in one of my papers, which is published in EURASIP Journal on Wireless Communications and Networking, 2012.

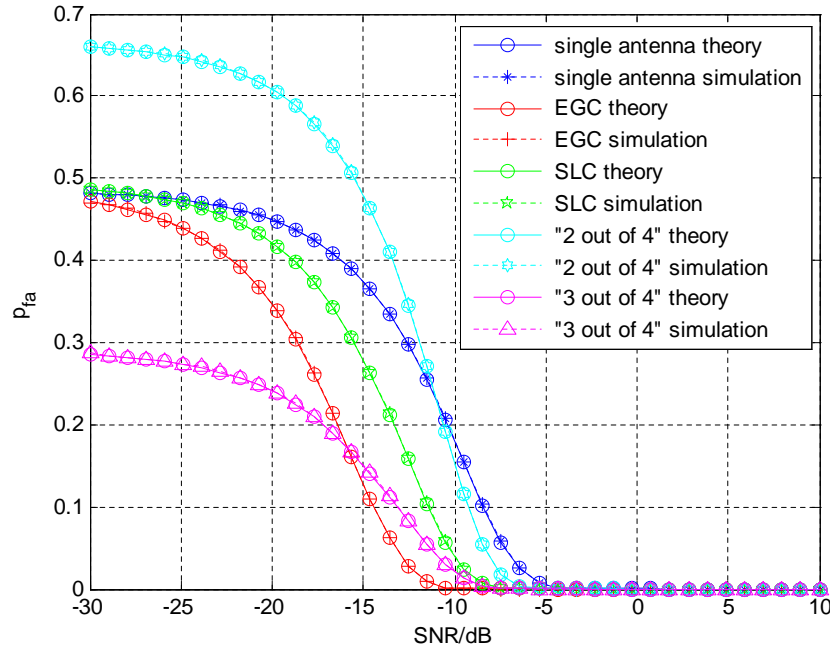


Figure 5.5: False alarm probability of DA algorithm in multi-antenna scenario with different methods.

5.4 CS Recovery Algorithms for Multi-antenna Signals

Since CS is initially designed for single antenna signals, how to recover the analog CS sampled multi-antenna signals is a new problem. Hence, this chapter designs two new CS recovery algorithms, i.e., CRL_2 algorithm and CBS algorithm, which are described in details as follows.

5.4.1 CRL_2 Algorithm

The function of the CRL_2 algorithm in the MCWSS scheme is illustrated in Figure 5.6, where the CRL_2 algorithm jointly processes the analog CS sampled multi-antenna signals and obtains the recovered multi-antenna signals simultaneously. Considering the multi-

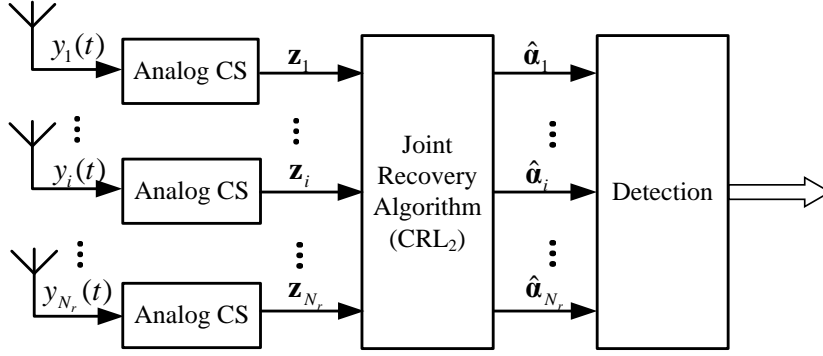


Figure 5.6: Description of CRL₂ algorithm.

antenna signals are jointly sparse, the CRL₂ algorithm firstly combines the multi-antenna signals' relevances with the L₂ norm to reduce the effect of noise, then it searches for the entry with the maximal relevance to identify the positions of the non-zero elements. The signal model and the principle are stated as follows.

The signal model is $\mathbf{z}_i = \mathbf{A}\boldsymbol{\theta} + \mathbf{w}_i$ for $i = 1, \dots, N_r$. $[\mathbf{a}_1 \dots \mathbf{a}_l \dots \mathbf{a}_n]$ are the columns of matrix \mathbf{A} with each column of unit norm; $\boldsymbol{\theta}$ is the sparse vector with only a few non-zero elements; \mathbf{z}_i is a linear combination of \mathbf{a}_l . The correlation coefficient vector between \mathbf{z}_i and \mathbf{a}_l for $l = 1, \dots, n$ is $\boldsymbol{\rho}_i = \mathbf{A}^H \mathbf{z}_i$. $\boldsymbol{\Lambda} = [\boldsymbol{\rho}_1 \dots \boldsymbol{\rho}_i \dots \boldsymbol{\rho}_{N_r}]$ is the $n \times N_r$ correlation matrix.

Then the recovery problem turns into how to combine the correlation matrix $\boldsymbol{\Lambda}$ into a $n \times 1$ vector $\boldsymbol{\rho}'$. Three commonly used methods are considered in the chapter: L₁ norm, L₂ norm, and L_∞ norm. Specifically, L₁ norm combining is $\rho'_l = \sum_{i=1}^{N_r} |\rho_{i,l}|$, where ρ'_l and $\rho_{i,l}$ are the element of $\boldsymbol{\rho}'$ and $\boldsymbol{\rho}_i$ respectively; L₂ norm combining is $\rho'_l = \sum_{i=1}^{N_r} |\rho_{i,l}|^2$; and L_∞ norm combining is $\rho'_l = \arg \max_{i=1, \dots, N_r} |\rho_{i,l}|$.

Since the relevance between noise and the measurement vector is smaller than that of signal, the method which can suppress the smaller element is the best. L₁ norm gives every element the same weight; L_∞ norm only selects the biggest component without restraining the smaller one; L₂ norm gives a greater weight to larger members and gives a smaller weight to smaller element. Thus, the CRL₂ algorithm chooses L₂ norm to suppress

Table 5.1: Procedures of CRL₂ algorithm

Input: \mathbf{A} , $\mathbf{z}_i, i = 1, \dots, N_r$, the number of non-zero elements d .
Output: Estimates $\hat{\boldsymbol{\theta}}_i, i = 1, \dots, N_r$ of the signal $\boldsymbol{\theta}$.
Procedures:
1. Initialize the residual $\mathbf{r}_{0,i} = \mathbf{z}_i$, the index set $I_0 = \emptyset$, the iteration counter $t = 1$, and chosen columns of matrix $\mathbf{A}_0 = \emptyset$.
2. Calculate the relevance $\boldsymbol{\rho}_i = \mathbf{A}^H \mathbf{r}_{t-1,i}$ for $i = 1, \dots, N_r$.
3. Combine relevance with L ₂ norm $\rho'_l = \sum_{i=1}^{N_r} \rho_{i,l} ^2$ for $l = 1, \dots, n$.
4. Find the index λ_t of the maximal element of $\boldsymbol{\rho}'$ by $\lambda_t = \arg \max_{l=1 \dots n} \rho'_l$.
5. Augment the index set $I_t = I_{t-1} \cup \{\lambda_t\}$, and the matrix of chosen columns $\mathbf{A}_t = [\mathbf{A}_{t-1} \mathbf{a}_{\lambda_t}]$, where \mathbf{a}_{λ_t} is the λ_t^{th} column of \mathbf{A} .
6. Update the residual by $\mathbf{r}_{t,i} = \mathbf{z}_i - \mathbf{A}_t(\mathbf{A}_t^H \mathbf{A}_t)^{-1} \mathbf{A}_t^H \mathbf{z}_i$ for $i = 1, \dots, N_r$.
7. Increment t , and return to step 2 if $t < 2d$.
8. The estimates $\hat{\boldsymbol{\theta}}_i$ have nonzero elements at the indices listed in I_{2d} , the value of $\hat{\boldsymbol{\theta}}_i$ in component λ_t is equal to the t^{th} component of $(\mathbf{A}_{2d}^H \mathbf{A}_{2d})^{-1} \mathbf{A}_{2d}^H \mathbf{z}_i$.

the noise. The procedures of the CRL₂ algorithm are shown in Table 5.1.

5.4.2 CBS Algorithm

Although the CRL₂ algorithm suppresses the noise by jointly processing the multi-antenna signals, the SNR does not increase directly, so the performance gain is limited. Considering EGC combining of the multi-antenna signals can increase the signal's SNR,

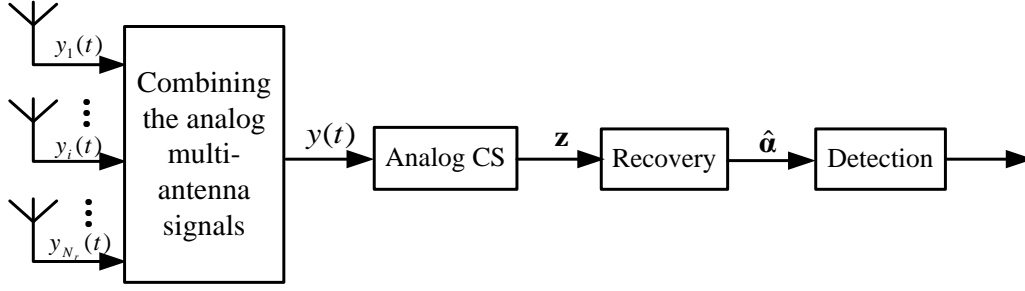


Figure 5.7: Block diagram of CBS algorithm.

we propose to combine the analog signals before analog CS, which is named as the CBS (combining before sampling) algorithm. The block diagram of the CBS algorithm is shown in Figure 5.7, where we can see that the multi-antenna signals are firstly combined before analog CS, and then are sampled by analog CS, at last the sampled signals are recovered and detected. To make the CBS algorithm clear, the detailed procedures is shown in Table 5.2.

5.4.3 Summary of CRL_2 Algorithm and CBS Algorithm

In this subsection, the CRL_2 algorithm and the CBS algorithm are compared from the angle of the denoising effect. The CRL_2 algorithm suppresses the noise by restraining the smaller relevance in the recovery process. The CBS algorithm increases the signal's SNR by combining the multi-antenna signals before analog CS. Hence, it can be speculated that the CBS algorithm outperforms the CRL_2 algorithm. However, compared with the CRL_2 algorithm, the CBS algorithm needs an additional analog device to combine the analog signals. In summary, one can choose CBS algorithm to get better performance if the analog combining operation is available, otherwise, CRL_2 algorithm is used to recover the multi-antenna signals.

Table 5.2: Procedures of CBS Algorithm

Input: The received analog signal from the j^{th} antenna $y_j(t)$, the sparsity of the signal d .

Output: Estimate of the combined signal $\hat{\boldsymbol{\theta}}$.

Procedures:

1. Combine the multi-antenna signals with EGC method into one signal by $y(t) = \sum_{j=1}^{N_r} y_j(t)/N_r$.
 2. Sample the combined signal $y(t)$ with MWC method and get $z(n)$.
 3. Get the signal model of recovery $\mathbf{z} = \mathbf{A}\boldsymbol{\theta}$.
 4. Initialize the residual $\mathbf{r}_0 = \mathbf{z}$, the index set $I_0 = \emptyset$, the iteration counter $t = 1$, and chosen columns of matrix $\mathbf{A}_0 = \emptyset$.
 5. Find the index by $\lambda_t = \arg \max_{l=1,\dots,n} |\langle \mathbf{r}_{t-1}, \mathbf{a}_l \rangle|$.
 6. Augment the index set $I_t = I_{t-1} \cup \{\lambda_t\}$, and the matrix of chosen columns $\mathbf{A}_t = [\mathbf{A}_{t-1} \ \mathbf{a}_{\lambda_t}]$, where \mathbf{a}_{λ_t} is the λ_t^{th} column of \mathbf{A} .
 7. Update the residual by $\mathbf{r}_t = \mathbf{z} - \mathbf{A}_t(\mathbf{A}_t^H \mathbf{A}_t)^{-1} \mathbf{A}_t^H \mathbf{z}$.
 8. Increment t , and return to step 2 if $t < 2d$.
 9. The estimate $\hat{\boldsymbol{\theta}}$ has nonzero elements at the indices listed in I_{2d} , the values of $\hat{\boldsymbol{\theta}}$ in component λ_t is equal to the t^{th} component of $(\mathbf{A}_{2d}^H \mathbf{A}_{2d})^{-1} \mathbf{A}_{2d}^H \mathbf{z}$.
-

5.5 Numerical Results

In this section, three main simulations are performed to evaluate the MCWSS scheme. The first simulation is performed to validate the theoretical derivation of the DA algorithm and the analysis results in the multi-antenna scenario. The relative simulation results are shown by the dotted lines in Figure 5.4 and Figure 5.5. The second simulation is performed

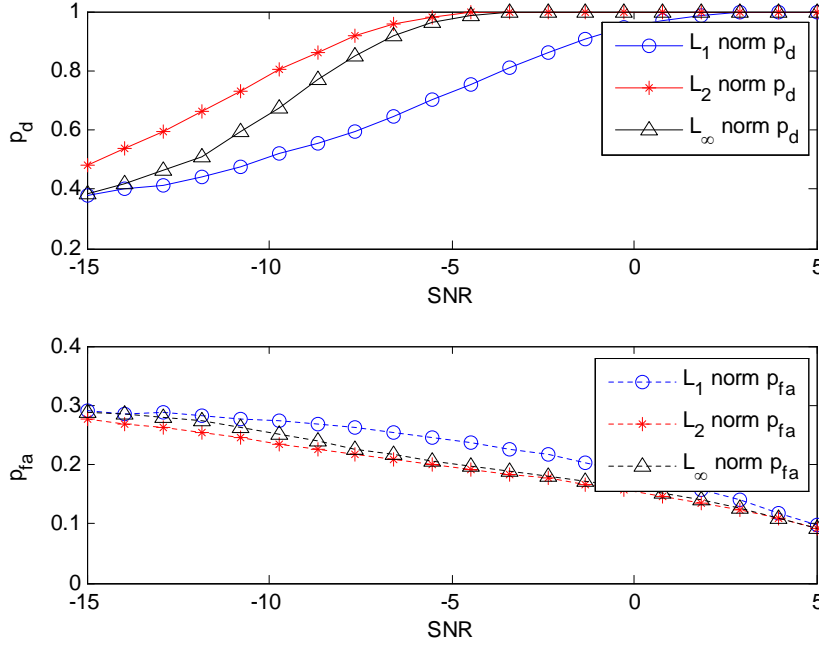


Figure 5.8: Performance of three joint processing methods: L_1 norm combining, L_2 norm combining, L_∞ norm combining.

to verify the CRL_2 algorithm, the relative simulation results are plotted in Figure 5.8. The third simulation is carried out to evaluate the performance of the CBS algorithm compared with the CRL_2 algorithm and the single antenna scenario, the simulation results are demonstrated in Figure 5.9 and Figure 5.10.

We consider a wideband signal that is divided into $J = 400$ non-overlapping equal-bandwidth sub-bands, with each sub-band containing $M = 82$ points. Suppose that the primary users randomly occupy some of the sub-bands, with an average spectrum occupancy ratio of 10%, that is to say, the sparsity of the wideband signal is $\mu = 0.1$. The wideband signal passes through the AWGN channel, and the CR user has $N_r = 4$ antennas in the multi-antenna scenario.

From Figure 5.4 and Figure 5.5, we can see that all the simulation results coincide with the theoretical values. Therefore, the theory derivations of the DA algorithm for both

the single antenna and the multi-antenna scenario are correct. The conclusion that the pre-combining method is better than the post-combining method for the multi-antenna scenario is validated.

Since the detection performance is our focus, we use p_d and p_{fa} as the performance metric in verifying the CRL_2 algorithm. In the simulation, the DA algorithm is used to detect the wideband signal. The simulation results of L_1 norm combining, L_2 norm combining and L_∞ norm combining are shown in Figure 5.8. It can be concluded from Figure 5.8 that L_2 norm combining is the best method to combine the relevance of different antenna's signals, that is to say, the CRL_2 algorithm is efficient.

When simulating the CBS algorithm, p_d and p_{fa} are also used as the performance metric. From Figure 5.9 and Figure 5.10, we can see that the CRL_2 algorithm performs better than the single antenna scenario; the CBS algorithm performs much better than the CRL_2 algorithm, and even the CBS algorithm with two antennas is better than the CRL_2 algorithm with four antennas. This is because that the CBS algorithm can increase the SNR of signal while the CRL_2 algorithm can not. In other words, the MCWSS can achieve excellent performance with the CBS algorithm and DA algorithm at a very low sampling rate, which can be reduced to about 28% of the Nyquist sampling rate.

It is worthwhile to note that, the introduction of analog CS degrades the performance of WSS, which can be concluded by comparing Figure 5.9 and Figure 5.10 with Figure 5.4 and Figure 5.5. The above performance degradation is caused by the noise in the sparse wideband signals. Thus, to make the application of CS into wireless communications more practical, the performance of the CS recovery algorithm must be improved.

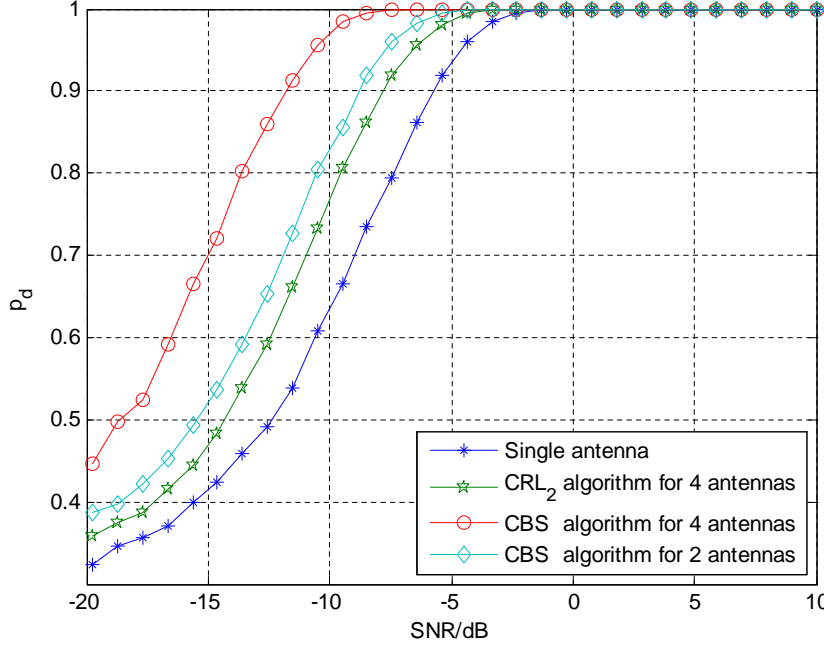


Figure 5.9: Detection probability of CRL₂ and CBS algorithm compared with single antenna scenario.

5.6 Summary

This chapter proposes a new WSS scheme (MCWSS scheme) to reduce the extremely high sampling rate problem and improve the detection performance in low SNR. We perform a thorough and complete work in the MCWSS scheme. Firstly, a new wideband detection algorithm, i.e., the DA algorithm, is devised to overcome the noise uncertainty with low complexity. The theoretical derivation and simulation results show the efficiency of the DA algorithm. Since previous studies on CS only focus on the single antenna scenario, two novel CS recovery algorithms, namely the CRL₂ algorithm and the CBS algorithm are designed for multi-antenna signals for different situations. In conclusion, the MCWSS scheme can achieve good detection performance with the proposed recovery and detection algorithms at a low sampling rate.

In this chapter, we found that the CS recovery performance is sensitive to noise, so we

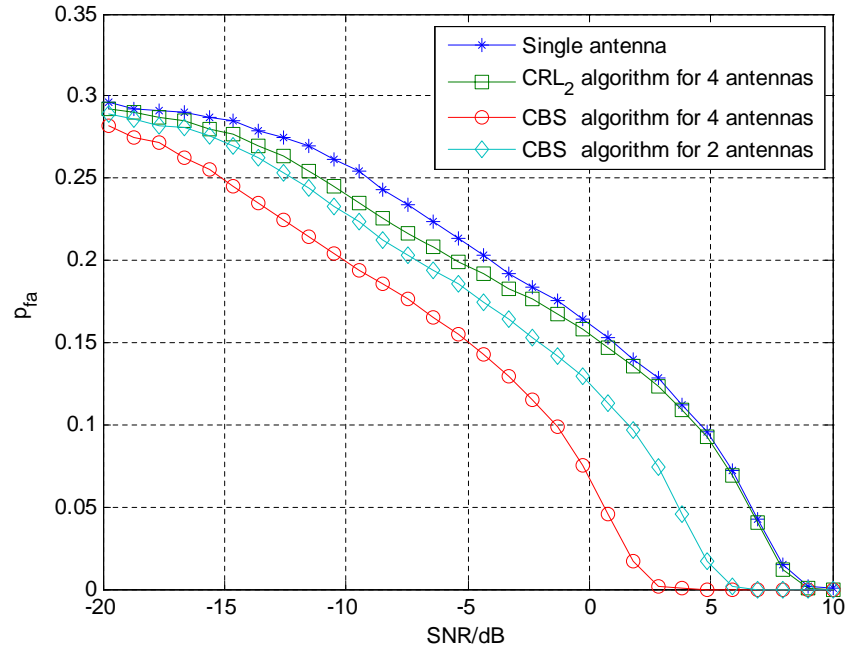


Figure 5.10: False alarm probability of CRL₂ and CBS algorithm compared with single antenna scenario.

will try to improve the CS recovery performance for noisy scenario in the next chapter.

Chapter 6

Denoising Regularized Subspace Pursuit CS Recovery Algorithm

As analyzed in Section 5.5, the CS recovery performance is sensitive to noise. However, noise is inevitable in wireless communication systems. To make the application of CS more practical, this chapter will investigate effective denoising CS recovery performance.

6.1 Introduction

The most common situation considered in a denoising CS recovery algorithm is that only the CS measurements are contaminated by noise, i.e.,

$$\mathbf{y} = \mathbf{A}\mathbf{x} + \mathbf{w}, \quad (6.1)$$

where \mathbf{x} is an $N \times 1$ unknown K -sparse signal, i.e., only K elements of \mathbf{x} are nonzero, where the indices of the K elements are termed the signal support Λ of \mathbf{x} , \mathbf{A} is an $M \times N$ Gaussian or Bernoulli distributed measurement matrix, which satisfies the RIP [20], \mathbf{y} is an $M \times 1$ measurement vector, and \mathbf{w} is an $M \times 1$ Gaussian white noise vector with mean 0 and variance σ^2 .

However, in many practical scenarios, e.g., the application of CS in the design of sub-Nyquist sampling devices [1] [2], the sparse signal is contaminated by noise prior to measurement. Thus, in this chapter, we will consider the following more general signal model

$$\mathbf{y} = \mathbf{A}(\mathbf{x} + \mathbf{z}) + \mathbf{w} = \mathbf{A}\mathbf{x} + \mathbf{v}, \quad (6.2)$$

where $\mathbf{v} = \mathbf{A}\mathbf{z} + \mathbf{w}$, and \mathbf{z} is an $N \times 1$ Gaussian white noise vector, where each element has mean 0 and variance σ_z^2 , and we assume that $\sigma_w^2 = \sigma_z^2 = \sigma^2$ for simplicity. It is worth mentioning that the pre-measurement noise \mathbf{z} results in much larger noise power in the compressive measurements \mathbf{y} than that in the original noisy sparse signal, which is called the noise-folding effect [37]. The reason for the noise-folding effect is that the measurement matrix \mathbf{A} combines all the noise elements in \mathbf{z} , even those corresponding to the zero elements in \mathbf{x} .

Reliable and stable CS recovery algorithms are one of the key components of the CS theory and are very important for the application of CS in noisy scenarios. Thus, in this chapter, we aim to develop an efficient CS denoising algorithm to reconstruct the noise-contaminated sparse signals from noisy compressive measurements with a high successful recovery rate. Since greedy algorithms are much faster and easier to implement than regularization methods, this paper focuses on the improvements of greedy algorithms in noisy environments. As stated in Section 2.1.4, the existing denoising greedy algorithms improve OMP either from the angle of finding indices of nonzero elements, e.g., ROMP, or the angle of signal estimation, e.g., CoSaMP and SP. However, none of them improves OMP from both angles.

Thus, this chapter proposes a RSP algorithm to improve OMP from both aspects mentioned above simultaneously. Firstly, the proposed RSP algorithm alleviates the noise-folding effect by introducing a data pre-processing operation. Secondly, the signal support Λ is identified by regularizing the chosen columns of \mathbf{A} , and then the chosen indices are

updated by retaining only the largest entries of the estimated signal. Thirdly, instead of using the LS method, Minimum Mean Square Error (MMSE) estimation is adopted to further reduce the effect of noise.

Simulation results show that, compared with the existing OMP, ROMP, CoSaMP and SP algorithms, the proposed RSP algorithm has the highest successful recovery rate and the smallest reconstruction error when the noise variance is high and the number of measurements is not large enough. For example, compared with the OMP algorithm, the proposed RSP algorithm increases the successful recovery rate (reduces the normalized reconstruction error) by up to 50% and 86% (35% and 65%) in high noise level scenarios and inadequate measurements scenarios, respectively.

The rest of this chapter is organized as follows. Section 6.2 describes the proposed RSP algorithm. Section 6.3 evaluates the recovery performance of RSP in comparison with the existing OMP, ROMP, CoSaMP and SP algorithms. Finally, Section 6.4 concludes this chapter.

6.2 Proposed RSP Algorithm

Based on the traditional OMP algorithm and motivated by the ROMP and SP algorithms, we propose the RSP algorithm to combat the effects of both the pre-measurement noise \mathbf{z} and the measurement noise \mathbf{w} .

6.2.1 Basic Idea

Five key parts of the RSP algorithm are stated as follows.

Pre-processing Operation

The covariance matrix of the equivalent noise vector \mathbf{v} in (6.2) is expressed as

$$\mathbf{Q} = \sigma^2(\mathbf{I} + \mathbf{A}\mathbf{A}^T). \quad (6.3)$$

Thus, the equivalent noise \mathbf{v} is not white any more unless the matrix $\mathbf{A}\mathbf{A}^T$ is proportional to the identity matrix \mathbf{I} . One example of the above exception is that matrix \mathbf{A} is a concatenation of $p = \frac{N}{M}$ orthonormal matrices, i.e., $\mathbf{A} = [\mathbf{A}^{(1)}, \dots, \mathbf{A}^{(p)}]$, where the dimension of $\mathbf{A}^{(k)}$ is $M \times M$. Then, we have $\mathbf{A}\mathbf{A}^T = p\mathbf{I}$, and $\mathbf{Q} = (1 + \frac{N}{M})\sigma^2\mathbf{I}$. This is a special case of the noise-folding effect, where the variance of the equivalent additive white noise is increased $\frac{N}{M}$ times.

In the proposed RSP algorithm, to better reconstruct the sparse signal, the noise \mathbf{v} is whitened by multiplying $\mathbf{Q}^{-1/2}$ at both sides of (6.2), then we obtain

$$\tilde{\mathbf{y}} = \mathbf{B}\mathbf{x} + \mathbf{v}', \quad (6.4)$$

where $\tilde{\mathbf{y}} = \mathbf{Q}^{-1/2}\mathbf{y}$, $\mathbf{B} = \mathbf{Q}^{-1/2}\mathbf{A}$ and $\mathbf{v}' = \mathbf{Q}^{-1/2}\mathbf{v}$. Now, the new equivalent noise \mathbf{v}' is white and has variance σ^2 .

Scaled Relevance Vector

Let \mathbf{b}_j denote the j^{th} column of the new measurement matrix \mathbf{B} , and $\|\mathbf{b}_j\|_2$ represent the ℓ_2 norm of \mathbf{b}_j . To make sure that the differences among $\|\mathbf{b}_j\|_2$ do not affect the precision in finding the index with the biggest relevance from the relevance vector $\mathbf{B}^H\mathbf{r}_{t-1}$, we propose to adopt the scaled relevance vector \mathbf{u}_t , which is expressed as

$$\mathbf{u}_t = \mathbf{C}^H\mathbf{r}_t, \quad (6.5)$$

where $\mathbf{C} = \mathbf{B}/\sqrt{\text{diag}(\mathbf{B}^H\mathbf{B})}$.

Identifying the Indices by Regularization

According to the RIP property [4], every K columns of matrix \mathbf{B} constitute an approximate orthonormal matrix. At the t^{th} iteration, to make the identified columns of \mathbf{B} behave like an orthonormal matrix, the identified columns are regularized via choosing a subset J_0 of the K largest indices in \mathbf{u}_t by letting

$$J_0 = \{j \mid \mathbf{u}_t(j) \geq u_{t,\max}/2\}, \quad (6.6)$$

where $\mathbf{u}_t(j)$ is the j^{th} element of \mathbf{u}_t , and $u_{t,\max} = \max_j[\mathbf{u}_t(j)]$ is the maximum element of \mathbf{u}_t . Then, the set J_0 is augmented to the identified indices in the previous iteration by letting $\Lambda_t = \Lambda_{t-1} \cup \{J_0\}$.

Estimating the Signal with MMSE

Since the LS method used in the existing greedy algorithms amplifies the noise, we utilize the denoising MMSE method to estimate the signal \mathbf{x}_{Λ_t} from the following problem

$$\tilde{\mathbf{y}} = \mathbf{B}_{\Lambda_t} \mathbf{x}_{\Lambda_t} + \mathbf{v}', \quad (6.7)$$

where \mathbf{x}_{Λ_t} contains the elements of \mathbf{x} indexed by Λ_t . As we know, the MMSE method requires to know the power of \mathbf{x}_{Λ_t} , which varies with the change of Λ_t . Thus, we propose to estimate the power of \mathbf{x}_{Λ_t} with the LS method, i.e.,

$$P = \left(\mathbf{B}_{\Lambda_t}^\dagger \tilde{\mathbf{y}} \right)^H \left(\mathbf{B}_{\Lambda_t}^\dagger \tilde{\mathbf{y}} \right) / |\Lambda_t|, \quad (6.8)$$

where $|\Lambda_t|$ is the cardinality of set Λ_t and counts the number of its elements. Then, the MMSE estimated signal is

$$\hat{\mathbf{x}}_{\Lambda_t} = \left(\mathbf{B}_{\Lambda_t}^H \mathbf{B}_{\Lambda_t} + \frac{\sigma^2}{P} \mathbf{I} \right)^{-1} \mathbf{B}_{\Lambda_t}^H \tilde{\mathbf{y}}. \quad (6.9)$$

Updating the Indices

If there are more than K elements in the identified indices set Λ_t , we propose to update Λ_t by only retaining the K largest entries in the magnitude of $\hat{\mathbf{x}}_{\Lambda_t}$.

Finally, the iterations will stop if the number of iterations is larger than K , or if the norm of the residual in this iteration is larger than that in the last one, i.e., $\|\mathbf{r}_t\|_2 \geq \|\mathbf{r}_{t-1}\|_2$.

6.2.2 Pseudocode of Proposed RSP Algorithm

Table 6.1 shows the procedures of the RSP algorithm.

Table 6.1: Pseudocode of Proposed RSP Algorithm

INPUT: \mathbf{A} , \mathbf{y} , K , σ^2 .

DATA PRE-PROCESSING OPERATION:

$$\mathbf{Q} = \sigma^2(\mathbf{I} + \mathbf{A}\mathbf{A}^T); \quad \tilde{\mathbf{y}} = \mathbf{Q}^{-1/2}\mathbf{y}; \quad \mathbf{B} = \mathbf{Q}^{-1/2}\mathbf{A};$$

INITIALIZATION:

1) Set the index set $\Lambda_0 = \emptyset$, the residual $\mathbf{r}_0 = \tilde{\mathbf{y}}$, the iteration count $t=1$.

3) Initialize the norm of the residual: $\mathbf{n}_r(0) = \infty$ and $\mathbf{n}_r(1) = \sqrt{\mathbf{r}_0^H \mathbf{r}_0}$.

ITERATIONS:

WHILE ($t \leq K$) & ($\mathbf{n}_r(t) < \mathbf{n}_r(t-1)$)

$\mathbf{u}_t = \mathbf{C}^H \mathbf{r}_t$, where $\mathbf{C} = \mathbf{B} / \sqrt{\text{diag}(\mathbf{B}^H \mathbf{B})}$; % Calculate the scaled relevance vector.

$[\mathbf{u}_{t,s}, J] = \text{sort}(|\mathbf{u}_t|, \text{'descend'})$; $k=1$; % Identify the indices by regularization.

WHILE ($k \leq K$) & ($|\mathbf{u}_{t,s}(k)| \geq |\mathbf{u}_{t,s}(1)|/2$); $k=k+1$; **END WHILE**

$J_0 = J(1 : k-1)$; % Obtaining the first $k-1$ elements of J .

$\Lambda_t = \Lambda_{t-1} \cup J_0$; % Estimate the signal with MMSE method.

$$P = \left(\mathbf{B}_{\Lambda_t}^\dagger \tilde{\mathbf{y}} \right)^H \left(\mathbf{B}_{\Lambda_t}^\dagger \tilde{\mathbf{y}} \right) / |\Lambda_t|; \quad \hat{\mathbf{x}}_{\Lambda_t} = \left(\mathbf{B}_{\Lambda_t}^H \mathbf{B}_{\Lambda_t} + \frac{\sigma^2}{P} \mathbf{I} \right)^{-1} \mathbf{B}_{\Lambda_t}^H \tilde{\mathbf{y}}; \quad \mathbf{r}_t = \tilde{\mathbf{y}} - \mathbf{B}_{\Lambda_t} \hat{\mathbf{x}}_{\Lambda_t};$$

% Update the indices by retaining only the K largest elements.

```

IF  $|\Lambda_t| > K$ 
     $\hat{\mathbf{x}}_t = \begin{cases} \hat{\mathbf{x}}_{\Lambda_t}, & \text{on the support set } \Lambda_t \\ \mathbf{0}, & \text{elsewhere} \end{cases};$ 
     $[\hat{\mathbf{x}}_s, J_s] = \text{sort}(|\hat{\mathbf{x}}_t|, \text{'descend'}); \Lambda_t = J_s(1 : K);$ 
    % Estimate the signal with the updated indices.
     $P = \left( \mathbf{B}_{\Lambda_t}^\dagger \tilde{\mathbf{y}} \right)^H \left( \mathbf{B}_{\Lambda_t}^\dagger \tilde{\mathbf{y}} \right) / |\Lambda_t|; \hat{\mathbf{x}}_{\Lambda_t} = \left( \mathbf{B}_{\Lambda_t}^H \mathbf{B}_{\Lambda_t} + \frac{\sigma^2}{P} \mathbf{I} \right)^{-1} \mathbf{B}_{\Lambda_t}^H \tilde{\mathbf{y}}; \mathbf{r}_t = \tilde{\mathbf{y}} - \mathbf{B}_{\Lambda_t} \hat{\mathbf{x}}_{\Lambda_t};$ 
ELSE Continue;
END IF  $\mathbf{n}_r(t+1) = \sqrt{\mathbf{r}_t^H \mathbf{r}_t}; t = t+1;$ 
END WHILE

OUTPUT:
The estimated signal  $\hat{\mathbf{x}} = \hat{\mathbf{x}}_t = \begin{cases} \hat{\mathbf{x}}_{\Lambda_t}, & \text{on the support set } \Lambda_t \\ \mathbf{0}, & \text{elsewhere} \end{cases}$ , and the reconstructed
signal support  $\hat{\Lambda} = \Lambda_t$ .

```

6.3 Performance Evaluation

6.3.1 Simulation Parameters and Performance Metrics

In the simulations, we assume that \mathbf{x} is a 10-sparse 256×1 signal. The amplitudes of the nonzero elements in \mathbf{x} are uniformly distributed random variables in interval $[c, d]$, with $c=0.4$ and $d=1$. Then, the power of \mathbf{x} is normalized. The elements a_{ij} of the $M \times N$ measurement matrix \mathbf{A} are i.i.d. Gaussian variables with $a_{ij} \sim \mathcal{N}(0, 1/M)$. Therefore, each column of \mathbf{A} has unit norm on average.

All the simulations are performed with MATLAB and each simulation result is obtained via 2×10^4 random tests. The performance of the proposed RSP algorithm is evaluated by comparing it with the exiting OMP, ROMP, CoSaMP and SP algo-

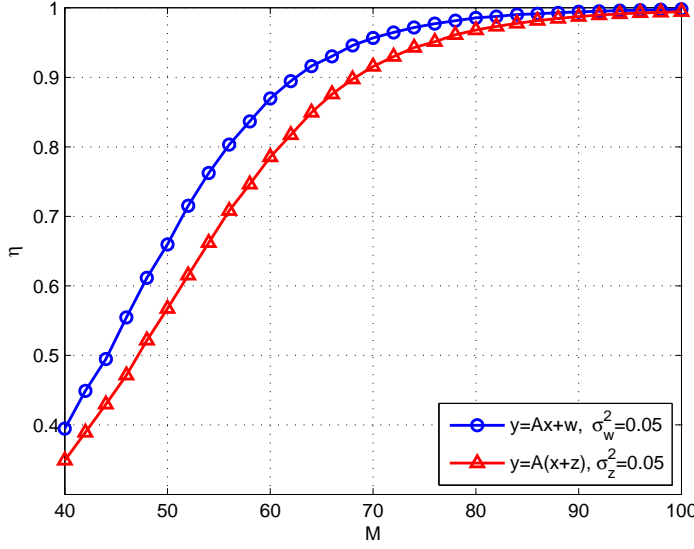


Figure 6.1: Illustration of the noise-folding effect, the successful recovery rate η vs. the number of measurements M .

rithms. The codes for OMP, ROMP, CoSaMP and SP are downloaded from the websites [110], [111], [112] and [113], respectively. The following two performance metrics are adopted: the first one is the successful recovery rate defined by $\eta = |\hat{\Lambda} \cap \Lambda| / |\Lambda|$ where $\hat{\Lambda}$ is the estimated signal support, the second performance metric is the normalized reconstruction error $\varepsilon = \|\mathbf{x} - \hat{\mathbf{x}}\|_2 / \|\mathbf{x}\|_2$.

6.3.2 Illustration of Noise-folding Effect

In this section, the noise-folding effect is demonstrated by comparing the recovery performance of the following two scenarios, i.e., $\mathbf{y} = \mathbf{A}(\mathbf{x} + \mathbf{z})$ and $\mathbf{y} = \mathbf{A}\mathbf{x} + \mathbf{w}$, where $\sigma_z^2 = \sigma_w^2 = 0.05$. Thus, we have $\text{SNR} = 13\text{dB}$ for $\mathbf{y} = \mathbf{A}\mathbf{x} + \mathbf{w}$, and $\text{SNR} \approx 10 \lg \frac{M}{12.8} \text{dB}$ for $\mathbf{y} = \mathbf{A}(\mathbf{x} + \mathbf{z})$. Figure 6.1 and Figure 6.2 show that, due to the noise-folding effect, the recovery performance of $\mathbf{y} = \mathbf{A}(\mathbf{x} + \mathbf{z})$ is degraded compared with that of $\mathbf{y} = \mathbf{A}\mathbf{x} + \mathbf{w}$. Specifically, Figure 6.1 indicates that the successful recovery rate of $\mathbf{y} = \mathbf{A}(\mathbf{x} + \mathbf{z})$ is decreased by up to 17% in comparison with that of $\mathbf{y} = \mathbf{A}\mathbf{x} + \mathbf{w}$. Besides, Figure 6.2 illus-

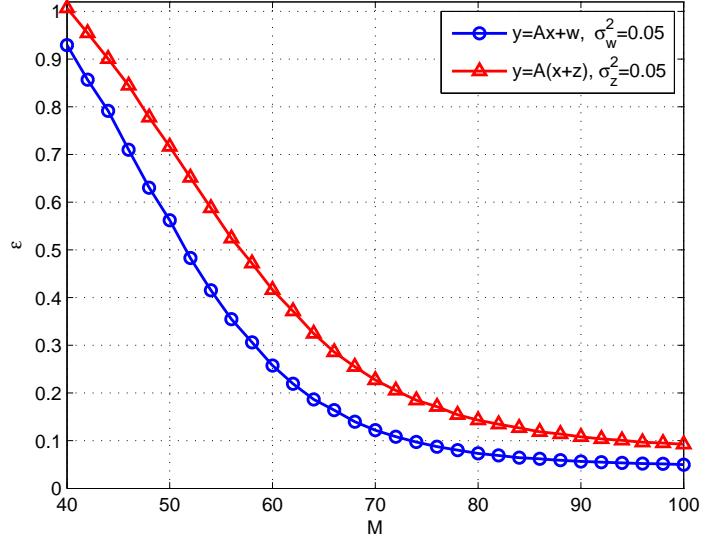


Figure 6.2: Illustration of the noise-folding effect, the normalized reconstruction error ε vs. the number of measurements M .

trates that the reconstruction error of $\mathbf{y} = \mathbf{A}(\mathbf{x} + \mathbf{z})$ is increased by up to 48% compared with that of $\mathbf{y} = \mathbf{A}\mathbf{x} + \mathbf{w}$.

6.3.3 Simulation Results under Signal Model $\mathbf{y} = \mathbf{A}(\mathbf{x} + \mathbf{z}) + \mathbf{w}$

In this section, we evaluate the proposed RSP algorithm under signal model $\mathbf{y} = \mathbf{A}(\mathbf{x} + \mathbf{z}) + \mathbf{w}$. The performance of the RSP algorithm and the existing four schemes are evaluated against the number of measurements M and SNR, which is approximated as $\text{SNR} \approx 10 \lg^{1/(1+\frac{N}{M}\sigma^2)}$.

The recovery performance vs. M

Figure 6.3 illustrates that, in comparison with the OMP, ROMP, CoSaMP and SP algorithms, the proposed RSP algorithm has the highest successful recovery rate η with the number of measurements M increasing from 40 to 100, when $\sigma^2 = 0.05$ and $\text{SNR} \approx 10 \lg^{1/(1+\frac{12.8}{M})}$ dB. Specifically, RSP increases η by up to 86%, 27%, 48% and 40% compared with OMP, ROMP, CoSaMP and SP algorithm, respectively. Figure 6.4 shows that,

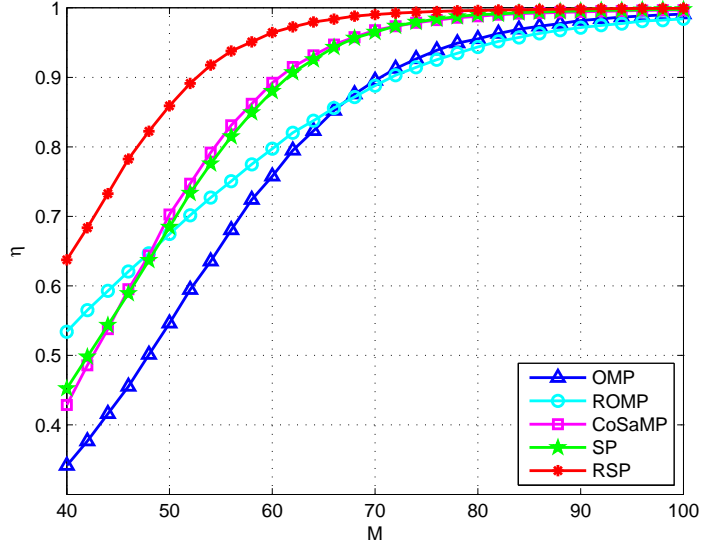


Figure 6.3: Successful recovery rate η vs. the number of measurements M , when $\mathbf{y}=\mathbf{A}(\mathbf{x} + \mathbf{z}) + \mathbf{w}$, $\sigma^2=0.05$ and $\text{SNR} \approx 10\lg^{1/(1+\frac{12.8}{M})}\text{dB}$.

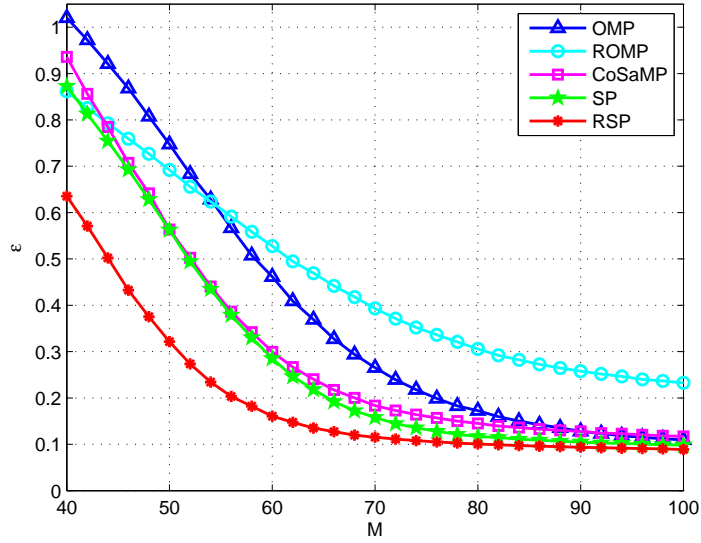


Figure 6.4: Normalized reconstruction error ε vs. the number of measurements M , when $\mathbf{y}=\mathbf{A}(\mathbf{x} + \mathbf{z}) + \mathbf{w}$, $\sigma^2=0.05$ and $\text{SNR} \approx 10\lg^{1/(1+\frac{12.8}{M})}\text{dB}$.

compared with the existing four algorithms, the proposed RSP algorithm has the smallest normalized reconstruction error ε with the increase of M . Specifically, the RSP algorithm

decreases ε by up to 65%, 71%, 47%, and 46% compared with the OMP, ROMP, CoSaMP and SP, respectively.

Besides, Figure 6.3 and Figure 6.4 demonstrate that, compared with the OMP algorithm, ROMP can improve the recovery performance when M is relatively small, but it deteriorates the recovery performance when M is larger, which is not desired. The reason for this phenomenon is that ROMP identifies $2K$ nonzero elements including at most K correct indices and at least K wrong indices, where the wrong indices deteriorate the recovery performance especially when M is large.

The recovery performance vs. SNR

Figure 6.5 indicates that, the proposed RSP algorithm has the highest recovery rate η in comparison with the existing four algorithms. Specifically, with the increase of SNR, the proposed RSP algorithm increases η by up to 50%, 4%, 36% and 34% compared with OMP, ROMP, CoSaMP and SP algorithms, respectively. Figure 6.6 shows that the proposed RSP algorithm has the smallest reconstruction error ε . Specifically, RSP decreases ε by up to 35%, 70%, 30% and 24% with the increase of SNR compared with the OMP, ROMP, CoSaMP and SP, respectively.

6.3.4 Simulation Results under Signal Model $\mathbf{y}=\mathbf{Ax} + \mathbf{w}$

In this section, we investigate the performance of the proposed RSP algorithm under signal model $\mathbf{y}=\mathbf{Ax} + \mathbf{w}$, where SNR is defined as $\text{SNR} = 10 \lg^{1/\sigma^2}$.

The recovery performance vs. M

Figure 6.7 illustrates that, under signal model $\mathbf{y}=\mathbf{Ax} + \mathbf{w}$, the proposed ROMP algorithm has the highest successful recovery rate η . Specifically, RSP increases η by up to 85%, 30%, 39% and 37% compared with the OMP, ROMP, CoSaMP and SP algorithm,

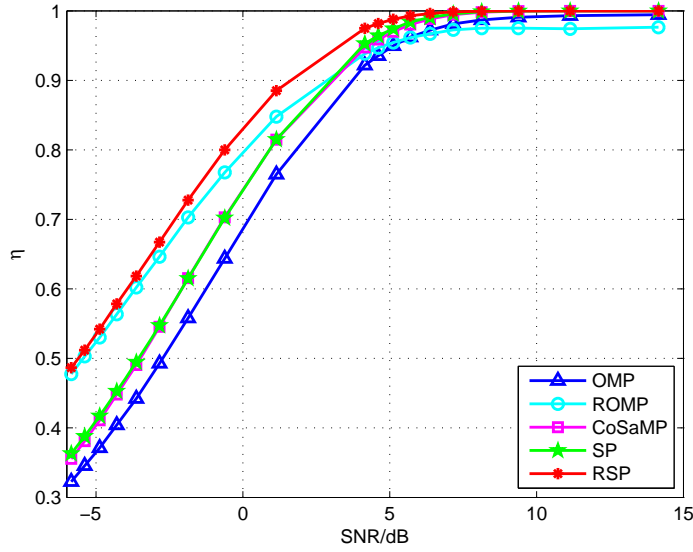


Figure 6.5: Successful recovery rate η vs. $\text{SNR} \approx 10 \lg^{1/(1+\frac{256}{90}\sigma^2)}$, when $\mathbf{y}=\mathbf{A}(\mathbf{x} + \mathbf{z}) + \mathbf{w}$ and $M=90$.

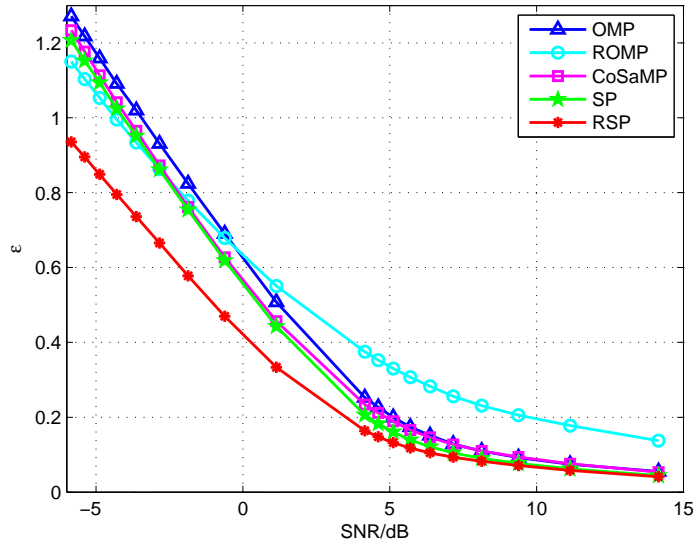


Figure 6.6: Normalized reconstruction error ε vs. $\text{SNR} \approx 10 \lg^{1/(1+\frac{256}{90}\sigma^2)}$, when $\mathbf{y}=\mathbf{A}(\mathbf{x} + \mathbf{z}) + \mathbf{w}$ and $M=90$.

respectively. Figure 6.8 shows that, the proposed RSP algorithm has the smallest normalized reconstruction error ε . Specifically, the RSP algorithm decreases ε by up to 75%,

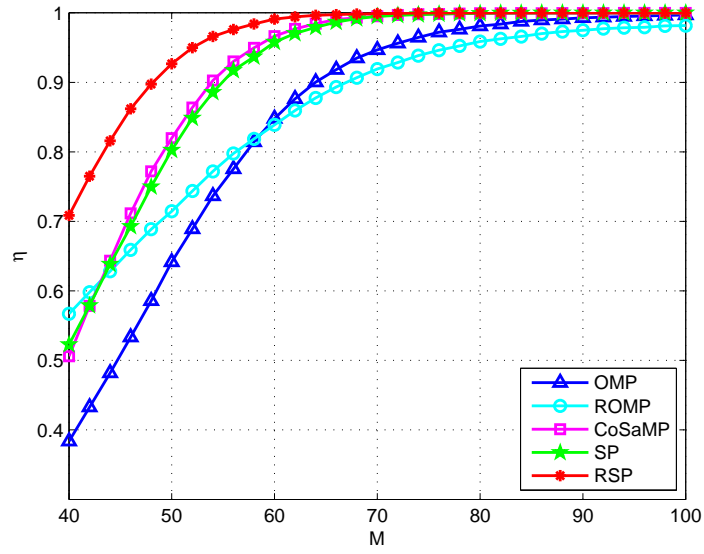


Figure 6.7: Successful recovery rate η vs. the number of measurements M , when $\mathbf{y}=\mathbf{Ax} + \mathbf{w}$ and SNR=10dB.

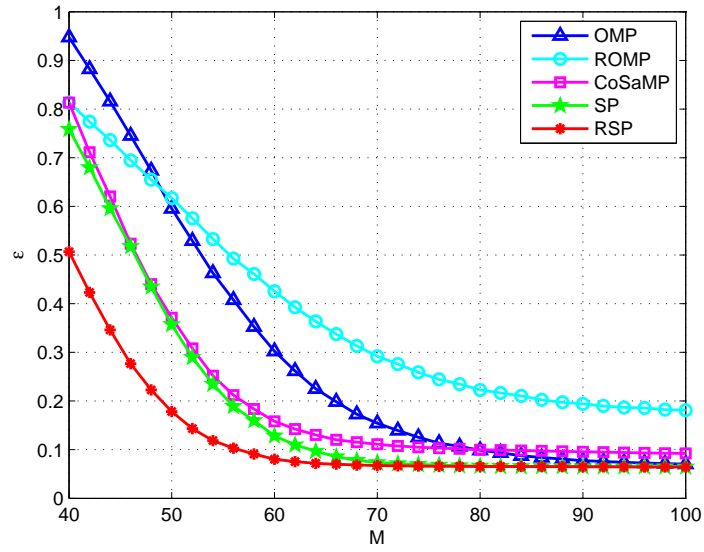


Figure 6.8: Normalized reconstruction error ε vs. the number of measurements M , when $\mathbf{y}=\mathbf{Ax} + \mathbf{w}$ and SNR=10dB.

81%, 51%, and 50% compared with the OMP, ROMP, CoSaMP and SP, respectively.

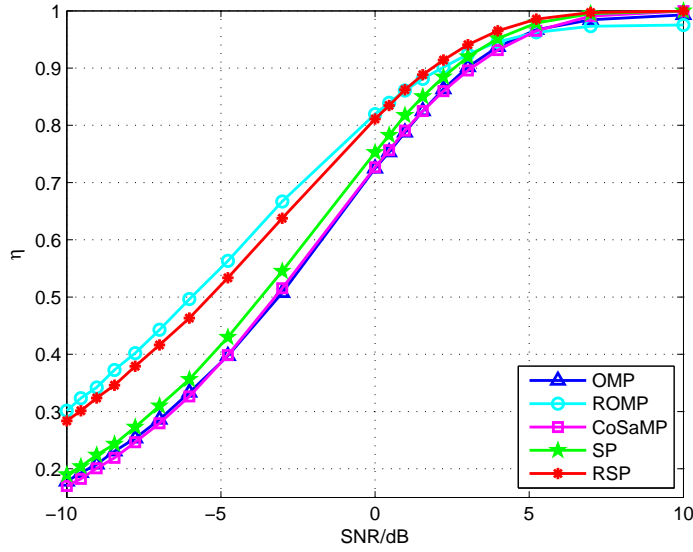


Figure 6.9: Successful recovery rate η vs. SNR, when $\mathbf{y}=\mathbf{Ax} + \mathbf{w}$ and $M=90$.

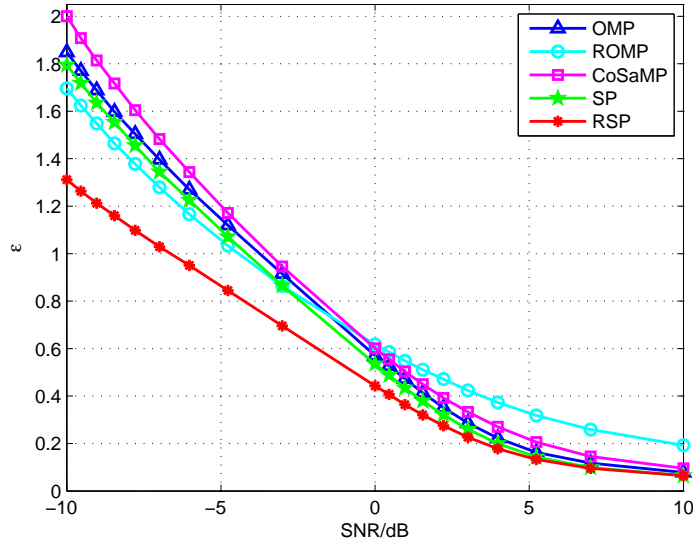


Figure 6.10: Normalized reconstruction error ε vs. SNR, when $\mathbf{y}=\mathbf{Ax} + \mathbf{w}$ and $M=90$.

The recovery performance vs. SNR

Figure 6.9 indicates that, the proposed RSP algorithm has the highest recovery rate η when $0\text{dB} < \text{SNR} < 10\text{dB}$, and has the second highest η when $-10\text{dB} < \text{SNR} < 0\text{dB}$. Specif-

ically, with the increase of SNR, the proposed RSP algorithm increases η by up to 57%, 47% and 50% compared with the OMP, CoSaMP and SP algorithms, respectively. Figure 6.10 shows that the proposed RSP algorithm has the smallest reconstruction error ε . Specifically, RSP decreases ε by up to 30%, 74%, 26% and 29% with the increase of SNR compared with the OMP, ROMP, CoSaMP and SP, respectively. It is worthy to note that, although the successful recovery rate η of RSP is smaller (up to 6%) than ROMP when $-10\text{dB} < \text{SNR} < 0\text{dB}$, it has smaller (up to 74%) reconstruction error ε than ROMP.

In summary, under signal model $\mathbf{y}=\mathbf{A}(\mathbf{x}+\mathbf{z})+\mathbf{w}$, the proposed RSP algorithm can simultaneously improve the successful recovery rate η and decrease the reconstruction error ε for all values of M and σ^2 . Under signal model $\mathbf{y}=\mathbf{A}\mathbf{x}+\mathbf{w}$, the proposed RSP algorithm has the lowest reconstruction error and the second highest successful recovery rate. The basic idea of the proposed RSP algorithm is to improve the way of identifying the indices of the nonzero elements and the method of estimating the signal with not more than K nonzero elements, simultaneously.

6.4 Summary

To enhance the performance of CS recovery algorithms in the scenarios where both the original sparse signal and the CS measurement vector are contaminated by noise, this chapter proposed a RSP algorithm by simultaneously improving the way of identifying the signal support and the method of estimating signals with the updated signal support. Meanwhile, by introducing a data pre-processing operation, the proposed RSP algorithm reduces the noise-folding effect. Simulation results show that, under signal model $\mathbf{y}=\mathbf{A}(\mathbf{x}+\mathbf{z})+\mathbf{w}$, the proposed RSP algorithm has the highest successful recovery rate and the lowest reconstruction error in comparison with the existing OMP, ROMP, CoSaMP and SP algorithms. Under signal model $\mathbf{y}=\mathbf{A}\mathbf{x}+\mathbf{w}$, the proposed RSP al-

gorithm has the lowest reconstruction error and the second highest successful recovery rate, which is lower (up to 6%) than ROMP. However, RSP has smaller (up to 74%) reconstruction error ε than ROMP.

Chapter 7

Conclusions and Future Work

This thesis focuses on the application of discrete CS in improving the energy efficiency of WSNs, the research on analog CS based on a structured matrix, the application of analog CS in wideband spectrum sensing for CRs, and the design of a denoising CS recovery algorithm. In this chapter, we will summarize the innovations of this thesis in Section 7.1, then we will point out the directions for future work in Section 7.2.

7.1 Innovations in the Thesis

The main innovations of this thesis are presented as follows.

7.1.1 CNCDS Scheme

Utilizing the correlations of wireless sensor data, we propose a CNCDS scheme based on the CS theory and network coding technology. The objective of the CNCDS scheme is to improve the energy efficiency of WSNs deployed in catastrophic scenarios by simultaneously reducing the number of required transmissions and receptions. Theoretical analysis proves that the measurement matrix of the CNCDS scheme guarantees successful recovery of the sensed data. To verify the efficiency of the CNCDS scheme, we derive

the expressions for the total number of data transmissions and receptions based on the random geometric graph theory. Furthermore, based on the derived expressions, we propose an adaptive CNCDS scheme, which further improves the energy efficiency of WSNs. Simulation results show that, the proposed adaptive CNCDS scheme has the highest energy efficiency with the lowest reconstruction error. The related research work won the “Best Paper Award” of ISCIT 2012 and is published in IEEE Transactions on Wireless Communications, 2013.

7.1.2 Research on Analog CS Based on Structured Matrix

The main innovations and achievements in this topic are stated as follows.

(1) Using non-modulated Slepian basis to represent the modulated and bandlimited multi-band signal, we significantly reduce the dimensions of the signal basis and measurement matrix, and thus reduce the computational recovery complexity. To obtain the performance gain of the Slepian basis, we further propose an interpolation recovery algorithm. Simulation results show that, compared with the DFT basis, our proposed algorithm can improve the recovery SNR up to 35dB at a low computational load. The related research work is published in IEEE ICC, 2013.

(2) Based on the random circulant orthogonal matrix, we propose using the cyclic shifts of the ZC sequence to replace the independent pseudorandom sequences. As a result, we reduce the number of physical parallel channels from m to 1, where m ranges from several dozens to several hundreds. Theoretical analysis proves that the measurement matrix of the proposed scheme satisfies the RIP condition. The related research work is published on IET Electronics Letter 2012, and IEEE GLOBECOM 2012.

7.1.3 MCWSS Scheme

Since analog CS enables Sub-Nyquist rate sampling for sparse signals, it resolves the extremely high sampling rate challenge confronted by WSS in CRs. However, CS may compromise the detection performance of WSS, because CS is sensitive to noise. Here, we propose utilizing multi-antenna technology to improve the detection performance. Furthermore, we design a joint recovery algorithm for multi-antenna signals by utilizing their joint sparsity. To alleviate the effect of noise uncertainty, we propose a low-complexity and high-performance WSS algorithm. Simulation results show that, the proposed MCWSS scheme has high detection performance at about 28% of Nyquist sampling rate. The related research work is published in IEEE WCNC, 2011.

In addition, there is one contradiction in CRs, i.e., to simultaneously minimize the interference caused to the primary (licensed) system, and maximize the throughput of the secondary (unlicensed) system. To resolve the above challenge, we propose an interference-constrained adaptive simultaneous spectrum sensing and data transmission scheme, which is published in EURASIP Journal on Wireless Communications and Networking, 2012.

7.1.4 CS Denoising Recovery Algorithm – Regularized Subspace Pursuit

To improve the recovery performance of CS in noisy environments, we propose a novel CS denoising recovery algorithm, i.e., the RSP algorithm. The RSP algorithm is designed for the scenario, where both the sparse signals and measurements are contaminated by noise. By adding a pre-processing operation and using the MMSE method to estimate the sparse signal, we alleviate the noise folding effect caused by the noise in sparse signals. Via regularizing the chosen columns in the iteration, we make the chosen columns approximately satisfy the RIP condition. Simulation results show that, compared with existing

CS denoising recovery algorithms, the proposed RSP algorithm has the best recovery performance. The relative research work is published in IEEE WCNC, 2014.

7.2 Future Work

Due to the limited time and energy of the author, this thesis still leaves some valuable research topics for future work. Some of the important and interesting research directions are pointed out as follows.

7.2.1 New DDS Scheme Based on Spatial and Temporary Correlation

The CNCDS scheme proposed in Chapter 3 has the highest energy efficiency at the lowest reconstruction error. However, the CNCDS scheme is only based on the spatial correlation of WSNs. In the future, we can further improve the energy efficiency of WSNs by utilizing the spatial and temporary correlation, and even the frequency correlation for OFDM based WSNs.

7.2.2 Novel Analog CS Method with Low Time Delay and Low Hardware Complexity

The RCOM-ACS scheme proposed in Chapter 4 reduces the hardware complexity of analog CS, but at the cost of a longer processing time. Although Section 4.3.5 has made a tradeoff between the hardware complexity and processing delay by proposing a fast RCOM-ACS scheme, in future, we can design a new analog CS method with a low time delay and low hardware complexity by designing a new measurement matrix.

7.2.3 New WSS Scheme Based on CS Measurements

The MCWSS scheme proposed in Chapter 5 has high detection performance with a low sampling rate. In the MCWSS scheme, CS measurements have to be firstly recovered before spectrum sensing, which increases the computational complexity of the MCWSS scheme. In future, we can merge the recovery and detection into one process, i.e., design a new detection algorithm directly based on the CS measurements rather than the CS recovered data.

7.2.4 Theoretical Analysis of Denoising Recovery Algorithm

Simulation results in Chapter 6 show that the proposed RSP algorithm has the best recovery performance compared with the existing CS denoising schemes. In future, we can theoretically prove the efficiency and reliability of RSP by analyzing its convergence and the limit of its reconstruction error.

Appendix A

Derivations of Some Expressions in Chapter 3

A.1 Derivation of \bar{S}_2

As shown in Figure 3.4(a), node i and node j are located at O and O' respectively, A and B are the two distinct intersecting points of these two circles with $d(i,j) < 2r_t$. \bar{S}_2 is the expected area of the lens-shaped region jointly covered by node i and node j . The area of $S_2/2$ equals to the area of sector OAB minus the area of triangle OAB . Thus, we have

$$\begin{aligned} S_2 &= 2 \left\{ \frac{r_t^2}{2} \times 2 \arccos \left(\frac{d}{2r_t} \right) - \frac{1}{2} \times \frac{d}{2} \times 2 \sqrt{r_t^2 - \frac{d^2}{4}} \right\} \\ &= 2r_t^2 \arccos \left(\frac{d}{2r_t} \right) - \frac{d}{2} \sqrt{4r_t^2 - d^2} \end{aligned} \quad (\text{A.1})$$

Since the nodes are uniformly distributed, $\Pr(d \leq x)$ equals to the area of the circle having radius x and being centered at O over the area of the circle having radius $2r_t$ and being centered at O [93]. Thus, we have

$$F_1(x) = \Pr(d \leq x) = \frac{\pi x^2}{4\pi r_t^2} = \frac{x^2}{4r_t^2}. \quad (\text{A.2})$$

Then, the probability density function (PDF) is $f_1(x) = \frac{x}{2r_t^2}$, and the average area of the

intersection is calculated by

$$\begin{aligned}\bar{S}_2 &= \int_0^{2r_t} (2r_t^2 \arccos(\frac{x}{2r_t}) - \frac{x}{2} \sqrt{4r_t^2 - x^2}) \times \frac{x}{2r_t^2} dx \\ &= \int_0^{2r_t} x \arccos(\frac{x}{2r_t}) dx - \frac{1}{4r_t^2} \int_0^{2r_t} x^2 \sqrt{4r_t^2 - x^2} dx\end{aligned}\quad (\text{A.3})$$

where the above two integrals are calculated as

$$\begin{aligned}&\int_0^{2r_t} x \arccos(\frac{x}{2r_t}) dx \\ &= \left[\left(\frac{x^2}{2} - r_t^2 \right) \arccos(\frac{x}{2r_t}) - \frac{x \sqrt{4r_t^2 - x^2}}{4} \right] \Big|_0^{2r_t} = \frac{\pi r_t^2}{2},\end{aligned}\quad (\text{A.4})$$

$$\begin{aligned}&\frac{1}{4r_t^2} \int_0^{2\pi} x^2 \sqrt{4r_t^2 - x^2} dx \\ &= \frac{1}{4r_t^2} \left[-\frac{x}{4} (4r_t^2 - x^2)^{\frac{3}{2}} + \frac{r_t^2 x}{2} \sqrt{4r_t^2 - x^2} + 2r_t^4 \arcsin(\frac{x}{2r_t}) \right] \Big|_0^{2r_t} \\ &= \frac{\pi r_t^2}{4}.\end{aligned}\quad (\text{A.5})$$

Combining (A.3), (A.4) and (A.5), we get

$$\bar{S}_2 = \frac{\pi r_t^2}{2} - \frac{\pi r_t^2}{4} = \frac{\pi r_t^2}{4}.\quad (\text{A.6})$$

A.2 Computation of \bar{S}_{II}

The computation of \bar{S}_{II} is very similar to that of \bar{S}_2 . The only difference is $d(n_{s,1}, n_{s,2}) < r_t$ rather than $d(i, j) < 2r_t$, as illustrated in Figure 3.4(b). Similarly, we can get

$$F_2(x) = \Pr(d \leq x) = \frac{\pi x^2}{\pi r_t^2} = \frac{x^2}{r_t^2}.\quad (\text{A.7})$$

The corresponding PDF is $f_2(x) = \frac{2x}{r_t^2}$, and \bar{S}_{II} is computed by

$$\bar{S}_{\text{II}} = \int_0^{r_t} (2r_t^2 \arccos(\frac{x}{2r_t}) - \frac{x}{2} \sqrt{4r_t^2 - x^2}) \times \frac{2x}{r_t^2} dx.\quad (\text{A.8})$$

Similar to the calculation of (A.4) and (A.5), we get

$$\bar{S}_{\text{II}} = \left(\pi - \frac{3\sqrt{3}}{4} \right) r_t^2.\quad (\text{A.9})$$

A.3 Calculation of $N_{r,1}^q$, $N_{r,2}^q$, $N_{r,3}^q$ and $N_{r,4}^q$

A.3.1 Calculation of $N_{r,1}^q$

The value of $N_{r,1}^q$ is the number of reception nodes in the area S_{III} (as shown in Figure 3.5(a)) in the q^{th} forwarding. Thus we have

$$N_{r,1}^q = N_t^q \times N \times \bar{S}_{III}. \quad (\text{A.10})$$

Since the distance between the selected forward node n_t^q and the node n_t^{q-1} which transmit packet to n_t^q is smaller than r_t , the value of \bar{S}_{III} is

$$\bar{S}_{III} = \pi r_t^2 - \bar{S}_{2s} = \pi r_t^2 - \left(\pi - \frac{3\sqrt{3}}{4}\right) r_t^2 = \frac{3\sqrt{3}}{4} r_t^2, \quad (\text{A.11})$$

where \bar{S}_{2s} is the expected area jointly covered by two nodes with their distance less than r_t , i.e., $\bar{S}_{2s} = \bar{S}_{II}$. Then, we have

$$N_{r,1}^q = N_t^q \times N \times \frac{3\sqrt{3}}{4} r_t^2. \quad (\text{A.12})$$

A.3.2 Calculation of $N_{r,2}^q$

Like the calculation of $N_{nr,II}$ in (3.21), the value of $N_{r,2}^q$ is

$$N_{r,2}^q = N_{c1} \times N \times \bar{S}_{c1}, \quad (\text{A.13})$$

where N_{c1} is the number of times that case one happens, and \bar{S}_{c1} is the expected value of area S_{c1} , which is represented by the oblique lines in Figure 3.5(b).

Firstly, N_{c1} is calculated as follows. Figure A.1(a) describes the critical situation where $S_{c1} = 0$ and $d(n_{t,1}^q, n_{t,2}^q) = \sqrt{3}r_t$. That is to say, case one will happen if the following two events happen simultaneously: (1) $d(n_{t,1}^q, n_{t,2}^q) < \sqrt{3}r_t$, (2) $n_{t,1}^q$ and $n_{t,2}^q$ are located in the area S_3 , which is represented by the solid oblique lines in Figure A.1(b). As presented in Section A.4, the expected value of S_3 is

$$\bar{S}_3 = \frac{5}{36} (4\pi - 3\sqrt{3}) r_t^2 - \frac{\pi}{6} r_t^2 = \frac{(14\pi - 15\sqrt{3})}{36} r_t^2. \quad (\text{A.14})$$

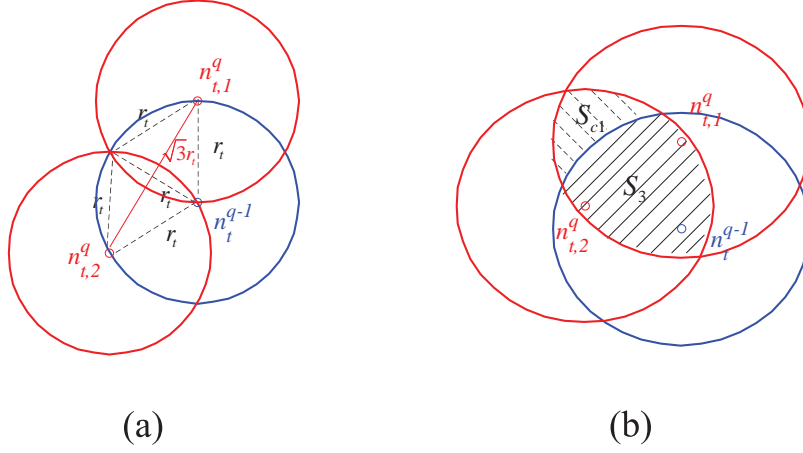


Figure A.1: (a) The critical situation when case one happens, (b) Illustration of the area of S_3 when calculating N_{c1} .

Thus, we have

$$N_{c1} = C_{N_t^q}^2 \bar{S}_3 = C_{N_t^q}^2 \times \frac{(14\pi - 15\sqrt{3})}{36} r_t^2. \quad (\text{A.15})$$

Then, the value of \bar{S}_{c1} is approximated as follows. Since it is too complicated to get the closed form expression for \bar{S}_{c1} , we use the method in [31] to approximate \bar{S}_{c1} , i.e., $\bar{S}_{c1} \simeq S_{c1, \max} = \pi r_t^2 / 6$. Finally, we have the expression for $N_{r,2}^q$, i.e.,

$$N_{r,2}^q = C_{N_t^q}^2 \times \frac{(14\pi - 15\sqrt{3})}{36} r_t^2 \times N \times \frac{\pi}{6} r_t^2. \quad (\text{A.16})$$

A.3.3 Calculation of $N_{r,3}^q$

As illustrated in Figure 3.6 (a), the value of $N_{r,3}^q$ should be calculated by

$$N_{r,3}^q = N_t^q \times p_{c2a} \times N \times \bar{S}_{c2a}, \quad (\text{A.17})$$

where p_{c2a} is the probability that the first situation of case two happens, i.e., the probability that the selected forward node n_t^q is located in the area jointly covered by node $n_{t,1}^{q-1}$ and node $n_{t,2}^{q-1}$ with $0 < d(n_{t,1}^{q-1}, n_{t,2}^{q-1}) < r_t$. Thus, the expression for p_{c2a} is

$$p_{c2a} = \frac{\bar{S}_{2s}}{\pi r_t^2} = \frac{(\pi - 3\sqrt{3}/4)r_t^2}{\pi r_t^2}. \quad (\text{A.18})$$

Again, similar to [114], we approximate \bar{S}_{c2a} as $\bar{S}_{c2a} = \pi r_t^2 / 6$. Thus, the expression for $N_{r,3}^q$ is

$$N_{r,3}^q = N_t^q \times \frac{(\pi - 3\sqrt{3}/4)r_t^2}{\pi r_t^2} \times N \times \frac{\pi r_t^2}{6}. \quad (\text{A.19})$$

A.3.4 Calculation of $N_{r,4}^q$

Similar to the calculation of $N_{r,3}^q$, the value of $N_{r,4}^q$ is

$$N_{r,4}^q = N_t^q \times p_{c2b} \times N \times \bar{S}_{c2b}, \quad (\text{A.20})$$

where p_{c2b} is the probability that the second situation of case two happens, i.e., the probability that the selected forward node n_t^q is located in the area jointly covered by node $n_{t,1}^{q-1}$ and node $n_{t,2}^{q-1}$ with $r_t < d(n_{t,1}^{q-1}, n_{t,2}^{q-1}) < 2r_t$. Then, the expression for p_{c2b} is

$$p_{c2b} = \frac{\bar{S}_{2l}}{\pi r_t^2} = \frac{3\sqrt{3}/16 r_t^2}{\pi r_t^2}, \quad (\text{A.21})$$

and the calculation of \bar{S}_{2l} is presented in Section A.5. As shown in Figure 3.6 (b), the size of \bar{S}_{c2b} equals to the area \bar{S}_{2s} jointly covered by node $n_{t,1}^{q-1}$ and node n_t^q minus the area \bar{S}_{2l} jointly covered by node $n_{t,1}^{q-1}$ and node $n_{t,2}^{q-1}$, i.e., $\bar{S}_{c2b} = \bar{S}_{2s} - \bar{S}_{2l}$. Since $0 < d(n_t^q, n_{t,2}^{q-1}) < r_t$ and $r_t < d(n_{t,1}^{q-1}, n_{t,2}^{q-1}) < 2r_t$, we have

$$\bar{S}_{c2b} = \bar{S}_{2s} - \bar{S}_{2l} = \left(\pi - \frac{3\sqrt{3}}{4}\right)r_t^2 - \frac{3\sqrt{3}}{16}r_t^2 = \left(\pi - \frac{15\sqrt{3}}{16}\right)r_t^2. \quad (\text{A.22})$$

Thus, the expression for $N_{r,4}^q$ is

$$N_{r,4}^q = N_t^q \times \frac{3\sqrt{3}r_t^2/16}{\pi r_t^2} \times N \times \left(\pi - \frac{15\sqrt{3}}{16}\right)r_t^2. \quad (\text{A.23})$$

A.4 Derivation of \bar{S}_3

As demonstrated in Figure A.1(b), the value of S_3 equals to the area S_{jc} which is jointly covered by $n_{t,1}^q$ and $n_{t,2}^q$ minus the area S_{c1} represented by the dotted oblique lines, i.e., $S_3 = S_{jc} - S_{c1}$. According to the linearity of expectation, we have $\bar{S}_3 = \bar{S}_{jc} - \bar{S}_{c1}$.

Again, the calculation of \bar{S}_{jc} is similar to that of \bar{S}_2 . Since the distance between $n_{t,1}^q$ and $n_{t,2}^q$ is smaller than $\sqrt{3}r_t$, we have

$$F_3(x) = \Pr(d \leq x) = \frac{\pi x^2}{3\pi r_t^2} = \frac{x^2}{3r_t^2}. \quad (\text{A.24})$$

So, the PDF is $f_3(x) = \frac{2x}{3r_t^2}$, and the calculation of \bar{S}_{jc} is

$$\bar{S}_{jc} = \int_0^{\sqrt{3}r_t} \left(2r_t^2 \arccos\left(\frac{x}{2r_t}\right) - \frac{x}{2} \sqrt{4r_t^2 - x^2} \right) \times \frac{2x}{3r_t^2} dx. \quad (\text{A.25})$$

Following a similar calculation as in (A.4) and (A.5), we get

$$\bar{S}_{jc} = \frac{5}{36} (4\pi - 3\sqrt{3}) r_t^2. \quad (\text{A.26})$$

Similar to that in Section A.3, the value of \bar{S}_{c1} is approximated as $\bar{S}_{c1} = \frac{\pi r_t^2}{6}$. Thus, we have

$$\bar{S}_3 = \bar{S}_{jc} - \bar{S}_{c1} = \frac{(14\pi - 15\sqrt{3})}{36} r_t^2. \quad (\text{A.27})$$

A.5 Computation of \bar{S}_{2l}

Figure 3.6(b) shows that S_{2l} is the area denoted by the dash oblique lines and $r_t < d(n_{t,1}^{q-1}, n_{t,2}^{q-1}) < 2r_t$. Very similar to the calculation of \bar{S}_2 in Section A.1, \bar{S}_{2l} is calculated by

$$\bar{S}_{2l} = \int_{r_t}^{2r_t} \left(2r_t^2 \arccos\left(\frac{x}{2r_t}\right) - \frac{x}{2} \sqrt{4r_t^2 - x^2} \right) \times \frac{x}{2r_t^2} dx. \quad (\text{A.28})$$

Following a similar calculation as in (A.4) and (A.5), we get $\bar{S}_{2l} = \frac{3\sqrt{3}}{16} r_t^2$.

Symbols

\mathbb{R}^N	N-dimensional real-number field
\mathbf{x}	vector
\mathbf{x}^T	transpose of vector
\mathbf{x}^H	conjugate transpose of vector
$\ \mathbf{x}\ _2$	ℓ_2 norm of vector
$\ \mathbf{x}\ _1$	ℓ_1 norm of vector
$\ \mathbf{x}\ _\infty$	ℓ_∞ norm of vector
$\ \mathbf{x}\ _0$	ℓ_0 norm of vector
$\langle \mathbf{x}, \mathbf{y} \rangle$	relevance between \mathbf{x} and \mathbf{y}
\mathbf{A}	matrix
\mathbf{A}^T	transpose of matrix
\mathbf{A}^H	conjugate transpose of matrix
\mathbf{A}^+	pseudoinverse of matrix
\mathbf{I}_N	identity matrix of dimension $N \times N$
\mathcal{F}	range of bandwidth
$\mathcal{B}\{\cdot\}$	bandlimited operator
$\mathcal{D}\{\cdot\}$	timelimited operator
$Pr(x < d)$	probability that event $x < d$ occurs
$\sup_x \{f(x)\}$	supremum of function $f(x)$

$|a|$ absolute value of number a

Abbreviations

1G 1st Generation mobile communication system

4G 4th Generation mobile communication system

5G 5th Generation mobile communication system

ADC Analog-to-Digital Conversion

AIC Analog-to-Information Conversion

AST Affine Scaling Transformation

AWGN additive Gaussian noise

BP Basis Pursuit

BPDN BP Denoising

CA Carrier Aggregation

CBS Combining Before Sampling

CDF Cumulative Distributed Function

CDP Compressive Data Persistence

CFAR Constant False Alarm Rate

CNCDS Compressed Network Coding based Distributed data Storage

CoSaMP Compressive Sampling MP

CR Cognitive Radio

CS Compressed Sensing

CRL₂ Combining Relevance via ℓ_2 norm

CTF Continuous To Finite

DA Divided-averaged

DCS Distributed Compressed Sensing

DCT Discrete Cosine Transform

DDS Distributed Data Storage

DFT Discrete Fourier Transform

DMD Digital Micromirror Device

DP Data Persistence

DPSSs Discrete Prolate Spheroidal Sequences

DTFT Discrete Time Fourier Transform

EGC Equal Gain Combining

FCC Federal Communications Commission

FOCUSS FOcal Underdetermined System Solver

ICASST interference-constrained adaptive simultaneous spectrum sensing and data transmission

ICStorage Improved CStorage

IDTFT Inverse-Discrete Time Fourier Transform

IHT Iterative Hard Thresholding

IMV Infinite Measurement Vector

IR Interpolation Recovery

IST Iterative Soft Thresholding

LASSO Least Absolute Shrinkage and Selection Operator

LPF Low Pass Filter

LS Least-Square

LTE-Advanced Long Term Evolution-Advanced

M-BP MMV-BP

M-OMP MMV-OMP

MCWSS Multi-antenna based Compressed Wideband Spectrum Sensing

MIP Mutual Incoherence Property

MMSE Minimum Mean Square Estimation

MMV Multiple Measurement Vector

MSE Mean Squared Error

MWC Modulated Wideband Converter

NoInitCNCDS No Initialization stage CNCDS

NP Non-deterministic Polynomia

NSS Narrowband Spectrum Sensing

OMP Orthogonal Matching Pursuit

PA Power Amplifier

PDF probability density function

PSWFs Prolate Spheroidal Wave Function

RCOM-ACS Random Circulant Orthogonal Matrix based Analog Compressed Sensing

RF Radio Front-ends

RG Random Geometric Graph

RIP Restricted Isometry Property

ROMP Regularized OMP

RSP Regularized Subspace Pursuit

SLC Square Law Combining

SNR Signal to Noise Ratio

SP Subspace Pursuit

SRCOM-ACS Short processing time RCOM-ACS

StOMP Stagewise OMP

UWB Ultra-WideBand

WSN Wireless Sensor Network

WSS Wideband Spectrum Sensing

ZC Zadoff-Chu

Bibliography

- [1] J. A. Tropp, J. N. Laska, M. F. Duarte, J. K. Romberg, and R. G. Baraniuk, “Beyond nyquist: Efficient sampling of sparse bandlimited signals,” *IEEE Transactions on Information Theory*, vol. 56, no. 1, pp. 520–544, 2010.
- [2] M. Mishali and Y. C. Eldar, “From theory to practice: Sub-nyquist sampling of sparse wideband analog signals,” *IEEE Journal of Selected Topics in Signal Processing*, vol. 4, no. 2, pp. 375–391, 2010.
- [3] J. A. Tropp, M. B. Wakin, M. F. Duarte, D. Baron, and R. G. Baraniuk, “Random filters for compressive sampling and reconstruction,” in *IEEE International Conference on Acoustics, Speech and Signal Processing, ICASSP*, vol. 3, 2006, pp. III–III.
- [4] D. Takhar, J. N. Laska, M. Wakin, M. F. Duarte, D. Baron, S. Sarvotham, K. F. Kelly, and R. Baraniuk, “A new compressive imaging camera architecture using optical-domain compression,” in *Proc. Computational Imaging*, 2006, pp. 43–52.
- [5] J. A. Tropp and A. C. Gilbert, “Signal recovery from random measurements via orthogonal matching pursuit,” *IEEE Transactions on Information Theory*, vol. 53, no. 12, pp. 4655–4666, 2007.
- [6] D. L. Donoho, “Compressed sensing,” *IEEE Transactions on Information Theory*, vol. 52, no. 4, pp. 1289–1306, 2006.

- [7] E. J. Candes and T. Tao, “Near-optimal signal recovery from random projections: Universal encoding strategies?” *IEEE Transactions on Information Theory*, vol. 52, no. 12, pp. 5406–5425, 2006.
- [8] E. J. Cands, “Compressive sampling,” in *Proceedings of the International Congress of Mathematicians*, 2006.
- [9] E. J. Candes and M. B. Wakin, “An introduction to compressive sampling,” *IEEE Signal Processing Magazine*, vol. 25, no. 2, pp. 21–30, 2008.
- [10] M. F. Duarte, M. A. Davenport, D. Takhar, J. N. Laska, S. Ting, K. F. Kelly, and R. G. Baraniuk, “Single-pixel imaging via compressive sampling,” *IEEE Signal Processing Magazine*, vol. 25, no. 2, pp. 83–91, 2008.
- [11] J. Romberg, “Imaging via compressive sampling,” *IEEE Signal Processing Magazine*, vol. 25, no. 2, pp. 14–20, 2008.
- [12] M. Lustig, D. L. Donoho, J. M. Santos, and J. M. Pauly, “Compressed sensing mri,” *IEEE Signal Processing Magazine*, vol. 25, no. 2, pp. 72–82, 2008.
- [13] J. Provost and F. Lesage, “The application of compressed sensing for photo-acoustic tomography,” *IEEE Transactions on Medical Imaging*, vol. 28, no. 4, pp. 585–594, 2009.
- [14] B. Jafarpour, V. Goyal, D. McLaughlin, and W. Freeman, “Transform-domain sparsity regularization for inverse problems in geosciences,” *GEOPHYSICS*, vol. 74, no. 5, pp. R69–R83, 2009.
- [15] F. Herrmann, D. Wang, G. Hennenfent, and P. Moghaddam, “Curvelet-based seismic data processing: A multiscale and nonlinear approach,” *GEOPHYSICS*, vol. 73, no. 1, pp. A1–A5, 2008.

- [16] S. Kirolos, J. Laska, M. Wakin, M. Duarte, D. Baron, T. Ragheb, Y. Massoud, and R. Baraniuk, “Analog-to-information conversion via random demodulation,” in *IEEE Dallas/CAS Workshop on Design, Applications, Integration and Software*, 2006, pp. 71–74.
- [17] T. Zhi and G. B. Giannakis, “Compressed sensing for wideband cognitive radios,” in *IEEE International Conference on Acoustics, Speech and Signal Processing, ICASSP*, vol. 4, 2007, pp. IV–1357–IV–1360.
- [18] C. Liu, K. Wu, and J. Pei, “An energy-efficient data collection framework for wireless sensor networks by exploiting spatiotemporal correlation,” *IEEE Transactions on Parallel and Distributed Systems*, vol. 18, no. 7, pp. 1010–1023, 2007.
- [19] D. Baron, M. Wakin, M. Duarte, S. Sarvotham, and R. Baraniuk, “Distributed compressed sensing,” *Preprint*, 2005.
- [20] E. J. Candes and T. Tao, “Decoding by linear programming,” *IEEE Transactions on Information Theory*, vol. 51, no. 12, pp. 4203–4215, 2005.
- [21] Z. Yu, S. Hoyos, and B. M. Sadler, “Mixed-signal parallel compressed sensing and reception for cognitive radio,” in *IEEE International Conference on Acoustics, Speech and Signal Processing, ICASSP*, 2008, pp. 3861–3864.
- [22] 3GPP, “Tr 36.808 evolved universal terrestrial radio access (e-utra); carrier aggregation; base station (bs) radio transmission and reception,” Tech. Rep., 2013.
- [23] W. Vereecken, W. V. Heddeghem, D. Colle, M. Pickavet, and P. Demeester, “Overall ict footprint and green communication technologies,” in *4th International Symposium on Communications, Control and Signal Processing (ISCCSP), 2010*, pp. 1–6.

- [24] S. Haykin, "Cognitive radio: brain-empowered wireless communications," *IEEE Journal on Selected Areas in Communications*, vol. 23, no. 2, pp. 201–220, 2005.
- [25] I. F. Akyildiz, W. Su, Y. Sankarasubramaniam, and E. Cayirci, "Wireless sensor networks: a survey," *Computer Networks*, vol. 38, no. 4, pp. 393–422, 2002.
- [26] T. S. Rappaport, S. Shu, R. Mayzus, Z. Hang, Y. Azar, K. Wang, G. N. Wong, J. K. Schulz, M. Samimi, and F. Gutierrez, "Millimeter wave mobile communications for 5g cellular: It will work!" *IEEE Access*, vol. 1, pp. 335–349, 2013.
- [27] J. Weitzen, L. Mingzhe, E. Anderland, and V. Eyuboglu, "Large-scale deployment of residential small cells," *Proceedings of the IEEE*, vol. 101, no. 11, pp. 2367–2380, 2013.
- [28] T. M. Cover and J. A. Thomas, *Elements of Information Theory*. A John Wiley & Sons, Inc. Publication, 2006.
- [29] Z. Kong, S. Aly, and E. Soljanin, "Decentralized coding algorithms for distributed storage in wireless sensor networks," *IEEE Journal on Selected Areas in Communications*, vol. 28, no. 2, pp. 261–267, 2010.
- [30] Y. Lin, B. Liang, and B. Li, "Data persistence in large-scale sensor networks with decentralized fountain codes," in *26th IEEE International Conference on Computer Communications, INFOCOM*, 2007, pp. 1658–1666.
- [31] F. Wang and J. Liu, "Networked wireless sensor data collection: Issues, challenges, and approaches," *IEEE Communications Surveys & Tutorials*, vol. 13, no. 4, pp. 673–687, 2011.
- [32] M. Zemedede, "Lte-advanced design and test challenges - carrier aggregation," *Agilent Technologies*, 2012.

- [33] S. E. W. Group, “Federal communications commission spectrum policy task force – report of the spectrum efficiency working group,” Tech. Rep., 2002.
- [34] J. Mitola and J. M. G. Q., “Cognitive radio: making software radios more personal,” *IEEE Personal Communications*, vol. 6, no. 4, pp. 13–18, 1999.
- [35] T. Yucek and H. Arslan, “A survey of spectrum sensing algorithms for cognitive radio applications,” *IEEE Communications Surveys & Tutorials*, vol. 11, no. 1, pp. 116–130, 2009.
- [36] I. F. Akyildiz, L. Won-Yeol, M. C. Vuran, and S. Mohanty, “A survey on spectrum management in cognitive radio networks,” *IEEE Communications Magazine*, vol. 46, no. 4, pp. 40–48, 2008.
- [37] E. Arias-Castro and Y. C. Eldar, “Noise folding in compressed sensing,” *IEEE Signal Processing Letters*, vol. 18, no. 8, pp. 478–481, 2011.
- [38] D. L. Donoho and X. Huo, “Uncertainty principles and ideal atomic decomposition,” *IEEE Transactions on Information Theory*, vol. 47, no. 7, pp. 2845–2862, 2001.
- [39] R. Gribonval and M. Nielsen, “Sparse representations in unions of bases,” *IEEE Transactions on Information Theory*, vol. 49, no. 12, pp. 3320–3325, 2003.
- [40] M. Aharon, M. Elad, and A. Bruckstein, “K-svd: An algorithm for designing overcomplete dictionaries for sparse representation,” *IEEE Transactions on Signal Processing*, vol. 54, no. 11, pp. 4311–4322, 2006.
- [41] H. Mohimani, M. Babaie-Zadeh, and C. Jutten, “A fast approach for overcomplete sparse decomposition based on smoothed l0 norm,” *IEEE Transactions on Signal Processing*, vol. 57, no. 1, pp. 289–301, 2009.

- [42] J. A. Tropp, “Greed is good: algorithmic results for sparse approximation,” *IEEE Transactions on Information Theory*, vol. 50, no. 10, pp. 2231–2242, 2004.
- [43] M. Rudelson and R. Vershynin, “On sparse reconstruction from fourier and gaussian measurements,” *Communications on Pure and Applied Mathematics*, vol. 61, no. 8, p. 21, 2008.
- [44] T. T. Cai, L. Wang, and G. Xu, “Stable recovery of sparse signals and an oracle inequality,” *IEEE Transactions on Information Theory*, vol. 56, no. 7, pp. 3516–3522, 2010.
- [45] T. T. Cai, G. Xu, and J. Zhang, “On recovery of sparse signals via l1 minimization,” *IEEE Transactions on Information Theory*, vol. 55, no. 7, pp. 3388–3397, 2009.
- [46] S. S. Chen, D. L. Donoho, and M. A. Saunders, “Atomic decomposition by basis pursuit,” *SIAM Review*, vol. 43, no. 1, pp. 129–159, 2001.
- [47] S. Chen and D. Donoho, “Basis pursuit,” in *Conference Record of the Twenty-Eighth Asilomar Conference on Signals, Systems and Computers*, vol. 1, 1994, pp. 41–44.
- [48] I. F. Gorodnitsky and B. D. Rao, “Sparse signal reconstruction from limited data using focuss: a re-weighted minimum norm algorithm,” *IEEE Transactions on Signal Processing*, vol. 45, no. 3, pp. 600–616, 1997.
- [49] D. L. Donoho, Y. Tsaig, I. Drori, and J. L. Starck, “Sparse solution of underdetermined systems of linear equations by stagewise orthogonal matching pursuit,” *IEEE Transactions on Information Theory*, vol. 58, no. 2, pp. 1094–1121, 2012.
- [50] S. Chatterjee, D. Sundman, and M. Skoglund, “Robust matching pursuit for recovery of gaussian sparse signal,” in *IEEE Digital Signal Processing Workshop and IEEE Signal Processing Education Workshop (DSP/SPE)*, 2011, pp. 420–424.

- [51] A. Jung, Z. Ben-Haim, F. Hlawatsch, and Y. C. Eldar, “Unbiased estimation of a sparse vector in white gaussian noise,” *IEEE Transactions on Information Theory*, vol. 57, no. 12, pp. 7856–7876, 2011.
- [52] R. E. Carrillo, K. E. Barner, and T. C. Aysal, “Robust sampling and reconstruction methods for sparse signals in the presence of impulsive noise,” *IEEE Journal of Selected Topics in Signal Processing*, vol. 4, no. 2, pp. 392–408, 2010.
- [53] P. Duc-Son and S. Venkatesh, “Improved image recovery from compressed data contaminated with impulsive noise,” *IEEE Transactions on Image Processing*, vol. 21, no. 1, pp. 397–405, 2012.
- [54] M. Raginsky, R. M. Willett, Z. T. Harmany, and R. F. Marcia, “Compressed sensing performance bounds under poisson noise,” *IEEE Transactions on Signal Processing*, vol. 58, no. 8, pp. 3990–4002, 2010.
- [55] J. A. Tropp, “Just relax: convex programming methods for identifying sparse signals in noise,” *IEEE Transactions on Information Theory*, vol. 52, no. 3, pp. 1030–1051, 2006.
- [56] R. Tibshirani, “Regression shrinkage and selection via the lasso,” *Journal of the Royal Statistical Society. Series B (Methodological)*, vol. 58, no. 1, pp. 267–288, 1996.
- [57] M. J. Wainwright, “Sharp thresholds for high-dimensional and noisy sparsity recovery using ℓ_1 -constrained quadratic programming (lasso),” *IEEE Transactions on Information Theory*, vol. 55, no. 5, pp. 2183–2202, 2009.
- [58] Z. Xu, X. Chang, F. Xu, and H. Zhang, “ $L_{1/2}$ regularization: A thresholding representation theory and a fast solver,” *IEEE Transactions on Neural Networks and Learning Systems*, vol. 23, no. 7, pp. 1013–1027, 2012.

- [59] D. Needell and R. Vershynin, "Signal recovery from incomplete and inaccurate measurements via regularized orthogonal matching pursuit," *IEEE Journal of Selected Topics in Signal Processing*, vol. 4, no. 2, pp. 310–316, 2010.
- [60] D. Needell and J. A. Tropp, "Cosamp: Iterative signal recovery from incomplete and inaccurate samples," *Applied and Computational Harmonic Analysis*, vol. 26, no. 3, pp. 301–321, 2009.
- [61] D. Wei and O. Milenkovic, "Subspace pursuit for compressive sensing signal reconstruction," *IEEE Transactions on Information Theory*, vol. 55, no. 5, pp. 2230–2249, 2009.
- [62] T. T. Cai and L. Wang, "Orthogonal matching pursuit for sparse signal recovery with noise," *IEEE Transactions on Information Theory*, vol. 57, no. 7, pp. 4680–4688, 2011.
- [63] R. Wu, W. Huang, and D. Chen, "The exact support recovery of sparse signals with noise via orthogonal matching pursuit," *IEEE Signal Processing Letters*, vol. 20, no. 4, pp. 403–406, 2013.
- [64] T. Blumensath and M. E. Davies, "Iterative hard thresholding for compressed sensing," *Applied and Computational Harmonic Analysis*, vol. 27, pp. 265–274, 2009.
- [65] I. Daubechies, M. Defrise, and C. D. Mol, "An iterative thresholding algorithm for linear inverse problems with a sparsity constraint," *Communications on Pure and Applied Mathematics*, vol. 57, no. 11, pp. 1413–1457, 2004.
- [66] M. A. Lexa, M. E. Davies, and J. S. Thompson, "Reconciling compressive sampling systems for spectrally sparse continuous-time signals," *IEEE Transactions on Signal Processing*, vol. 60, no. 1, pp. 155–171, 2012.

- [67] O. Taheri and S. A. Vorobyov, "Segmented compressed sampling for analog-to-information conversion: Method and performance analysis," *IEEE Transactions on Signal Processing*, vol. 59, no. 2, pp. 554–572, 2011.
- [68] X. Yang, X. Tao, Y. J. Guo, X. Huang, and Q. Cui, "Subsampled circulant matrix based analogue compressed sensing," *Electronics Letters*, vol. 48, no. 13, pp. 767–768, 2012.
- [69] X. Yang, Y. J. Guo, Q. Cui, X. Tao, and X. Huang, "Random circulant orthogonal matrix based analog compressed sensing," in *IEEE Global Telecommunications Conference (GLOBECOM)*, 2012, pp. 3612–3616.
- [70] Y. Chen, M. Mishali, Y. C. Eldar, and A. O. Hero, "Modulated wideband converter with non-ideal lowpass filters," in *IEEE International Conference on Acoustics Speech and Signal Processing (ICASSP)*, 2010, pp. 3630–3633.
- [71] E. Matusiak and Y. C. Eldar, "Sub-nyquist sampling of short pulses," *IEEE Transactions on Signal Processing*, vol. 60, no. 3, pp. 1134–1148, 2012.
- [72] M. Vetterli, P. Marziliano, and T. Blu, "Sampling signals with finite rate of innovation," *IEEE Transactions on Signal Processing*, vol. 50, no. 6, pp. 1417–1428, 2002.
- [73] J. Meng, H. Li, and Z. Han, "Sparse event detection in wireless sensor networks using compressive sensing," in *43rd Annual Conference on Information Sciences and Systems (CISS)*, 2009, pp. 181–185.
- [74] M. Lin, C. Luo, F. Liu, and F. Wu, "Compressive data persistence in large-scale wireless sensor networks," in *IEEE Global Telecommunications Conference (GLOBECOM)*, 2010, pp. 1–5.

- [75] A. Talari and N. Rahnavard, “Cstorage: Distributed data storage in wireless sensor networks employing compressive sensing,” in *IEEE Global Telecommunications Conference (GLOBECOM)*, 2011, pp. 1–5.
- [76] G. Taubock and F. Hlawatsch, “A compressed sensing technique for ofdm channel estimation in mobile environments: Exploiting channel sparsity for reducing pilots,” in *IEEE International Conference on Acoustics, Speech and Signal Processing (ICASSP)*, 2008, pp. 2885–2888.
- [77] J. L. Paredes, G. R. Arce, and Z. Wang, “Ultra-wideband compressed sensing: Channel estimation,” *IEEE Journal of Selected Topics in Signal Processing*, vol. 1, no. 3, pp. 383–395, 2007.
- [78] J. Yick, B. Mukherjee, and D. Ghosal, “Wireless sensor network survey,” *Computer Networks*, vol. 52, no. 12, pp. 2292–2330, 2008.
- [79] R. Zeng, Y. Jiang, C. Lin, Y. Fan, and X. Shen, “A distributed fault/intrusion-tolerant sensor data storage scheme based on network coding and homomorphic fingerprinting,” *IEEE Transactions on Parallel and Distributed Systems*, vol. 23, no. 10, pp. 1819–1830, 2012.
- [80] Y. Ren, V. Oleshchuk, and F. Y. Li, “A scheme for secure and reliable distributed data storage in unattended wsns,” in *IEEE Global Telecommunications Conference (GLOBECOM)*, 2010, pp. 1–6.
- [81] J. Liang, J. Wang, and J. Chen, “An overhearing-based scheme for improving data persistence in wireless sensor networks,” in *IEEE International Conference on Communications (ICC)*, 2010, pp. 1–5.

- [82] W. Zhang, X. Ma, and G. Choi, "Enhancing data persistence for energy constrained networks by network modulation," in *47th Annual Allerton Conference on Communication, Control, and Computing*, 2009, pp. 214–221.
- [83] J. W. Byers, M. Luby, and M. Mitzenmacher, "A digital fountain approach to asynchronous reliable multicast," *IEEE Journal on Selected Areas in Communications*, vol. 20, no. 8, pp. 1528–1540, 2002.
- [84] D. J. C. MacKay, "Fountain codes," *IEE Proceedings-Communications*, vol. 152, no. 6, pp. 1062–1068, 2005.
- [85] T. D. Nguyen, L. L. Yang, and L. Hanzo, "Systematic luby transform codes and their soft decoding," in *IEEE Workshop on Signal Processing Systems*, 2007, pp. 67–72.
- [86] Q. Wang, M. Hempstead, and W. Yang, "A realistic power consumption model for wireless sensor network devices," in *3rd Annual IEEE Communications Society on Sensor and Ad Hoc Communications and Networks, SECON*, vol. 1, 2006, pp. 286–295.
- [87] T. Ho, M. Medard, R. Koetter, D. R. Karger, M. Effros, S. Jun, and B. Leong, "A random linear network coding approach to multicast," *IEEE Transactions on Information Theory*, vol. 52, no. 10, pp. 4413–4430, 2006.
- [88] D. S. Lun, N. Ratnakar, R. Koetter, M. Medard, E. Ahmed, and L. Hyunjoon, "Achieving minimum-cost multicast: a decentralized approach based on network coding," in *24th Annual Joint Conference of the IEEE Computer and Communications Societies, INFOCOM*, vol. 3, 2005, pp. 1607–1617.

- [89] S. Chachulski, M. Jennings, S. Katti, and D. Katabi, "Trading structure for randomness in wireless opportunistic routing," *SIGCOMM Comput. Commun. Rev.*, vol. 37, no. 4, pp. 169–180, 2007.
- [90] S. Katti, S. Shintre, S. Jaggi, D. Katabi, and M. Medard, "Real network codes," pp. 389–395, 2007.
- [91] N. Nguyen, D. L. Jones, and S. Krishnamurthy, "Netcompress: Coupling network coding and compressed sensing for efficient data communication in wireless sensor networks," in *IEEE Workshop on Signal Processing Systems (SIPS)*, 2010, pp. 356–361.
- [92] N. Rahnavard, B. Vellambi, and F. Fekri, "Crbcast: a reliable and energy-efficient broadcast scheme for wireless sensor networks using rateless codes," *IEEE Transactions on Wireless Communications*, vol. 7, no. 12, pp. 5390–5400, 2008.
- [93] C. Y. Chang, K. P. Shih, and S. C. Lee, "Zbp: a zone-based broadcasting protocol for wireless sensor networks," in *18th International Conference on Advanced Information Networking and Applications, AINA*, vol. 1, 2004, pp. 84–89.
- [94] M. Penrose, *Random Geometric Graphs*. Oxford University Press, 2004.
- [95] P. Hall, *Introduction to the Theory of Coverage Process*. John Wiley and Sons, 1998.
- [96] L. H. Yen and Y. M. Cheng, "Clustering coefficient of wireless ad hoc networks and the quantity of hidden terminals," *IEEE Communications Letters*, vol. 9, no. 3, pp. 234–236, 2005.

- [97] M. A. Davenport and M. B. Wakin, "Compressive sensing of analog signals using discrete prolate spheroidal sequences," *Applied and Computational Harmonic Analysis*, vol. 33, pp. 438–472, 2012.
- [98] D. Slepian, "Prolate spheroidal wave functions, fourier analysis, and uncertainty - v: the discrete case," *The Bell System Technical Journal*, vol. 57, pp. 1371–1429, 1978.
- [99] D. Slepian and H. O. Pollak, "Prolate spheroidal wave functions, fourier analysis, and uncertainty - i," *The Bell System Technical Journal*, pp. 43–63, 1961.
- [100] J. Chen and X. Huo, "Theoretical results on sparse representations of multiple-measurement vectors," *IEEE Transactions on Signal Processing*, vol. 54, no. 12, pp. 4634–4643, 2006.
- [101] M. Mishali and Y. C. Eldar, "Reduce and boost: Recovering arbitrary sets of jointly sparse vectors," *IEEE Transactions on Signal Processing*, vol. 56, no. 10, pp. 4692–4702, 2008.
- [102] S. F. Cotter, B. D. Rao, K. Engan, and K. Kreutz-Delgado, "Sparse solutions to linear inverse problems with multiple measurement vectors," *IEEE Transactions on Signal Processing*, vol. 53, no. 7, pp. 2477–2488, 2005.
- [103] Z. Ye, G. Memik, and J. Grosspietsch, "Energy detection using estimated noise variance for spectrum sensing in cognitive radio networks," in *IEEE Wireless Communications and Networking Conference, WCNC*, 2008, pp. 711–716.
- [104] H. V. Poor, *An introduction to signal detection and estimation (2nd ed.)*. Springer-Verlag New York, Inc., 1994.

- [105] D. Shen, X. Gan, H.-H. Chen, L. Qian, and M. Xu, "Significant cycle frequency based feature detection for cognitive radio systems," in *4th International Conference on Cognitive Radio Oriented Wireless Networks and Communications (CROWN-COM), 2009*, pp. 1–4.
- [106] I. F. Akyildiz, W. Y. Lee, M. C. Vuran, and S. Mohanty, "Next generation/dynamic spectrum access/cognitive radio wireless networks: A survey," *Computer Networks*, vol. 50, no. 13, pp. 2127–2159, 2006.
- [107] R. Tandra and A. Sahai, "Fundamental limits on detection in low snr under noise uncertainty," in *International Conference on Wireless Networks, Communications and Mobile Computing*, 2005, pp. 464–469 vol.1.
- [108] Z. Quan, S. Cui, A. H. Sayed, and H. V. Poor, "Optimal multiband joint detection for spectrum sensing in cognitive radio networks," *IEEE Transactions on Signal Processing*, vol. 57, no. 3, pp. 1128–1140, 2009.
- [109] Z. Tian and G. B. Giannakis, "A wavelet approach to wideband spectrum sensing for cognitive radios," in *1st International Conference on Cognitive Radio Oriented Wireless Networks and Communications*, 2006, pp. 1–5.
- [110] <http://white.stanford.edu/trac/pdcprojects/browser/restimation/Dictionary%20Learning/KSVD/OMP.m?rev=177>.
- [111] <http://www-personal.umich.edu/~romanv/software/romp.m>.
- [112] http://media.aau.dk/null_space_pursuits/2011/07/08/cosamp.m.
- [113] http://media.aau.dk/null_space_pursuits/2011/07/08/subspacepursuit.m.

-
- [114] C. W. Yu, “Computing subgraph probability of random geometric graphs with applications in quantitative analysis of ad hoc networks,” *IEEE Journal on Selected Areas in Communications*, vol. 27, no. 7, pp. 1056–1065, 2009.